Investigating photoinduced phenomena in molecular crystals with prospects for atomically-resolved dynamics

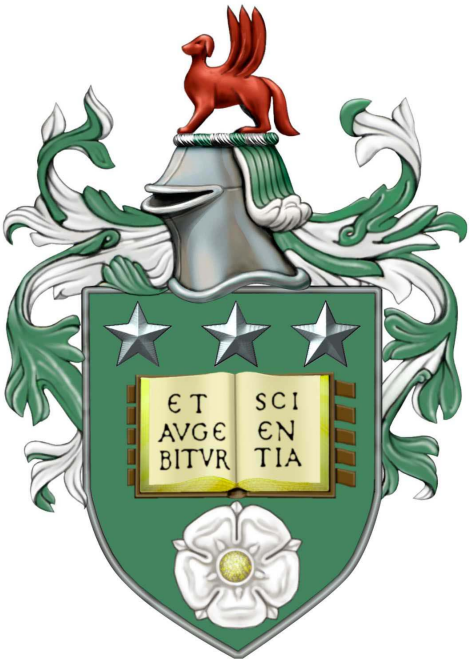

Khalid Maqbool Siddiqui

Submitted in accordance with the requirements for the degree of

Doctor of Philosophy

The University of Leeds

School of Chemistry

December 2016

Declaration

The candidate confirms that the work submitted is his own, except where work which has formed part of jointly-authored publications has been included. The contribution of the candidate and the other authors to this work has been explicitly indicated below. The candidate confirms that appropriate credit has been given within the thesis where reference has been made to the work of others.
The work in Chapter 4 of the thesis has appeared in publication as follows:

K. M. Siddiqui, G. Corthey, S. A. Hayes, A. Rossos, D. S. Badali, R. Xian, R. S. Murphy, B. J. Whitaker and R. J. D. Miller, *CrystEngComm.*, 18, 7212-7216, (2016).
I performed the experiments and analysis and built parts of the transient absorption apparatus: NOPA and the pump line.
Dr Corthey built the main transient absorption setup and the acquisition software. He also played a key role in discussions, planning, analysis and running of the experiment.
Dr Hayes was involved with planning, discussions and the running of the experiments. He also provided support for the construction of the NOPA.
Drs Rossos and Murphy supported with sample preparation.
Dr Rui calibrated the detector and Dr Badali contributed to the original design and building of the transient absorption setup.
Profs Miller and Whitaker initiated the original study and provided advice and support throughout the work.

"To my parents, Maqbool and Robina
and siblings, Nisa and Ertan"

Acknowledgements

I would like to first of all thank my supervisors, Profs Whitaker and Miller. I have been working with Prof Whitaker since the summer of 2010 and I can say that it has been a thoroughly satisfactory journey for me. I thank him for introducing me to lasers, for teaching me physics and above all for supporting me on almost every aspect of my university life. I will remain forever grateful. I sincerely thank Prof Miller for giving me the opportunity to work in his group. To be around such an excellent cast of scientists has contributed to my own development as a scientist. I also thank him for his support during testing times in the lab; he always knows what to say and how and when to say it and I feel honoured to have worked under his supervision.

My deep gratitude goes to Stuart and Gaston with whom I shared the lab and from whom I have learnt a lot. Their selflessness, cooperation and patience with me have been nothing short of exemplary and I thank them for it. Thanks also to Marcos and Xinxin for constant encouragement and passing down valuable advice and also for taking time to read my thesis manuscript despite their busy schedules.

To the IMPRS school for providing a nice base for exchanging ideas and for the friendly faces. I would like to especially thank the coordinators, past and present, Frau Anja Bleidhorn, Dr Sonia Utermann and Dr Julia Quante, who have all been exceptionally kind to me and helped me immensely; being a Leeds University student in Hamburg, I would often hit a snag with university matters and they were ever-present to sort things out for me.

I also like to mention our collaborators: Dr Tadahiko Ishikawa and Dr Scott Murphy, for giving me the chance to engage in interesting projects and thank them for their contribution in my research. I also thank Michal Kochman for handling the theory side of the project and also for clarifying many concepts relating to quantum chemistry.

Other people and friends (past and present) that require a mention are Prof Dick, Dr Mike Nix, Ingvar Kraatz, Hugh Sowey, German Sciaini, Kostya Pichugin, Sabine Bank, Hong-Guan, Rolf Loch, Xian Rui, Andreas Rossos and of course, the whole Miller group.

And I would foremost like to thank my family and most of all my parents. All of my successes are for you. Thanks for bearing with me throughout all this time, for your unconditional love and unrelenting support for which I am eternally in your debt. And finally, I thank God for giving me the strength to reach the finishing line.

Abstract

Molecular crystals are at the forefront of research to find new technologies and to probe emerging phenomena such as superconductivity. Their studies are, therefore, important but also challenging, especially in the field of atomically-resolved dynamics due to low damage thresholds and other factors. Two such crystals, showing different phenomena, were the focus of this work.

The dynamics of photochemical reaction in ultrathin crystals of spirooxazines were studied using a home-built transient absorption setup and 266 nm light for excitation. They were found not to be completely photochromic in crystalline state, in contrast to their behaviour in solution and amorphous films. A transient emerges after excitation, which evolves to form planar trans-merocynanine product within 80 ps in solution, but due to steric restrictions in the crystal, only the ring-opened form of spirooxazine was created without undergoing isomerisation. For these experiments, a methodology was developed to tackle the issue relating to the permanent formation of the photoproducts in crystals, which severely hampers reversibility. It made use of an additional ultrashort beam, making it a three-beam approach, with the third beam acting to arrest the accumulation of the products by removing them from the probe volume via the back photoreaction. Using this approach, it was possible to achieve over 10,000 pump-probe cycles, enabling time-resolved spectroscopy of this system and opens up prospect for femtosecond diffraction experiments.

Femtosecond electron diffraction study was carried out on EDO-MeEDO, a doped crystal of EDO-TTF. The response of the system was found to be different to what is known for the pure EDO-TTF crystal; our findings could not confirm

the occurrence of a cell doubling phase transition. At acoustic time scales, it is hypothesised that cooperative effects play a role, which lead to pronounced phonon signals. Further studies are needed to understand the dynamics of this system.

Contents

List of Figures

List of Tables

"There is nothing that living things do
that cannot be understood from the point
of view that they are made of atoms
acting according to the laws of physics."
—**Richard Feynman**

Chapter 1

Introduction

"Seeing is believing" —the idiom from the seventeenth century holds a special meaning across many scientific disciplines [1]. A major part of our understanding of the world today is due to the ability to observe and measure different states of matter. The discoveries of the nuclei by Rutherford in 1890 [2] and electrons by J.J.Thompson in 1897 [3], amongst others, were a confirmation for the existence of atoms and became a catalyst for many exciting developments, both in theory and experiments. Experimentally, the invention of the laser [4, 5] and the development of diffraction and microscopy techniques were a major advance. Today, it is possible to "see" individual atoms using a scanning tunneling microscope (STM) [6]. Many physico-chemical phenomena involve displacement of atoms of some sort happening at the molecular level. It is therefore interesting to be able to see these displacements as they happen. As Muhammad Ali once boasted about his speed in the boxing ring, "His hands cannot hit what his eyes cannot see". In a similar vein, one cannot control what one cannot observe. Controlling molecular processes generally requires detailed knowledge of the underlying physics and the associated structural changes, which can be acquired by studying them at the atomic level. This endeavour represents the main goal of the field of ultrafast structural dynamics and also of this thesis work.

1.1 The need for atomic scales

This section discusses the need for atomic level probing and also defines the atomic scale. Fig 1.1 provides a guide to the typical length and time scales that are characteristic of different objects and processes. As can be seen from the length scales, that, in order to peer at atoms and molecules, we must venture into the Ångstrom scale (1 Å= 10^{-10} m). The eye is a powerful apparatus in the human anatomy that is responsible for vision, but it is unable to resolve objects smaller than 0.001 mm. Microscopy is the field concerned with viewing objects that are too small for the eye to detect [7]. The optical microscopes using visible radiations are able to, at best, magnify and resolve objects of sizes down to 250 nm (1 nm = 10 Å) [8]. The main limitation to achieving a better resolution than this is due to diffraction, which smears out the features smaller than $\lambda/2$. This is also known as the Abbe resolution limit [9]. Recently, techniques known collectively as super-resolution microscopies have been developed that circumvent the diffraction limit and effectively bring the resolution into sub-20 nm domain [10, 11]. Stefan Hell, Eric Betzig and William Moerner shared the 2014 chemistry Nobel prize for their pioneering research that led to the development of these techniques [12]. But, despite this incredible improvement, the resolution has still not reached the atomic level. If, however, the visible light is replaced by any source that emits radiation that has a wavelength comparable with or smaller than the typical inter-atomic distance then it can, in theory, be used to investigate atoms and molecules. Neutrons, x-rays or electron all have wavelengths that are well suited for this purpose and have conventionally been used to elucidate structures of molecules using diffraction techniques. It should be pointed out that other techniques do exist, such as nuclear magnetic resonance (NMR) and infrared (IR) spectroscopy to name a couple, that can also be used for structure determination, but methods involving x-rays and subatomic particles provide much higher resolutions as they are direct probes of molecular structures.

The interest in determining the structure of molecules is due to the wealth of useful information that can be obtained from it. For example, measuring the

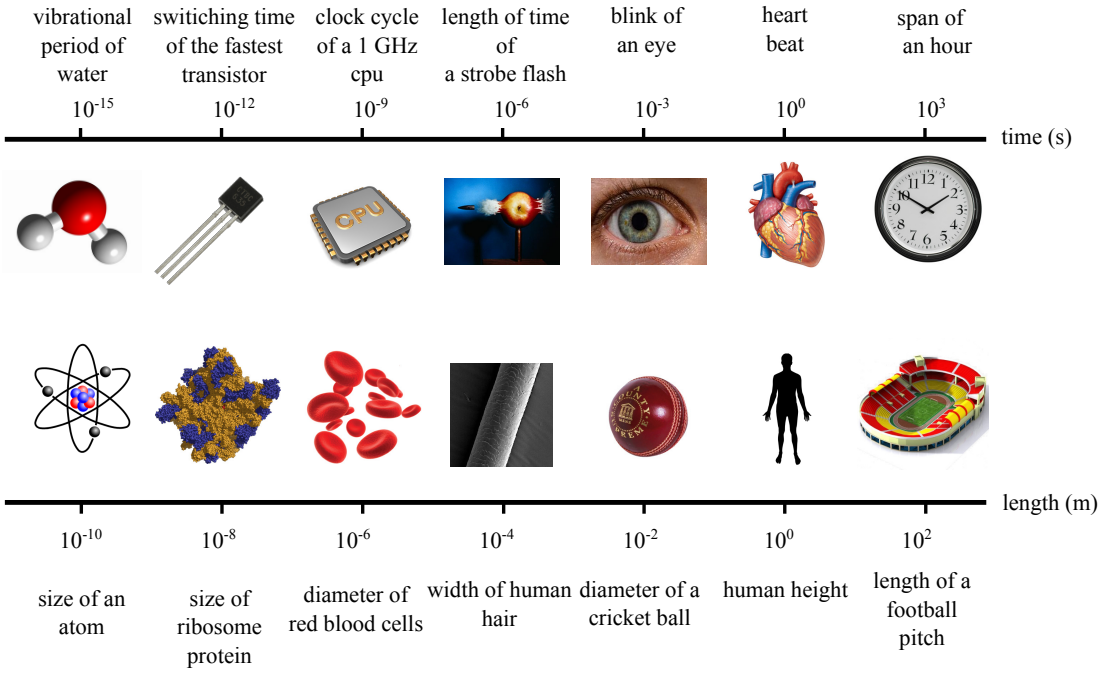

Figure 1.1: Orders of magnitude (images from various sources).

energy levels of molecules, by means of spectroscopy, can provide information on the electronic structures, which can be used to predict reactivity. Similarly, the knowledge of molecular structures can help to understand the tendencies of molecules towards forming certain bonds. For instance, a molecule with a hydroxyl (OH) functional group can form a hydrogen bond with an oxygen or other highly electronegative atom. In fact, a statement is often made which relates the structure directly to function: structure defines function. Therefore, determining (electronic or molecular) structures are considered imperative to understand the properties of many systems. Most structural determination techniques are able to provide only time-averaged (static) structural information. While clearly useful for characterisation purposes, if the goal really is to understand what is occurring at the molecular level, so as to control processes, e.g., to devise tailored materials, then the information on only the static structures is not sufficient and the dynamic aspect of the system must be considered.

To get an appreciation for the need for dynamic information consider, for ex-

ample, a football match played between two teams, A and B that ends with team A scoring six goals and team B scoring none, therefore the scores at the beginning (zero all) and the end are well-determined. Anyone who had not watched the match can only hazard a guess (which may or may not be correct) as to what might have transpired in the match. For instance, one might be able to guess who the goal scorers were based on the form of the players leading up to the match or speculate some poor decision from the referee owing to some past history. In any case, only by watching the replay of the match can one truly learn about the key moments that played out and defined the final outcome. This football match analogy is a reasonable one when discussing the need to follow the dynamics. Often well-defined structures of the molecules that form the reactants in a chemical reaction are available and it is possible to fully characterise the products. But, how can one make the connection between the two when there can be a myriad of possible routes from the reactant to the final products? In other words, what is the reaction mechanism? Traditionally, chemical knowledge and intuition have aided this exercise. But, as has already been emphasised, the specific motions that define a reaction outcome cannot be deduced *a priori* from the time-averaged structures and in order to determine the structural dynamics, probing in the relevant timescales is necessary. To establish the atomic timescales, let's consider the dissociation of a bond as an example. The timescale in question is then that of atoms moving approximately 1 Å along the dissociation coordinate at the speed of sound (typically 10^3 m s^{-1} in solids). This equates to about 100 femtoseconds (1 fs = 10^{-15} s). This is just one example and there are certainly other processes occurring on either slower or faster timescales. For example, the vibrational period of the OH stretching in water was determined to be roughly on the order of 10-150 fs [13]. Nevertheless, the 100 fs serves as a good figure for the time resolution that must be achieved if the molecular motions are to be tracked.

1.1.1 Making molecular movies

Any experiment that measures the evolution of molecules with atomic spatial and time resolutions can be referred to as the 'molecular movie'. As already mentioned, x-rays and subatomic particles are suitable for probing structures with atomic spatial resolution, but what about the required time resolution? The camera that would be needed to capture the molecular motions must have an effective shutter speed on the order of 100 fs or shorter. To justify that it is the shutter speed that will be important, see Fig 1.2 which shows photographs of a fountain taken with a camera with fast speed of the shutter (panel a) and with slow shutter speeds (panel b). As can be seen, with higher shutter speeds of the camera, the drops of the water flowing out of the fountain are more clearly distinguished than with lower shutter speed, in which case they are completely smeared out. This is of course a macroscopic example, so what can be said about the cameras needed for capturing molecular motion? No electronic detector is fast enough to approach the figure needed to capture molecular motions in real time. Indeed, it was thought inconceivable to reach the time resolution necessary to probe ultrafast phenomena until the advent of ultrashort laser technology over three decades ago [14]. Nowadays, it is quite routine to produce and characterise laser flashes that have durations as short as a few hundred attoseconds (1 as = 10^{-18} s), so that the 'shutter speed' required to freeze molecular motions is no longer elusive, i.e. ultrafast lasers can act as molecular cameras. Such 'cameras' have been used in probing matter using pump-probe approaches in which one pulse of light is used to initiate the dynamics of interest and another pulse —that is delayed from the first one, is used to capture images at different stages of the molecular process and these images can be treated like frames of a film that can be stitched together to give a sense of a 'movie'. When ultrafast light pulses are used as the probe, the technique is termed time-resolved spectroscopy. Being spectroscopic techniques, they measure the transitions in rotational, vibrational and electronic energy manifolds of molecules depending on the whether microwave, infrared or ultraviolet (UV) light is used, respectively. Time-resolved

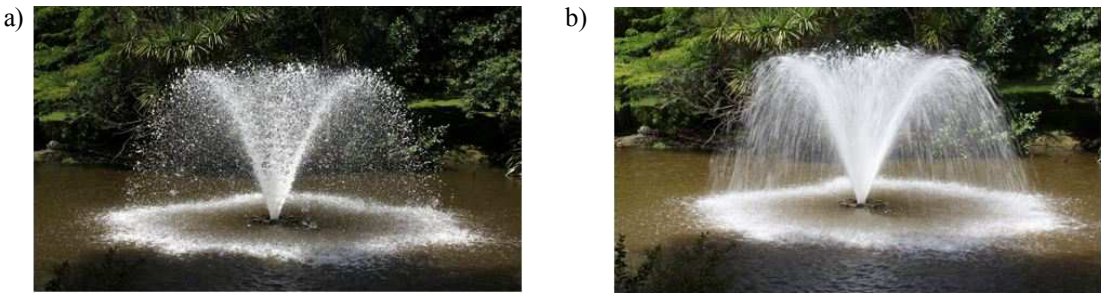

Figure 1.2: Photographs of a fountain taken with a) fast shutter speed and b) slow shutter speed. Notice the difference in the exposure. Taken from [15].

spectroscopies have provided very useful insights on many different ultrafast phenomena, in many area of physical sciences and today form an indispensable tool for any laboratory concerned with ultrafast studies of matter. The interpretation of the experimental results from such techniques and reconstruction of molecular structures, however, often requires support from theory and/or simulations. Construction of potential energy surfaces (PES) —a multi-dimensional surface that describes the change of the potential energy of the molecule as a function of some internal coordinate, of all the relevant (electronic) states of a system is often undertaken and dynamic simulations are performed on these surfaces to model the data. For small molecules, such as diatoms with $3N$-5 internal coordinates (where N is the number of atoms in the molecule)[1], this can be done at a high level of theory (both *ab initio* methods or density functional theory (DFT) can be used), but for large, complex systems the calculations can rapidly become intractable. Moreover, spectroscopy can only probe states which do not involve non-radiative pathways, i.e. it can not detect dark states.

Diffraction techniques, on the other hand, provide atomic level detail on the molecular structure and can even detect dark states, but are traditionally time-averaged measurements. By combining the strengths of ultrafast spectroscopy and diffraction techniques, one can follow the evolution of structures in actual time. The marriage of the two fields gives rise to time-resolved diffraction.

[1] $3N$-6 internal coordinates in the case of nonlinear molecules.

1.2 Electrons as structural probes

The choice of the structural probe for time-resolved diffraction experiments is usually between electrons and x-rays. The production of neutron beams requires nuclear reactors or spallation facilities, which makes them a less attractive option and furthermore no known facility has reported on the production of femtosecond bunches of neutrons [2], therefore the discussion in this section will be limited to x-rays and electrons only. Both have their merits and shortcomings and these should be considered when choosing between the two as structural probes. Electrons differentiate themselves from x-rays by how strongly they interact with matter. Being charged particles, they 'feel' the electrostatic potential around the atoms whereas the x-rays are electromagnetic waves that are only scattered by the electron density. If the wavelength remains unchanged in the scattering process, it is referred to as elastic scattering (Thompson scattering for case of x-rays) and conversely it is called inelastic scattering (Compton scattering for x-rays) when the wavelength is changed. Due to the different degree of interaction, the scattering cross-sections for electrons and x-rays are different. Electrons are (elastically) scattered a factor of 10^6 times more strongly than the x-rays [17]. This has some implications, such as for the flux (number of photons/electrons per second per unit area) that is needed to obtain a sufficiently high quality diffraction pattern, in particular from weak scattering systems or dilute samples. The flux requirement is largely reduced in the case of electrons compared to the x-rays. Indeed, for gas-phase diffraction studies in which the low density of the gaseous molecules is often the limiting factor to obtain a diffraction pattern with high signal-to-noise (S/N) ratio, electrons are the preferred choice. Similarly, for solid samples, the higher scattering cross-sections favour the use of electrons as the 'dose' can be kept to a tolerable level, especially when studying sensitive specimens, e.g. proteins and viruses. The x-rays are notorious for causing radiation damage [18] when high doses are used —as would typically be needed to obtain high quality data. The origins of the radiation damage is mainly in the in-

[2]Pulsed picoseconds neutron beams were recently generated. See [16].

elastic scattering events, which deposit a large amount of energy into the sample [19]. This problem is less severe with electrons as there are far fewer inelastically scattered electrons per scattering event.

One elegant way to fulfill the flux requirement and also prevent radiation damage is to use ultrashort bunches of x-rays, emitting from an x-ray free electron-laser (XFEL *plural:* XFELs) [20]. The flux from an XFEL is typically on the order of 10^9 photons per pulse (can also be higher), which is sufficient for obtaining a good quality diffraction pattern in a *single* shot, but the time span of the pulse is also short enough that it is possible to override the damage. An experiment that exploits this feature is referred to as "diffract before destroy" experiment [21]. The production of femtosecond x-ray beams by an XFEL is, however, non-trivial and requires large, expensive facilities such as those found at DESY in Hamburg [22] and LCLS in USA [23], with linear accelerators that are typically a kilometre or longer.

A possible cause of concern with the use of XFEL beams is the shot-to-shot fluctuation in the generated narrow-band, x-ray beam spectrum brought about by the generation process that uses self-amplified spontaneous emission (SASE), which is stochastic in nature [24]. When compared with XFELs, a synchrotron —which employs a ring accelerator, is able to provide a much more stable, broad-band beam of hard x-rays, but the shortest pulse durations from these sources are on the order of several picoseconds, which limits their scope for many ultrafast studies. The shot-to-shot fluctuations of a FEL can be accounted for by performing normalisation of the data, by measuring the spectrum of every x-ray shot. Recently, seeding them with an optical laser has been proposed as a possible solution to this issue [25]. Furthermore, a FEL is made up of many independent components such as undulators (a periodic structure of dipole magnets) and accelerators that must be made synchronous with one another and also with the external laser (excitation source for the pump-probe experiments) to be able to precisely clock the dynamics. This requires optical synchronisation control schemes [26], which not only add to the overall cost of running of a FEL, but

also can be time-consuming and challenging to implement. Moreover, one needs to apply for beam times to use these facilities for experiments, which not only can be a lengthy process, but also does not guarantee 100 % success rate. Lab-based sources producing femtosecond x-rays pulses from laser-generated plasmas are available and have been used to conduct femtosecond x-ray diffraction experiments with [27], but the hard x-ray intensity (efficiencies are on the order of 10^{-8}) is still not that which would make them a mainstay in the field.

Electrons beams, on the other hand, can be produced in femtosecond bunches fairly straightforwardly using laser-triggered photocathodes in table-top setups [28]. The laser used to generate the photoelectrons is always used to derive the pump beam, therefore electron probe beams are intrinsically synchronised with the pump laser. The wavelengths of the electrons are a lot shorter than x-rays (0.0335 Å for 120 keV compared to 0.1033 Å for x-rays) which, in theory, means higher spatial resolution. Furthermore, the charged nature of the electrons also makes them amenable to manipulation by electrostatic or magnetic fields, i.e. electron optics can be made to control and shape the beams, e.g. for imaging experiments such as in a transmission electron microscope (TEM). Imaging with the x-rays, on the other hand, is challenging because the focusing optics need to be fabricated in such a way that very small focal spot sizes (<10 nm) are realised at the sample position to achieve very high resolutions. This is made difficult by the high penetration depths (due to the scattering cross-sections) of the x-rays, which simply pass through most materials without bending. Focusing of the x-rays has typically been achieved by reflections off curved mirrors at grazing incidences or by multilayer Laue lenses (zone plates), which are mirrors that use layers of material off which the x-rays are diffracted. While progress is being made to make better and better optics, x-ray microscopes are yet to demonstrate atomic resolution [3]. However, the higher penetration depths of the x-rays gives them an advantage over the electrons; it is possible to perform experiments with thicker samples ($> 0.5\,\mu m$) and therefore, sample preparation for x-ray diffrac-

[3]The best resolution achieved to date was on the order of 5 nm [29].

tion experiments is less challenging. While on one hand, the charged nature of electrons can be advantageous, on the other it can pose some problems. Strong Coulomb repulsion between particles (space-charge effects) can lead to the loss of phase relationship (coherence) and can act to broaden the pulses, which can result in reduction of time resolution in time-resolved experiments [30]. In addition, the loss of coherence also means that time-resolved studies using electrons are, so far, only limited to crystals with unit cell dimensions on the order of few tens of angstroms (see chapter 5). Recently, Baum *et al* used *single* electron pulses to make the electron beam more coherent [31]. While, the space-charge effects can most certainly be eliminated by using very low beam currents, it comes at a cost of a huge reduction in flux and necessitates accumulations with multiple shots (often at high repetition rates to keep the acquisition times short) to buildup signal. This poses little to no problems for static measurements, but for time-resolved studies only completely reversible or rapidly exchanging samples (such as in gas-phase experiments) can be used. Other approaches to make the coherent electron beams concentrate on development of point-like sources [32, 33] and/or using high accelerating voltages [34]. X-rays remain the choice for ultrafast studies of large molecules, especially proteins using diffraction techniques. For the purposes of this thesis work, electron were used as the structural probe.

1.3 Development of time-resolved electron diffraction techniques

The first report of time-resolved diffraction studies using photoelectrons appeared in the early 1980s following the work by Mourou and Williamson [35]. In their experiment, an electron beam was used to probe the dynamics induced by a UV laser pulse in an aluminium foil. The pulse duration of the electron beam was on the order of 20 ps, as measured with a streak camera. This followed the efforts of Ishchenko *et al* to produce a short stroboscopic electron probe [36]. The Zewail group in Caltech produced femtosecond electron bunches for gas-phase

electron diffraction studies and managed to achieve picosecond resolution [37]. The main limitation to achieving femtosecond time resolution in their studies was the velocity mismatch between the laser pulse and the electron probe. The first study that brought the time-resolution to the sub-picosecond domain was the work of Siwick *et al* in 2003, who developed the concept of compact femtosecond electron sources, which when used with high accelerating voltages (60 kV in their case) made femtosecond electron diffraction (FED) experiments possible [38]. Since then, there have been a number of groups that have used femtosecond electron diffraction for studying number of interesting phenomena, from ultrafast melting in solids to chemical reactions in gas phase, with temporal resolutions ranging from a few picoseconds to one hundred femtosecond [39–43]. One study in particular that is both impressive and also relevant for this thesis work was that by Jean-Ruel *et al*, who studied the structural dynamics of diarylethene ring-closing reaction in the crystalline state [44]. Nowadays, ultrafast electron source development is an active area of research and many groups around the world are working towards improving the characteristics of electron beams for better temporal and spatial resolutions.

1.4 This thesis work

In the course of this PhD, a range of projects were undertaken, but the main focus of the thesis was on extending the capabilities of FED to study chemical reactions in crystalline media. The system chosen for this purpose was a spirooxazine compound that undergoes a photochromic reaction in the solution phase (see chapter 4). This project required the development of specific optical tools and acquisition schemes to control various aspects of the experiment. The approach that was developed was successfully tested in a proof-of-principle study using femtosecond spectroscopy. This forms an important part of the thesis report. Also reported are some results from a preliminary FED study of an organic salt, EDO-MeEDO-TTF that is believed to undergo a photoinduced phase transition.

The novelty of this system is that it is a 'doped' organic crystal, containing a stoichiometric mixture of two EDO salts.

1.4.1 Why solid state?

The preference of the solid state in the reported study over that of gas and liquid phases warrants some justification. For the case of the diffraction experiments, much higher signal-to-noise ratios can be achieved with solid samples, due to much higher density of molecules in a crystal than in gas or liquid phases. Due to the high achievable S/N and periodicity of the crystal lattice, it is possible to extract structural information with much higher resolutions. Moreover, except for only a couple of reported cases in the gas phase, femtosecond time resolution has mainly been achieved using crystalline materials. Liquid state FED is still largely in the development stage and as of yet, no time-resolved liquid phase FED experiment has been reported.

1.4.2 Organic crystals: challenges

Working with organic crystals is not without its challenges. Organic crystals consist typically of molecules made up of atoms with low atomic number (Z), such as nitrogen, carbon, oxygen and hydrogen, but sometimes may also contain heavy atoms like sulphur. Due to the relatively low density of the electron cloud surrounding these atoms, the interaction of the incoming electron beam with the charge cloud is much weaker when compared with molecules consisting of high Z atoms. As a consequence, these crystals generally scatter poorly. Moreover, the molecules in these crystals are held together by weak intermolecular forces, such as the Van der Waals forces. These forces are a result of fluctuating charge distributions which induce a dipole moment in the neighboring molecules. Due to the weak interactions, the molecules in the crystal can retain their individual character and so the crystals are sometimes termed as molecular crystals. These crystals are typically characterised by low melting points, poor thermal and electrical conductivities and moderate volatility, which makes them liable to thermal

and electrical damage. In order to work with these systems, different aspects, therefore, need to be managed. As the sample is irradiated with laser pulses to initiate the dynamics, it must be done at rates that allow the crystal to cool down/relax between shots. Typically, repetition rates below 100 Hz are used [4]. Moreover, the crystals need to be coherently excited to a level that the time-resolved signal can be recovered with sufficiently high signal-to-noise. Often, this requirement results in the fast onset of crystal damage and reversibility becomes a major issue (see chapter 4 for further discussion). All of this and the ultrashort pulse duration of the beam —which, recall, is analogous to the shutter speeds and results in low exposure (compare two cases in Fig 1.2), places a severe requirement on the flux. Very high density (high brightness) electron beams ($> 10^5$ electrons per pulse) must be used in order to provide adequate signal-to-noise in the experiment.

1.4.3 Thesis structure

This thesis is organised as follows. In chapter 2, an introduction to the basic physics behind ultrafast laser pulses is provided along with a discussion of the optical conversion schemes and a description of the laser system that drives the experiments. Chapter 3 details the theory underpinning transient absorption spectroscopy and introduces the experimental setup used in the thesis work. In chapter 4, details of the transient absorption measurements on crystalline spirooxazines are presented and the results are discussed in light of possible FED study. Chapter 5 provides a basic introduction to crystallography and reviews the theoretical and experimental methodologies of FED. Chapter 6 provides a description of femtosecond electron diffraction (FED) experiments performed on the EDO-MeEDO samples and finally chapter 7 concludes the thesis with an outlook on future experiments.

[4] Based on empirical observations.

Chapter 2

The Optical Setups

Almost all of the setups that are used in this thesis work rely on a femtosecond laser system providing short bursts of light, e.g. to trigger reactions, prepare states of interest and for the generation of photoelectrons for diffraction experiments. This chapter first introduces the basic concept of ultrashort laser pulses before providing a description of the laser system and nonlinear conversion schemes. The optical elements discussed here will become relevant in the subsequent chapters.

2.1 Ultrashort laser pulses

Ultrashort laser pulses are so called due to their extremely short pulse durations, which range in the picosecond (1 ps $=10^{-12}$ s) or shorter timescales. They have some interesting characteristics that distinguish them from pulses of other lasers. For example, they possess only a few optical cycles; an 800 nm laser pulse with a duration of 25 fs has a total number of 9 optical cycles. They also exhibit inherently broad spectrum due to the energy-time uncertainty[1] and can reach very high peak powers ($P_{\text{peak}} = \frac{\text{pulse energy (J)}}{\text{pulse duration (s)}}$, units Watts (W)).

[1]This differs from the quantum mechanical uncertainty as time is not an observable and has no quantum mechanical operator.

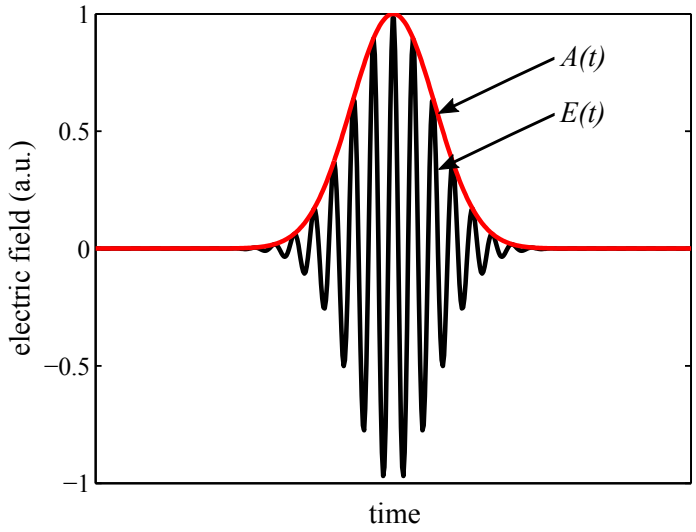

Figure 2.1: A graphical representation of an ultrashort pulse having a Gaussian profile. The electric filed, $E(t)$ is plotted in black and the electric field amplitude, $A(t)$ is shown in red.

The pulses can be described by the real electric field, $E(t)$ as

$$E(t) = A(t)\cos(\omega_o t - \phi(t)) \tag{2.1}$$

where $A(t)$ is the temporal envelope function that gives the absolute value of the electric field, $\phi(t)$ is the temporal phase, sometimes referred to as the carrier-envelope phase (CEP), which determines the relationship between the electric field and the envelope function and ω_0 is the carrier frequency, which is related to the colour (wavelength/frequency), υ_0 of the pulse

$$\omega_0 = 2\pi\upsilon_0 \tag{2.2}$$

When $\phi(t) = 0$ (see Fig 2.1), there is no phase delay between the electric field and the carrier envelope. It should be pointed out that most detectors (photodiodes, spectrometers) respond only to the intensity ($I(t) = |E(t)|^2$) of the pulses.

The field can equally be represented in the frequency domain by taking the Fourier transform of $E(t)$

$$E(t) = \frac{1}{2\pi} \int_{-\infty}^{+\infty} E(\omega) e^{-i\omega t} d\omega \tag{2.3}$$

and

$$E(\omega) = \int_{-\infty}^{+\infty} E(t) e^{i\omega t} dt \tag{2.4}$$

The equivalents of the intensity and temporal phase in the frequency domain are the spectrum and spectral phase [45]. The spectral phase, therefore, contains the frequency versus time information. In order to characterise the pulse completely, i.e. determine the pulse duration and the phase, spectral phase and time-dependent electric field must be known. Fortunately, techniques have been developed that are able to measure one or both of these two quantities. Most common ones are autocorrelation [46], frequency-resolved optical gating (FROG) [47] and spectral interferometry for direct electric-field reconstruction (SPIDER) [48].

A quantity, known as the time-bandwidth (TBW) product, is often quoted to indicate how close a given pulse is to being transform limited.

$$\Delta\omega \Delta t \geq K \tag{2.5}$$

where $\Delta\omega$ and Δt are spectral bandwidth and time duration measured at full width at half maximum (FWHM), respectively. The value K is different for different type of pulses as listed in Table 2.1.

Beam profile	K
Gaussian	0.441
Hyperbolic secant	0.315
Lorentzian	0.142

Table 2.1: Values of K relating to different pulse profiles.

A 25 fs Gaussian pulse ($K = 0.441$) has a bandwidth-limited spectral width of 17.6 THz (1 THz = 10^{12} Hz or s^{-1}).

2.1.1 Group velocity dispersion

As a natural consequence of their broad bandwidths, ultrashort pulses undergo a phenomenon known as group velocity dispersion (GVD), when they propagate through materials. In the medium, different frequency components of the ultrashort pulse experience different refractive indices causing them to travel at different speeds. These wavelength-dependent indices are responsible for variations in the temporal profile of the pulse such that the redder frequencies (longer wavelengths) travel at different velocities than the bluer (shorter wavelength) ones. When a transform-limited pulse propagates in a dispersive medium, it is said to become 'chirped' [2]. There are two scenarios depending on whether the material, through which the pulse propagates, is normally or anomalously dispersive. The pulse is said to become positively or up-chirped when passing through material with normal dispersion properties or negatively (down) chirped, when traversing an anomalously dispersive medium. In the latter case, the bluer frequencies travel faster than the redder frequencies. The GVD can be an undesirable effect, but fortunately can be compensated for by use of diffraction gratings [49] or prism pair [50].

2.1.2 Synthesis of ultrashort pulses

The synthesis of ultrashort laser pulses is accomplished by a process known as modelocking [51]. This process requires an optical resonator (or cavity) [52]. In the simplest case, the resonator cavity consists of two highly reflective, flat mirrors (of which one is slightly transmissive) that are placed in a linear arrangement and a gain medium for the generation and/or amplification of light, that is placed in between them. Light in the cavity is reflected back and forth making many passes through the gain medium. In the case, when the electromagnetic waves add up

[2]The chirp refers to case when $\phi_0 > 0$.

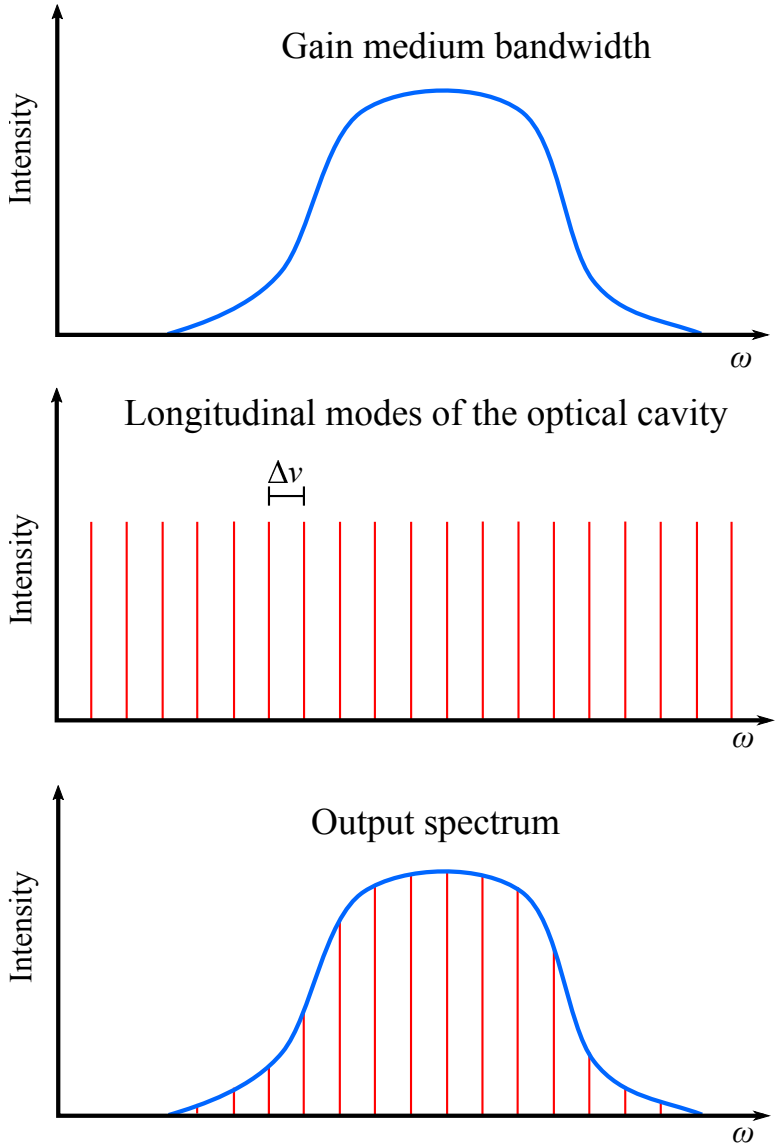

Figure 2.2: The cavity longitudinal modes selection by the gain medium.

constructively inside the resonator, a discrete set of standing waves, known as the cavity longitudinal modes are generated. The length of the resonator cavity, L defines the frequency separation between two adjacent modes ($\Delta\nu$) as

$$\Delta\nu = \frac{c}{2L} \tag{2.6}$$

where c is the speed of light. The repetition rate at which a laser operates is related to the round-trip time, T (where $T = \frac{2L}{c}$). The selection of modes for amplification is determined by the natural bandwidth of the gain medium. As Fig 2.2 illustrates, only those modes that fall within the bandwidth of the medium will get amplified.

The large number of modes present in the cavity (which fluctuate randomly in the CW operation) must be made to oscillate in phase in order for them to interfere constructively, i.e. modelocking. This can be achieved by installing an acousto-optic modulator (AOM) [53] or a saturable absorber [54] inside the laser cavity. These optical devices (through different mechanisms) cause the phases of the modes to be locked, leading to formation of ultrashort pulses. The process is said to be active or passive modelocking depending on whether the AOM (active) or a saturable absorber (passive) is used. A type of passive modelocking, known as Kerr-lens modelocking (KLM) [55], was discovered by Silbet *et al* in 1990 which does not require any saturable absorber [14]. Many ultrafast lasers today employ this scheme of modelocking. This method will be explained later on in the section on self-focusing.

2.2 Nonlinear optics

A rigorous treatment of the field of nonlinear optics is beyond the scope of this thesis. Only a general description of the relevant aspects will be provided to aid in understanding of the nonlinear conversion schemes.

Nonlinear optics is mainly concerned with the study of light-matter interaction, particularly when the intensity of the optical field interacting with the

material is sufficiently high —such as that may be found in a laser beam, that it distorts the electron density within the material causing it to become polarised [56]. Due to the induced nonlinear polarisation of the material, novel optical phenomena can be observed. For the case when the strength of the light field is low, the induced polarisation is written as [57]

$$\vec{P}(t) = \epsilon_0 \chi^{(1)} \vec{E}(t) \tag{2.7}$$

where ϵ_0 is the vacuum permittivity and the second term, $\chi^{(1)}$ is the linear electric susceptibility [3]. However, when the light field is of very high intensity then the induced polarisation can be written in form of power series as

$$\vec{P}(t) = \epsilon_0 \left[\chi^{(1)} \vec{E}(t) + \chi^{(2)} \vec{E}^2(t) + \chi^{(3)} \vec{E}^3(t) + \cdots \right] \tag{2.8}$$

where $\chi^{(n)}$ is the nth order nonlinear susceptibility. Higher order terms than $\chi^{(3)}$ are possible, but are less commonly encountered. Only processes relating to $\chi^{(2)}$ and $\chi^{(3)}$ will be described next.

2.2.1 Second harmonic generation

Second harmonic generation (SHG) is a process that is widely used throughout in the nonlinear optics field [58, 59] and many areas of physical sciences [60, 61]. The first discovery of the SHG process was made by Franken [62] in 1961, soon after the invention of the laser. In this process, two photons of frequency ω, via transitions involving virtual states in a nonlinear medium, are destroyed and a single photon of twice the frequency as that of the original photons is created. The energy is conserved in this process as illustrated in Fig 2.3a.

It is a χ^2 process that requires a second-order nonlinear polarisation to be induced in the medium

$$\vec{P}^2(t) = \chi^2 E^2(t) \tag{2.9}$$

[3] Simply, the electric susceptibility describes how strongly a material gets polarised when exposed to an electric field.

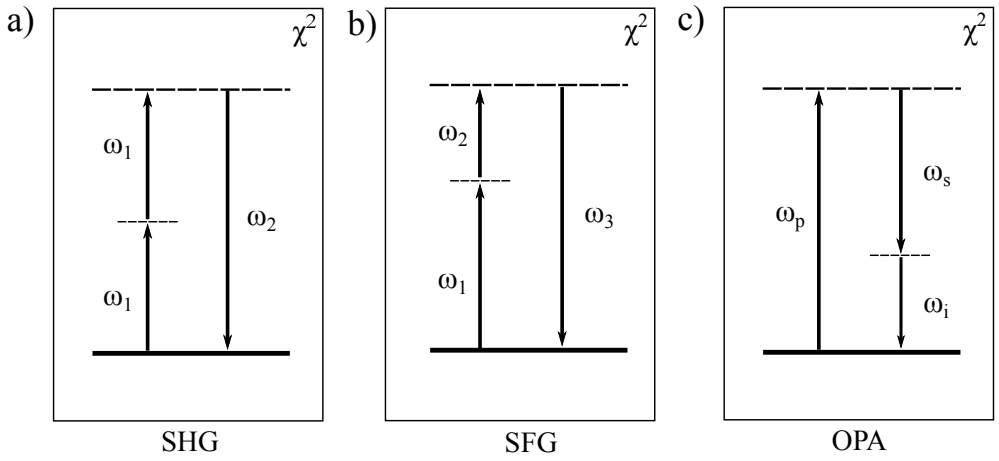

Figure 2.3: Energy level diagrams for different processes. a) The SHG process b) The SFG process c) The OPA process.

For any χ^2 nonlinear process to occur, the medium must be non-centrosymmetric, i.e. it must lack an inversion centre. Looking at Fig 2.3b, which shows the energy diagram for sum frequency generation (SFG)—also a χ^2 process, the energy conservation condition is written as

$$\omega_1 + \omega_2 = \omega_3 \tag{2.10}$$

which is also valid for SHG. In fact, SHG is a special case of SFG in which $\omega_1 = \omega_2$ and $\omega_3 = 2\omega_1$ [63]. When the second harmonic wave, 2ω is created in a medium, it does so with a perfect phase relationship with the ω wave. For the process to be efficient, the two waves must maintain this phase relationship, i.e. their phase velocities must be equal and remain constant otherwise destructive interference will make this process extremely inefficient. If a wave vector, $\vec{k}$ is assigned to the two fields to describe their propagation in the crystal, then the condition for conservation of momentum (phase matching) in SHG is given by

$$\vec{k_{\omega_2}} = 2\vec{k_{\omega_1}} \tag{2.11}$$

and since $\vec{k} = \dfrac{\omega n}{c}$ (c is the speed of light), the condition can only be fulfilled

when

$$n(\omega) = n(2\omega) \tag{2.12}$$

This is clearly not possible because the dispersion effects will prevent this from ever happening. A possible solution to overcome this limitation is in the use of birefringent crystals. This along with other practical aspects relating to SHG will be discussed further in the section on phase matching.

2.2.2 Optical parametric amplification

Optical parametric amplification [64] is the process in which a high intensity, high frequency photon, ω_{pump} transfers energy to a low frequency signal photon at ω_{signal} and a lower frequency idler photon is emitted at a difference frequency ω_{idler} (Fig 2.3c). As before, the energy and momentum are conserved.

$$\begin{aligned} \omega_{\text{pump}} &= \omega_{\text{signal}} + \omega_{\text{idler}} \\ \vec{k}_{\text{pump}} &= \vec{k}_{\text{signal}} + \vec{k}_{\text{idler}} \end{aligned} \tag{2.13}$$

A device that makes use of parametric amplification is called an optical parametric amplifier (OPA *plural*: OPAs). OPAs have been widespread in many areas of optical sciences, especially as sources of broadband tunable pulses [65].

2.2.3 Self-focusing

When the intensity of the laser beam reaches a so-called critical power, P_{critical}, a process known as self-focusing takes place in which the beam comes to a focus within the medium in which it is propagating [66]. This process is also called the Kerr-lens effect and is a consequence of the intensity dependent refractive index of the medium given by [67]

$$n(I) = n_0 + n_2 I \tag{2.14}$$

where $n(I)$ is the intensity dependent refractive index, n_0 the intensity independent refractive index and $n_2 I$ term denotes the second order nonlinearity. The

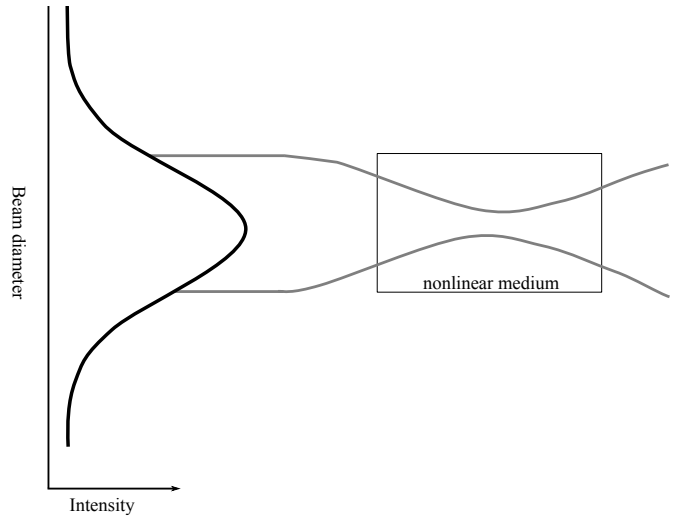

Figure 2.4: The Self-focusing effect.

critical power is given by

$$P_{\text{critical}} = \frac{\lambda^2}{2\pi n_0 n_2} \tag{2.15}$$

Consider a beam of a Gaussian intensity profile traveling through a nonlinear medium. As Fig 2.4 shows, the transverse intensity of the beam is not constant: the intensity is highest at the centre than at the peripheries, which leads to an increase of the refractive index of the medium at the centre, according to Eq 2.14. The non-uniform refractive index distribution across the medium causes it to act like a focusing lens[4]. Self-focusing is believed to be the triggering step in the generation of a supercontinuum [68, 69]. As was mentioned previously, the Kerr-lens effect can be used in the modelocking of the laser. This is described below.

To understand how the Kerr-lens effect can play a role in modelocking, it is useful to understand how passive modelocking using a saturable absorber works. The saturable absorber is often a semiconductor that responds to the intensity variation of the pulse by changing its transmission: absorption coefficient of the absorber decreases with increasing intensity, i.e. the absorber becomes more

[4]The origin of the word self-focusing is therefore due to this self-induced focusing by the pulse.

transparent at higher intensities. Therefore, a saturable absorber is used to suppress background (low intensity) fluctuating modes and permit only the modes that are of high intensity to be transmitted. Thus, the saturable absorber functions like a shutter and aids in the initiation of pulsing. In KLM, a Kerr-lens is created inside the gain medium leading to tight focusing from high intensity regions of the beam (reduction of the transverse mode size) and loose focusing at the wings (with corresponding CW powers). If an aperture is placed inside the cavity such that only the most intense part of the pulse is selectively focused by the Kerr-lens, a better overlap between the pump and the intracavity beam can be realised favouring pulsed operation. The aperture in this case is the gain medium itself and is called a soft aperture [70]. Lasers employing KLM are usually not self-starting, meaning that they do not spontaneously modelock [71]. Often a disturbance, introduced by jolting one of the end mirrors of the cavity for example, is needed to kick-start modelocking.

2.2.4 Self-phase modulation

Self-phase modulation (SPM) is yet another χ^3 process that occurs when a laser pulse propagating inside a transparent medium modifies the materials refractive index, which in turn modifies the phase of the pulse —differently for different frequency components contained in the pulse [72]. The results is a modulation the pulse spectrum. Again, this is a self-induced process and does not require the material to be dispersive (though they always are). The intensity dependent phase is defined by

$$\phi(t) = \frac{n_2 I(t) \omega L}{c} \tag{2.16}$$

where L is the length of the medium. The change of the phase in time as the pulse propagates in a medium is related to a change in frequency and so a concept of instantaneous frequency is developed. The instantaneous frequency is simply

the time derivative of the phase and is given by

$$\Delta\omega(t) = -n_2 \frac{dI(t)}{dt} \frac{\omega L}{c} \tag{2.17}$$

What Eq 2.17 essentially tells us is that as the pulse propagates in a medium, it is frequency shifted by an amount that is dependent on the intensity. Fig 2.5 shows the SPM of a pulse with a Gaussian intensity profile. The temporal variation in refractive index (due to temporal intensity changes) causes the leading edge of the pulse to experience a positive refractive index gradient and the trailing edge to experience a negative refractive index gradient. The pulse is slowed at the leading edge (frequency is decreased) and sped up at the trailing edge (frequency is increased), causing the overall spectrum to change and broaden. SPM is the main contributor to broadening in white light (WL) generation (see chapter 3).

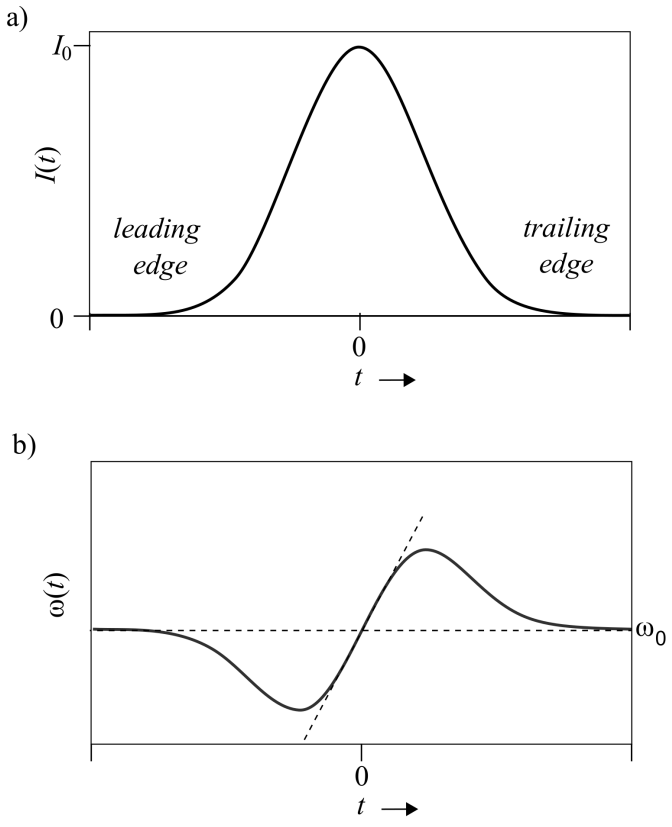

Figure 2.5: Self-phase modulation. a) The temporal intensity distribution of a Gaussian pulse b) The associated frequency shift. The leading edge is red-shifted and the trailing edge is blue shifted.

2.3 Phase matching

For the cases mentioned throughout this thesis, phase matching is achieved in a nonlinear solid-state optical medium [5], therefore, it is useful to discuss the symmetry aspects in relation to the crystals that can be used for harmonic generation. Crystal symmetries can be determined either by applying a set of operations that leave them unchanged using the group theory or by performing crystallographic measurements. Crystals are either isotropic, i.e. the index of refraction does not depend on the polarisation of the optical field or anisotropic in which the refractive index is polarisation dependent. Crystals that belong to the cubic system are always isotropic[6]. The anisotropic optical media are said to be birefringent because they exhibit the phenomenon of birefringence (double refraction) due to their polarisation dependent refractive indices. Keeping the discussion to birefringent crystals only, one typically encounters two types: uniaxial and biaxial birefringent crystals. Whether a crystal is uniaxial or biaxial depends on whether it possesses one or two optical axes, respectively. A beam travelling in a uniaxial crystal will get decomposed into two components: one will experience a constant refractive index, referred to as the ordinary refractive index, n_o whilst the other will experience a refractive index that is dependent on the angle which the beam makes with the optical axis, called the extraordinary refractive index, n_o. When $n_o > n_e$, the crystal is a negative uniaxial and conversely when $n_o < n_e$, it is called a positive uniaxial. It is quite routine to draw out a geometrical figure, called an indicatrix, to show how the refractive indices in an anisotropic medium differ from each other. As can be imagined, the indicatrix of an isotropic crystal will be spherical, because the refractive index is the same in all directions, but forms an ellipsoid for anisotropic crystals. Light incident at an angle to the

[5] A special case of phase matching called quasi-phase matching occurs in gases. High harmonic generation (HHG) is an example of this phenomenon [73].

[6] Due to the GVD, these material are unsuitable for phase matching.

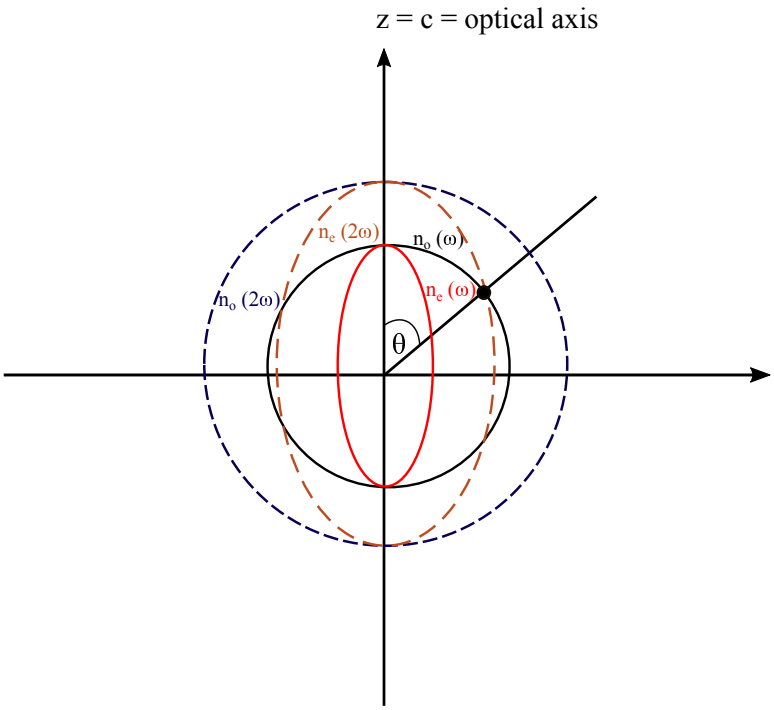

Figure 2.6: An indicatrix representation of the refractive indices in a negative uniaxial. For the SHG process, the angle θ can be exploited to fulfil the phase matching condition. The ellipses for the second harmonic wave are also drawn.

optical axis will experience a refractive index that is given by

$$\frac{1}{n_e(\theta)^2} = \frac{\sin^2\theta}{n_e^2} + \frac{\cos^2\theta}{n_o^2} \tag{2.18}$$

Now that we have defined what a birefringent crystal is, let's see how it can be used to create proper phase matching conditions for SHG process, i.e. $n(2\omega) = 2n(\omega)$. We shall consider a negative uniaxial such as beta barium borate, (β-BaB_2O_4, BBO), as it is the most common type used for SHG. Fig 2.6 shows the indicatrix with the ellipses corresponding to all the refractive indices of the waves that are involved in the process. As can be seen, by exploiting the angle θ that the incoming wave makes with the c-axis, the refractive index of the ordinary wave (fundamental) and the extraordinary wave (second harmonic) can be matched (the intersection point is shown with a black dot in the figure).

It should be pointed out that for SHG, two types of phase matching schemes can be realised in birefringent crystals: type I and type II. In type I phase match-

ing, the two input pulses have the same polarisations, whereas in type II, they are orthogonal. For example, for the SHG process the two phase matching schemes can be written as

$$\begin{aligned} n_o(\omega) + n_o(\omega) &= n_e(2\omega) \qquad \text{(Type I)} \\ n_o(\omega) + n_e(\omega) &= n_e(2\omega) \qquad \text{(Type II)} \end{aligned} \tag{2.19}$$

Either scheme of phase matching can be utilised, but which is eventually used will depend on the requirements for the desired application. To help one decide the scheme, the so-called effective nonlinear coefficient, d_{eff} (units pm/V), which describes the efficiency of the nonlinear interaction, can be looked up in any optical crystals handbook or from the excellent, free software called SNLO [74]. For example, for SHG of 800 nm, according to SNLO the d_{eff} is 2 pm/V for type I phase matching and 1.09 pm/V in case of type II phase matching. Therefore, type I phase matching is the favourable choice.

2.4 The laser system

The femtosecond laser in our lab is a commercial Legend Elite system from Coherent that uses Brewster-cut titanium doped sapphire (Ti:Sa) crystals as its gain media. It is comprised of an oscillator (Micra-5) producing a train of femtosecond pulses by Kerr-lens modelocking and a regenerative amplifier for pulse energy amplification. The oscillators gain crystal is pumped by the frequency-doubled output of a high power CW laser (Verdi, 1064 nm, 40 W), which employs a diode-pumped Neodymium Yttrium orthovanadate ($Nd : YVO_4$) crystal as the gain medium. The frequency doubling of 1064 nm light takes place inside a temperature-controlled lithium triborate (LBO) nonlinear crystal. The doubled output (532 nm) is strongly absorbed by the Ti:Sa crystal and results in the emission of light in the mid-infrared (MIR) region of the electromagnetic spectrum, i.e. 680-1100 nm. The pulse energies are on the order of 3-4 nJ. Table 2.2 lists the output of the Micra-5 oscillator. As mentioned above, the pulses from the oscillator are amplified in the regenerative amplifier system, which contains a

Central wavelength (nm)	800
Repetition rate (MHz)	85
Spectral bandwidth (nm)	100
Pulse duration (fs)	30 (FWHM)

Table 2.2: The Micra-5 oscillator output.

stretcher, whose function is to temporally elongate the pulses from femtoseconds to picoseconds duration, a regenerative cavity where the actual amplification takes place and finally a compressor to return the pulses back to femtosecond durations. The pulse stretcher uses all reflective optical elements to prevent chromatic aberrations and is designed from a single diffraction grating, a spherical mirror and a set of plane mirrors. Fig 2.7 shows the schematic of the pulse stretching system. A femtosecond pulse incident on the diffraction grating is spectrally dispersed, vertically displaced by the curved mirror and via reflections off the plane mirrors makes four passes through the stretcher. The grating is configured so that the short wavelength component travels further through the stretcher than the long wavelength components, thus lengthening the pulse. This step of stretching the pulse before it enters the regenerative amplifier cavity is necessary because with femtosecond laser pulses (due to their ultrashort pulse durations), very high peak intensities (up to $700\,\mathrm{GW\,cm^{-2}}$) can be attained during the amplification process, which could lead to damage of the optical components and the gain crystal. In the amplification stage, the chirped pulse is introduced into the regenerative cavity made up of yet another Ti:Sa crystal placed in an optical resonator, a pair of optical switches to control the injection and extraction of the beam and some polarising elements. The schematic of the regenerative amplifier is depicted in Fig 2.8.

An electro-optic modulator (EOM) called the Pockels cell, synchronised with the pulse train of the oscillator, in combination with polarisation optics, picks and traps a single pulse from the train of pulses for amplification in the resonator cavity. The pump for the Ti:Sa crystal in the cavity is derived from an intracavity

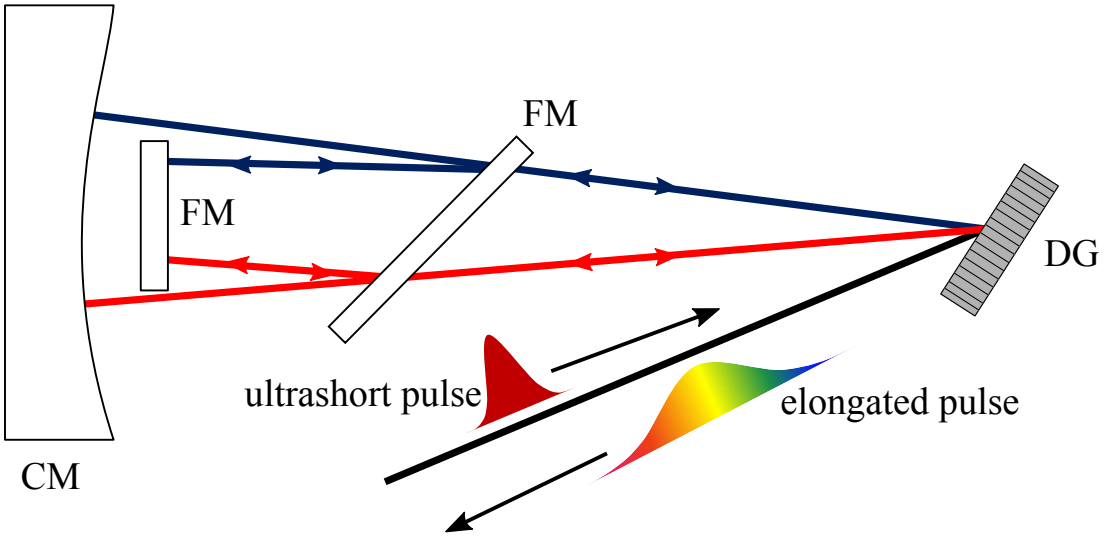

Figure 2.7: Femtosecond pulse stretching principle. Beam entering the stretcher is spectrally dispersed by the grating and after multiple passes leaves the stretcher with the red part exiting first. DG: diffraction grating; FM: flat mirrors; CM: curved mirror.

doubled output of a Neodymium-doped yttrium lithium fluoride (Nd : YLF) based Q-switched laser, which delivers 532 nm nanosecond pulses with pulse energies up to 12-20 mJ, operating at 1 kHz repetition rate, to the crystal. The trapped seed makes multiple passes through the Ti:Sa rod, extracting some energy from the pumped crystal with each pass. Once most of the stored energy has been extracted, the Pockels cell changes the polarisation of the amplified pulse, such that it exits the cavity. After amplification, pulses with energies on the order of a few millijoules are compressed back to the femtosecond durations by a dual-grating compressor. The final output of the regenerative amplifier is as follows: $\lambda_{\text{central}} = 800$ nm, 4 mJ at 1 kHz and 40 fs pulse duration [7]. This process of amplification by first stretching (chirping) the pulse is known as chirped pulse amplification (CPA) [35].

[7]This value is quoted from the factory specifications. It was not measured.

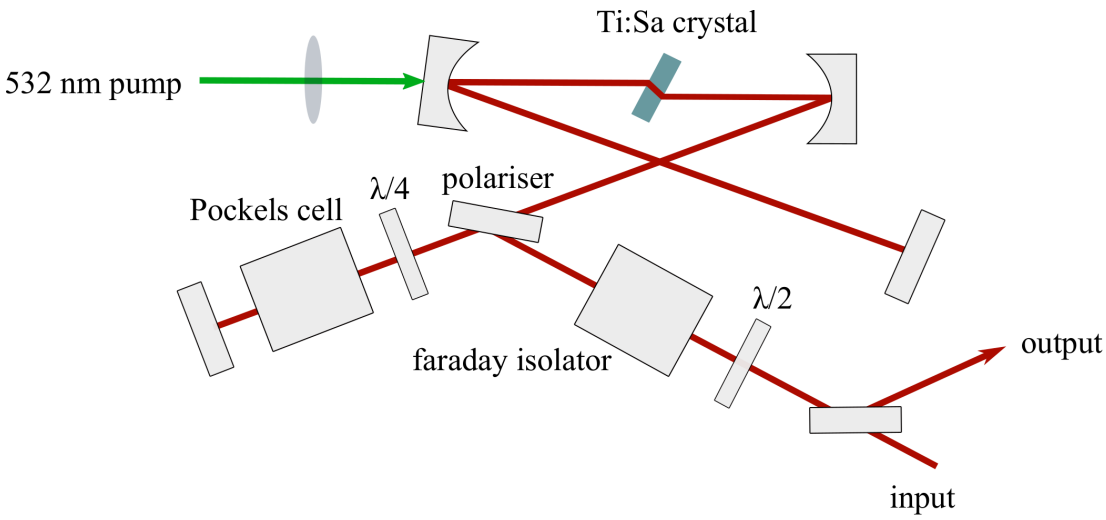

Figure 2.8: The schematic of the regenerative amplifier.

2.5 Non-collinear optical parametric amplifier

The first demonstration of a non-collinear optical parametric amplifier (NOPA, *plural*: NOPAs) was provided by Gale and co-workers [75]. It differs from the collinear case of OPAs in that it can be used to generate ultrabroadband, and hence, extremely short pulses. This section explores different aspects relating to the construction of the NOPA. The main reason for building the NOPA will be revealed in the subsequent chapters.

2.5.1 The pump

Energy conservation dictates that only those photons which have frequencies lower than the pump are amplified. Therefore, the choice of the pump will depend on the application, i.e. what frequencies one wishes to generate and amplify. The NOPA in our lab was build to be tunable in the visible region (450-700 nm) of the electromagnetic spectrum and, therefore, a pump of wavelength 400 nm, generated by SHG of the fundamental frequency of the amplifier output, was chosen. The required SHG crystal angle was calculated by rearranging Eq 2.18

for θ

$$\theta_{\mathrm{pm}} = \sin^{-1}\sqrt{\left(\frac{n_e(2\omega)^2\left(n_o(2\omega)^2 - n_o(\omega^2)\right)}{n_o(\omega)^2\left(n_o(2\omega)^2 - n_e(2\omega^2)\right)}\right)} \tag{2.20}$$

Inputting the values of the polarisation dependent refractive indices (Table 2.3) into Eq 2.20, yielded a value of $\theta_{pm} = 29^o$.

Index of refraction	Value
$n_e(\omega)$	1.5462
$n_e(2\omega)$	1.5687
$n_o(\omega)$	1.6614
$n_o(2\omega)$	1.6934

Table 2.3: The values of refractive indices used in Eq 2.20. The values were taken from [76].

2.5.2 The seed

The seed in the NOPA is a broadband supercontinuum or white light (for spectrum in the visible). The WL generation is a result of several χ^3 nonlinear processes, some of which were discussed in previous sections including SPM and self-focusing, taking place concurrently. Other processes that are thought to also play a role include Raman scattering [77] and four-wave mixing [78]. The choice of the medium supporting these processes must be such that it gives the desired white light spectrum. Sapphire (Al_2O_3) was chosen in our case because it is the most commonly used material for a stable continuum in the visible region and has a large transparency window (0.17 µm to 5.5 µm).

2.5.3 The mixing crystal

To achieve phase matching in the parametric process, the refractive index experienced by the pump in the mixing medium needs to be smaller than that of the seed and idler beams, i.e. anomalously dispersive conditions are needed or else the

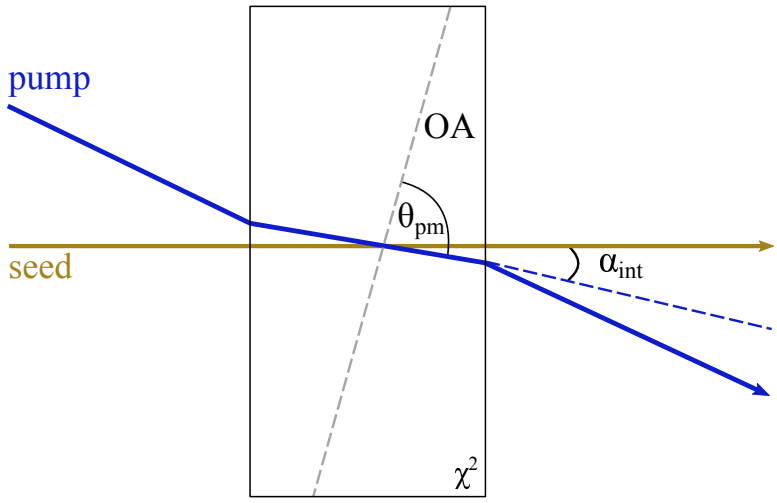

Figure 2.9: The mixing geometry used in the NOPA. OA is the optical axis.

phase overlap will be quickly lost. Therefore, the choice of the crystal should be such that it meets the above requirement. As alluded already, using a birefringent crystal will take care of this condition. Moreover, the crystal should not absorb the generated idler and signal photons: it needs to be transparent across all colours of idler and signal photons and it must (ideally) have a high damage threshold and respond weakly to environmental factors, such as temperature and pressure.

A BBO crystal satisfies all of the above requirements for the mixing medium and was, therefore, used for amplification of the seed light. The required angle needed to amplify in the visible region was calculated by using the expression given in [79] for the geometry shown in Fig 2.9.

$$\theta_{\text{pm}} = \sin^{-1}\left[\left(\frac{n_{op}^2}{n_p^2} - 1\right)^{1/2} \cdot \left(\frac{n_{op}^2}{n_{ep}^2} - 1\right)^{-1/2}\right] \tag{2.21}$$

where n_p is given as

$$n_p = \frac{\lambda_p}{\lambda_s} n_{os} \left(\cos\left(\alpha_{\text{int}}\right) + \sqrt{\frac{\lambda_s^2}{\lambda_i^2}\frac{n_{oi}^2}{n_{os}^2} - \sin^2\left(\alpha_{\text{int}}\right)}\right) \tag{2.22}$$

The subscripts *s, p, i* correspond to the parameters relating to signal, pump and idler photons, respectively. The refractive indices of the signal and idler photons

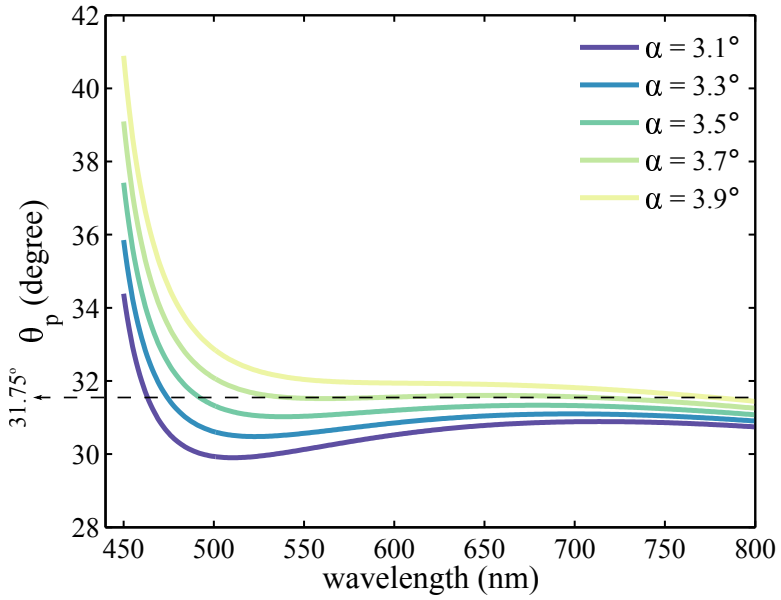

Figure 2.10: Calculated phase matching curves for different internal angles. With an internal angle of 3.7° corresponding to an approximate cut angle of $\theta_{\mathrm{p}} = 31.75^{o}$, broadband amplification can be achieved as indicated by the dotted line.

were calculated using Sellmeier equations for a BBO crystal [80]. The calculated phase matching curves are plotted in Fig 2.10 for different internal angles, α_{int} which is the angle that the pump beam makes with the signal inside of the crystal. As can be seen, to achieve broadband phase matching (the curve with the flattest region over a large wavelength range), a crystal cut at approximately $\theta_{\mathrm{pm}} = 32°$ is required.

The external angle that the pump beam should make with the seed beams is then easily calculated by applying Snell's law

$$\theta_{\mathrm{ext}} = \sin^{-1}\left(\frac{n_{\mathrm{BBO}(\lambda_{\mathrm{pump}},o)}\sin(\alpha_{\mathrm{int}})}{n_{\mathrm{air}}}\right) \tag{2.23}$$

which results in a value of approximately 6 degrees. Therefore, the optimum cut angle of a BBO crystal is 32° and the external angle between the seed and pump beams should be 6 degrees.

2.5.4 Other considerations

The sizes of the pump and probe beams should be comparable, with the seed beam spot size at the crystal slightly smaller than the pump beam size. One should be aware that when very small beam sizes are used, the fluence ($F = \frac{\text{pulse energy (J)}}{\text{spot area (m}^2\text{)}}$) can become very high, which can lead to instabilities in the output and can also damage the crystal. The beam sizes should, therefore, be chosen wisely. The optics used to achieve the necessary beam size can be transmissive (lens) or reflective (spherical mirrors), depending on what is available and acceptable. Transmissive optics will introduce more chirp (but are easier to align) to the beam than reflective optics and consequently, the output spectrum will be narrower than in case of reflective optics. With spherical mirrors, the chirp is completely avoided [8], but the alignment can be more challenging and require more space. Finally, the mixing crystal thickness is another factor that needs to be taken into account. A compromise between the efficiency and the GVD is sought, so that one gets the maximum efficiency and the shortest pulse possible. While one can certainly perform simulations to determine the optimum thickness, a 1 mm crystal was used in our NOPA.

2.5.5 The NOPA Setup

The design principles of building a NOPA were discussed above. This section provides details of its construction. The NOPA design was mainly based on the one from Riedle [82]. The schematic of the NOPA setup is presented in Fig 2.11. A fraction of the fundamental output of the regenerative amplifier (800 nm, 200 µJ, 40 fs pulse duration) having horizontal (denoted *p*, for parallel) polarisation was sent through a half-wave plate (HWP1) to change the polarisation state to vertical (denoted *s*, from German 'senkrecht' meaning perpendicular). The *s*-polarised beam was then split into two arms using a beam splitter (BS), with a splitting ratio of 90 % and 10 % for transmission and reflection, respectively. The

[8] Though not all mirrors will do that. Chirped mirrors for instance introduce negative GVD and are used in some commercial ultrafast compressors [81].

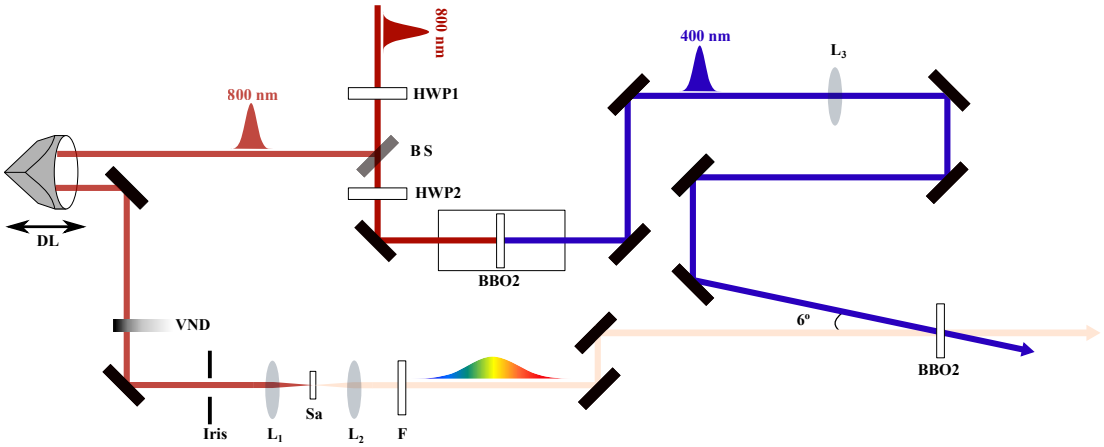

Figure 2.11: The schematic of the NOPA built in the lab. BS: beam splitter HWP: half-wave plate, VND: variable netural density filter,L_1= 75 mm, L_2= 35 mm, L_3= 750 mm, DL: delay line, F: cut-off filter.

transmitted beam was sent to the SHG stage for pump generation and the reflected 10 % was directed towards a delay stage (DL) and used for the creation of the seed. The reflected beam was selected for seed generation to avoid dispersion.

The SHG stage consisting of a BBO crystal (BBO1, 29.3°, 1 mm, type I) generated the 400 nm pump with an efficiency of 30 %. The power of 400 nm in this arm was controlled by using a HWP as follows: The *s*-polarised 800 nm was sent to the BBO1 for harmonic generation and the output was optimised by angle tuning of the crystal. After maximum efficiency was achieved, the crystal was fixed and not rotated anymore and a HWP2 was installed before the crystal. By rotating the HWP2 now, only the 800 nm photons that had the correct polarisation for efficient phase matching through the BBO1 generated 400 nm photons. This allowed to control the power of the generated beam that now had *p*-polarisation. The residual 800 nm was filtered out by using a set of dichroic mirrors optimised to reflect 99 % of 400 nm light. In the seed arm, the WL supercontinuum was generated by focusing 800 nm beam into a sapphire disc (Sa, 2 mm) using a fused silica convex lens (L_1, focal length = 75 mm) mounted on a translational stage. A variable neutral density (VND) filter and an iris were

placed in the path of the beam to adjust the pulse energy and change the beam diameter, respectively. Initially, very low pulse energies (<1 µJ) were used to generate the supercontinuum. The iris was left fully open at this stage, but the focal spot of the input beam at the sapphire was adjusted by translation of the lens L_1 until a weak yellow-whitish spot started to appear behind the crystal. At this stage, the translation of the lens was stopped and the VND filter wheel was rotated to increase the pulse energy until a uniform white beam, with a green outer ring around it, was formed. The iris was closed slightly to remove the outer ring and produce a single stable filament. The energy of the pulse used to generate the filament was measured to be approximately $\sim 2\,\mu J$. Fig 2.12 shows the spectrum of the generated continuum. The residual 800 nm was filtered off using a short-pass filter (F, $\lambda_{\text{cut-off}} = 700$ nm) and the resultant seed was focused at the amplifier crystal using a fused silica lens (L_2, focal length = 30 mm). Once both the pump and the seed beams had been generated, it was time to mix them in the amplifier crystal, which in this case was another SHG crystal for 800 nm (BBO2, 30°, 1 mm, Type I)[9]. However, before doing that, the pump was focused (L_3, focal length = 750 mm mounted on a translational stage) $\sim$ 20 mm [10] before the amplifier crystal in the absence of the seed. By adjusting the focal spot through translation of the lens, and varying the pump power [11] (by increasing it slightly), weakly coloured rings behind the crystal became visible (see Fig 2.13b). The rings were optimised (made brighter) by rotating the crystal and combined to give one solid-red ring by tilting the BBO2 crystal about the vertical axis. This was done by keeping the pump power constant. The rings appear due to a process known as superfluorescence and hence are called superfluorescence rings [83]. It is a result of the pump photons spontaneously splitting to give signal and idler photons that extends out of the crystal in a cone. Considered to be a

[9]This was the only crystal available at the time in our lab that closely matched the required cut angle. The crystal was tilted slightly for optimum interaction. A crystal with cut angle of 32° was ordered later.

[10]focusing the pump beam inside the crystal was avoided lest it got damaged.

[11]the pulse energy was not exceeded above 25 µJ.

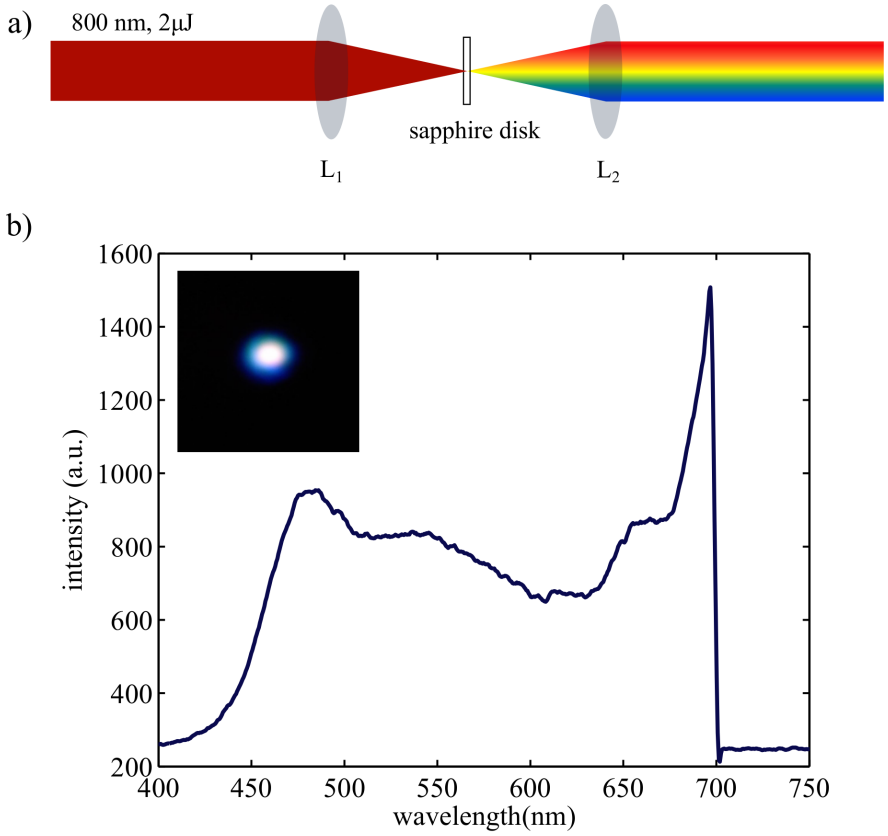

Figure 2.12: a) The schematic of white light generation process where L_1= 75 mm and L_2 = 30 mm. b) Spectrum of the generated supercontinuum. The sharp cut-off is due to the short-pass filter. The inset shows a photograph of the projection of the continuum on a screen.

completely quantum mechanical effect with no classical analogue, this process can conveniently be used to assist with the alignment of the pump with the seed. By spatially overlapping the seed beam with the pump beam on the crystal surface and also ensuring that it lies on the superfluorescence cone behind the crystal, the mixing angles can be correctly set. This process does require several iterations of correcting the overlap inside the crystal and adjusting the pump-signal angle so that the seed is always on the superfluorescence ring.

After the crossing angles had been properly set ($\sim 6^\circ$), the delay of the white light seed with respect to the pump was changed using the DL, until temporal overlap with the 400 nm pump inside the crystal was established. This led to an amplification of the seed in the range from 510-700 nm and disappearance of

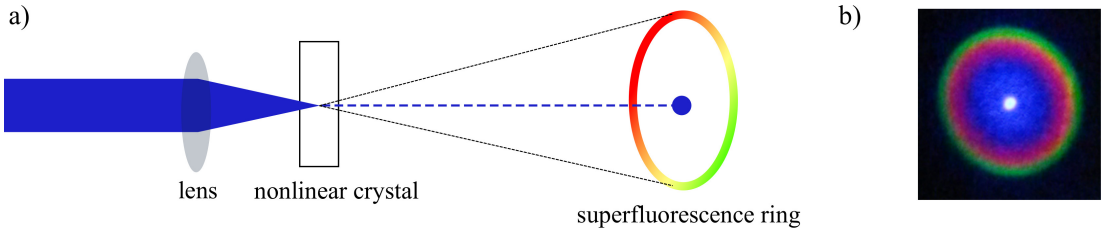

Figure 2.13: a) The schematic of generation of the fluorescence ring by focusing the 400 nm pump in the BBO crystal and b) A photograph of the ring generated in the setup. The central part shows the residual pump beam.

the fluorescence ring as shown in Fig 2.14. A colour filter ($\lambda_{\text{centre}} = 600$ nm, bandwidth = 25 nm FWHM) was added at the exit to select the frequencies of interest needed for experiments in the chapter 4. The energy of the pulses after filtering was measured to be $\sim 0.8\,\mu$J.

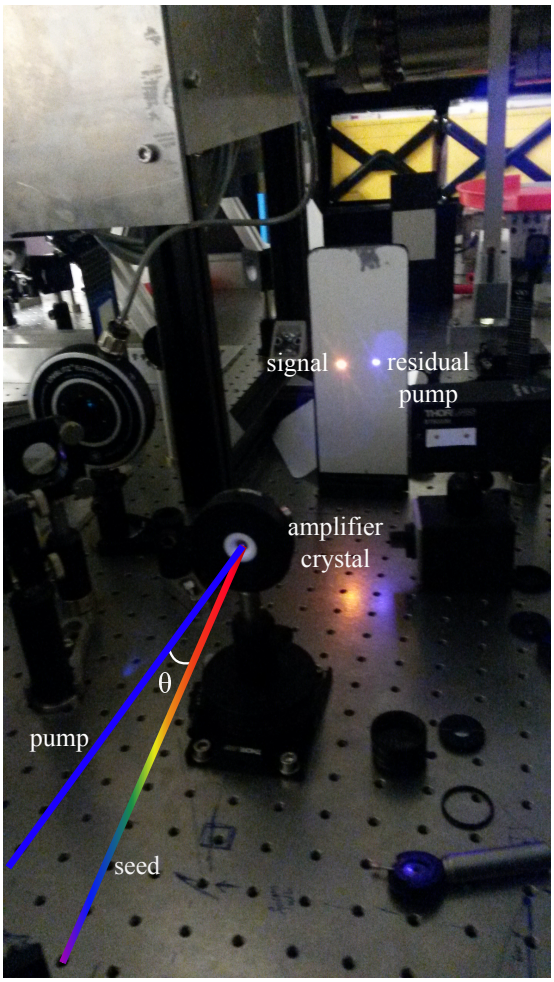

Figure 2.14: The amplification process. The superfluorescence ring is significantly depleted and the seed is amplified.

Chapter 3

Elements of Transient Absorption Spectroscopy

Ultrafast transient absorption (TA) is a nonlinear optical [1] spectroscopic technique that has been employed for studying many photochemical and photophysical processes that are of interest in physical and material sciences [84]. It is capable of providing dynamical information on the ultrafast processes with extremely high temporal resolution. The objective of this chapter is to introduce various concepts relating to transient absorption and also to describe the setup that was used to carry out experiments reported in chapter 4 of this thesis. The chapter is structured as follows: the first section provides a basic introduction to photochemistry and a section outlining different photochemical processes follows it. Afterwards, detailed descriptions of the transient absorption and related setups are provided and finally sections regarding the characterisation of the setup conclude the chapter.

[1] Transient absorption can also be performed using a beam of x-rays as the probe.

3.1 Photochemistry

The study of chemical reactions that occur due to absorption of light is called photochemistry. Atoms and molecules can absorb a photon if the energy separation between the ground and excited states of the system matches exactly the energy of the photon. One uses the time-independent Schrödinger equation to calculate the energies of the states

$$\hat{H}\Psi(\vec{r},\vec{R}) = E\Psi(\vec{r},\vec{R}) \tag{3.1}$$

where $\Psi(\vec{r},\vec{R})$ is the total molecular wave function, $\vec{r}$ and $\vec{R}$ represent, respectively, the coordinates of all electrons and nuclei, E is the energy and $\hat{H}$ is the Hamiltonian of the system defined as

$$\hat{H} = \hat{T}_N + \hat{T}_e + \hat{V}_{Ne} + \hat{V}_{ee} + \hat{V}_{NN} \tag{3.2}$$

In Eq 3.2, $\hat{T}_N$ is the kinetic energy operator for the nuclei and $\hat{T}_e$ is the kinetic energy operator for electrons. The last three terms are the potential energy operators relating to the Coulombic interactions (attraction and repulsion) between the nuclei and electrons, electrons with electrons and the nuclei with nuclei, respectively. Eq 3.1 is an example of an eigenvalue equation.

It turns out that solving Eq 3.1 is not possible for systems consisting of more than one electron without invoking some approximations, i.e. analytical solutions only exist for one electron systems. A powerful approximation used in quantum chemistry is the Born-Oppenheimer (BO) approximation, which essentially takes note that the electrons are about three orders of magnitude lighter than the nuclei ($\mathrm{m_e} = 9.1 \times 10^{-31}$ kg, $\mathrm{m_p} = 1.67 \times 10^{-27}$ kg ; $\dfrac{\mathrm{m_p}}{\mathrm{m_e}} \sim 1835$ .16) and can respond much more quickly as compared to the motions of the nuclei [85]. This makes it possible to factorise (separate) the molecular wave function into electronic and nuclear parts as

$$\Psi(\vec{r},\vec{R}) = \chi_N(\vec{R})\psi_e(\vec{r};\vec{R}) \tag{3.3}$$

χ_N is the nuclear wave function and $\psi_e(\vec{r}, \vec{R})$ denotes the electronic wave function. The electronic wave function depends on the coordinates of the electrons, $\vec{r}$ and also parametrically on the nuclear coordinates $\vec{R}$, i.e. there is a different electronic wave function for each arrangement of the nuclei. The Hamiltonian can be now written by considering only the electronic wave function.

$$\hat{H}\psi_e(\vec{r}, \vec{R}) = E(\vec{R})\psi_e(\vec{r}; \vec{R}) \tag{3.4}$$

By applying the BO, the potential energy surfaces can be constructed by calculating the electronic wave function as a function of R. The BO is sometimes also called the adiabatic approximation and breaks down whenever there is mixing between electronic states, resulting in conical intersections, which facilitate radiationless decay [86]. A related concept to BO is the Franck-Condon rule, which states that due to the large disparity in masses, the nuclei remain stationary during electronic excitations and only rearrange after the transition has taken place [85, 87]. This implies that, if the equilibrium geometry of the excited state differs from that of the ground state, the molecule will find itself in a vibrationally excited level. The population of the vibrational states in the excited electronic state is governed by the overlap between the vibrational wave functions in the ground and excited electronic states.

3.1.1 Photochemical pathways

When a molecule absorbs a photon, it acquires a new energy state that has a finite lifetime. The photophysical pathways available to the molecule after it has been excited are summarised in an energy level scheme called the Jablonski diagram, shown in Fig 3.1 [88, 89]. Four different electronic states are depicted as thick lines and additionally for each state, a stack of levels are drawn on top. These correspond to the vibrational states, characterised by vibrational quantum numbers, v. In addition to the vibrational states, there are also many rotational states with designated rotational quantum number J, but they have been omitted from the diagram.

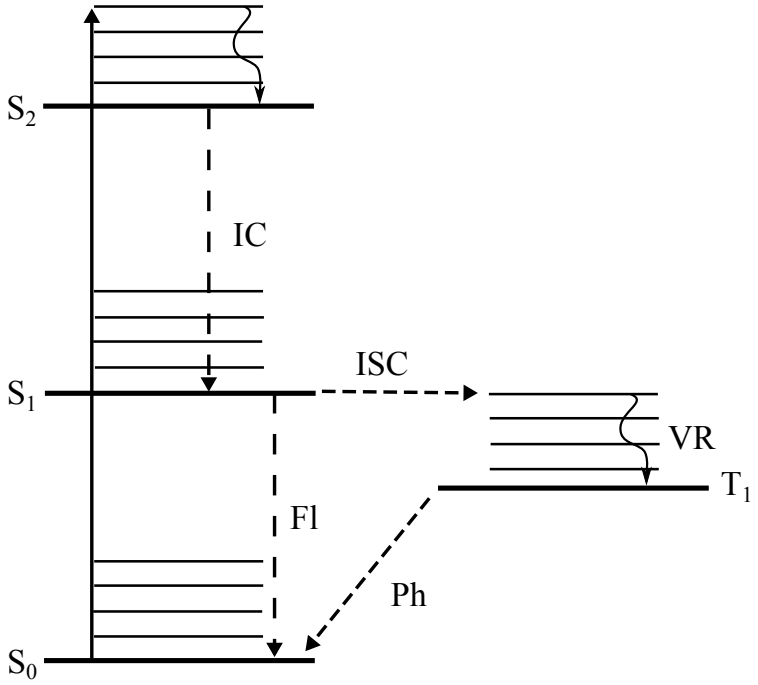

Figure 3.1: The Jablonski diagram showing different photochemical pathways. VR: vibrational relaxation; IC: internal conversion; ISC: inter-system crossing; Fl: fluorescence; Ph: phosphorescence; S: singlet state; T: triplet state.

Following the absorption process, an electron is promoted from the lowest-lying state (often the ground vibrational state of the ground *electronic* state, which for closed-shell systems is a singlet state, i.e. total spin is zero, denoted S_0) to a higher energy state. The figure shows that the absorption process takes the molecule from the ground electronic state to the second excited singlet state via a $S_0 \rightarrow S_2$ transition. Excitations to levels lying lower or higher in energy than S_2 will depend on the energy of incoming photon. It should also be mentioned here that, in reality, the electronic states are not necessarily well separated in energy as they are shown in the figure. For the sake of introducing concepts and terminologies, it is also assumed that the excitation to the S_2 populates a high energy vibrational level of the state. Highly excited vibrational states are often referred to as 'hot' states. Vibrationally hot molecules will tend to release the excess vibrational energy and relax to the lowest vibrational level in a given electronic state. This process is known as vibrational relaxation (VR) and proceeds

without release of a photon. In the condensed phase, the released energy can lead to fast thermalisation of the environment (the bath), especially in case of strong system-bath coupling or the energy goes mainly to the internal modes of the molecule, in which case the process is called intramolecular vibrational relaxation (IVR). Another deactivation process closely related to VR is internal conversion (IC). This process involves a vibrational transition between two electronic states of the same multiplicity, i.e. the spin state is preserved in the process. The probability of the process depends on the Franck-Condon overlap as discussed in the previous section. It should be mentioned that internal conversions between electronically excited states generally occur faster than from $S_1 \rightarrow S_0$ because the energy gap between S_1 and S_0 is often larger than between high-lying states. IC is often followed by VR, which demotes the electron to the lowest vibrational level of the S_1 state. As with VR, internal conversion is a radiationless transition. From this point, there are two pathways that are accessible to the molecule. It can either make a transition to the lowest electronic state, $S_1 \rightarrow S_0$, in which case the process is known as fluorescence (Fl) or it can change its spin state and make a transition to a triplet state (a state in which the spins of two electrons are parallel) via $S_1 \rightarrow T_0$, in which case the process is called inter-system crossing (ISC). Fl always results in the emission of a photon, while ISC is a non-radiative process. The selection rules actually forbid the transition from a singlet to a triplet state, making ISC extremely inefficient, but the process can occur (and also be fast) if the spin-orbit coupling between the states is strong. This is commonly encountered in molecules containing heavy atoms, like bromine. From the T_0 state, the molecule can return to the ground electronic state, S_0 by an emissive process known as phosphorescence (Ph). Fl and Ph occur predominately from the lowest-energy excited states of a given multiplicity of the molecule. This is the Kasha's rule [90]. The typical timescales of the photochemical processes are given in Table 3.1. It should be kept in mind that electronic transitions also involve vibrational transitions, termed vibronic. Rotational transitions also accompany vibronic transitions, but they are often unresolved in experiments involving con-

Process	Timescale (s)
Absorption	10^{-15}
Vibrational Relaxation	10^{-10}
Internal Conversion	$10^{-14} - 10^{-11}$
Intersystem Crossing	$10^{-8} - 10^{-3}$*
Phosphorescence	$10^{-4} - 10^{-1}$
Fluorescence	$10^{-9} - 10^{-7}$

Table 3.1: Photochemical processes and their approximate timescales. * may also be faster.

densed media.

3.2 Transient absorption spectroscopy

As has been mentioned already, transient absorption is a pump-probe technique in which one beam (the pump) is used to create an excited state population and another (the probe) is used to measure the absorption spectrum of the transient species. A transient absorption signal is obtained by measuring the optical density (OD) of the sample before interaction with the pump laser, $\mathrm{OD_{OFF}}$ corresponding to the absorption of the ground state and comparing it with the absorption spectrum of the pumped sample, $\mathrm{OD_{ON}}$ (see Eq 3.6).

The expression for optical density is given by the Beer-Lambert law [91]

$$\mathrm{OD} = -\log\left(\frac{I}{I_0}\right) = \varepsilon c l \tag{3.5}$$

where I_0 and I are the intensity of the reference (incident) beam and the beam that interacts with the sample, respectively, l is the thickness (or path length) of the sample, c is the concentration of the absorbing solution and ε is called the molar extinction coefficient (commonly given in units of $\mathrm{mol^{-1}cm^2}$), which provides a measure of the strength of optical absorption.

A transient absorption spectrum can be measured by recording the difference optical density as a function of wavelengths and time delays as

$$\begin{aligned} \Delta\mathrm{OD}(\lambda, \Delta t) &= \mathrm{OD}_{\mathrm{ON}} - \mathrm{OD}_{\mathrm{OFF}} \\ &= \log\left(\frac{I_{\mathrm{OFF}}(\lambda)}{I_{\mathrm{ON}}(\lambda, \Delta t)}\right) \end{aligned} \tag{3.6}$$

where Δt is the time delay. $\Delta\mathrm{OD}(\lambda, \Delta t)$ is often plotted as a 2D map, in which the wavelengths (λ) are arranged as rows and the columns represent the time delays. A trace taken along a selected wavelength is called a kinetic trace and provide the time evolution information, while a 1D plot taken at a particular time delay (also called a spectral trace) gives the transient absorption spectrum.

3.2.1 Types of signals

The transient absorption spectrum contains four main types of signals, distinguished by the region of the spectrum at which they appear and/or the signs of the ΔOD. When the sign of ΔOD is positive, it corresponds to an increase in the absorption and it is negative due to an overall decrease in absorption. It is important to understand what photophysical processes contribute to these signals. A simple scheme is shown in Fig 3.2 that relates the type of signal to the photophysical processes. The signals that can be observed are: ground state bleach (GSB), excited state absorption (ESA), stimulated emission (SE) and photoproduct absorption (PA). Ground state bleach and stimulated emission have negative signs of ΔOD, while the excited state and photoproduct absorption are positive signals.

3.2.1.1 Ground state bleach

Ground state bleach refers to the process in which the population of the molecules in the ground electronic state is depleted (due to the absorption process) and higher energy states are populated. As a result, the concentration of the species in the ground state capable of absorbing photons from the probe laser is reduced, which leads to $\mathrm{OD}_{\mathrm{ON}} < \mathrm{OD}_{\mathrm{OFF}}$ and therefore, ΔOD becomes negative. This

GSB signal is observed in the wavelength region of the ground state absorption of the molecules under investigation.

3.2.1.2 Stimulated emission

An excited molecule can radiatively decay to a lower energy level by a process known as spontaneous emission. However, if during this time, a photon should arrive with energy that matches the energy gap between the populated excited state and the ground state, a process resulting in the emission of a photon takes place. It is known as stimulated emission. In TA spectroscopy, SE is induced by a photon from the probe beam. The emitted photon travels in the same direction as the probe beam, towards the detector, leading to an increase in the number of photons impinging on it —such as would be in the case of reduced absorption, so that the OD_{ON} is again lower than OD_{OFF} resulting once more in the negative sign of the ΔOD. The spectral profile of the emitted signal follows that of the fluorescence spectrum of the species being studied and is typically red (Stokes) shifted with respect to the ground state bleach.

3.2.1.3 Excited state absorption

Electrons in the excited states can be promoted to even higher states, if they absorb photons of appropriate energy from the probe beam. This leads to the case where $OD_{ON} > OD_{OFF}$ in the region of excited state absorption and a positive ΔOD signal is observed. The ESA signal need not only come from the singlet excited states absorbing photons. States of other multiplicities, e.g. triplet states (if they can be accessed) can also absorb a photon from the probe and will give a positive signal in the TA spectrum.

3.2.1.4 Photoproduct absorption

Products from a photochemical reaction can give rise to the emergence of yet another positive feature in the transient absorption spectrum provided that the probe beam has photons with energies in which the products absorb.

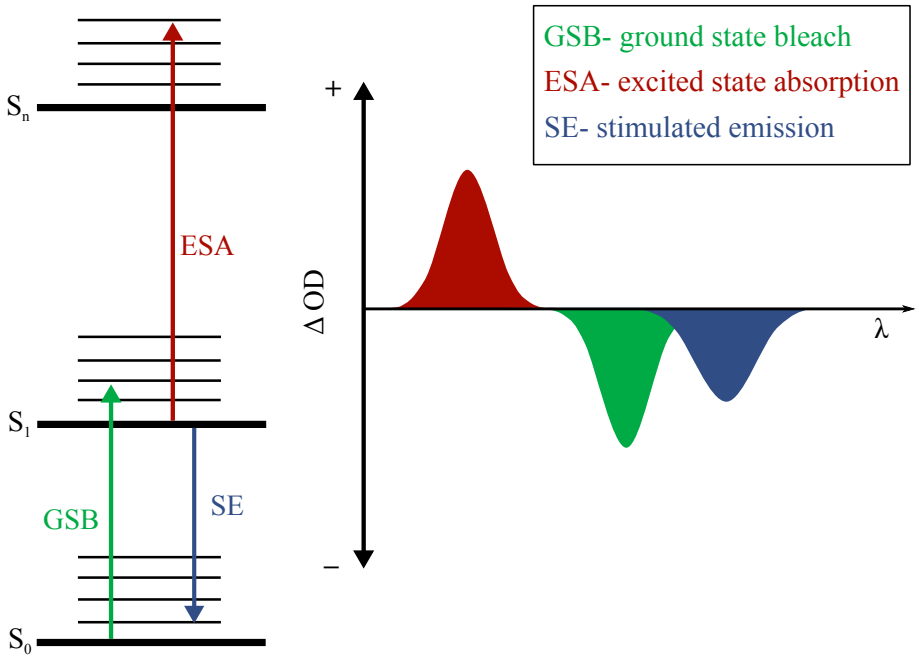

Figure 3.2: Typical signals observed in a transient absorption spectrum.

Generally, the signals mentioned above are observed as overlapping to some extent with each other, which complicates the interpretation of dynamics from the transient spectra. It is therefore important to separate out the underlying components by modelling the transient absorption data. A good starting point is to use the steady (ground) state absorption/fluorescence spectra to assign some of the signals, but a more rigorous (global and target) analysis is often necessary [92, 93].

3.2.2 Sample preparation

Before describing the instrumentation relating to the optical pump-probe setup, the method for sample preparation is presented. Almost all of the experiments reported in this thesis either require or make use of crystalline samples. The crystals for the experiments are typically grown in-house —except in the case that they are supplied, and sliced to sections thinner than 500 nm (the reason for this will be explained later). In order to cut the crystals, we use a crystal thinning technique widely used by electron microscopists, called ultramicrotomy [94]. The

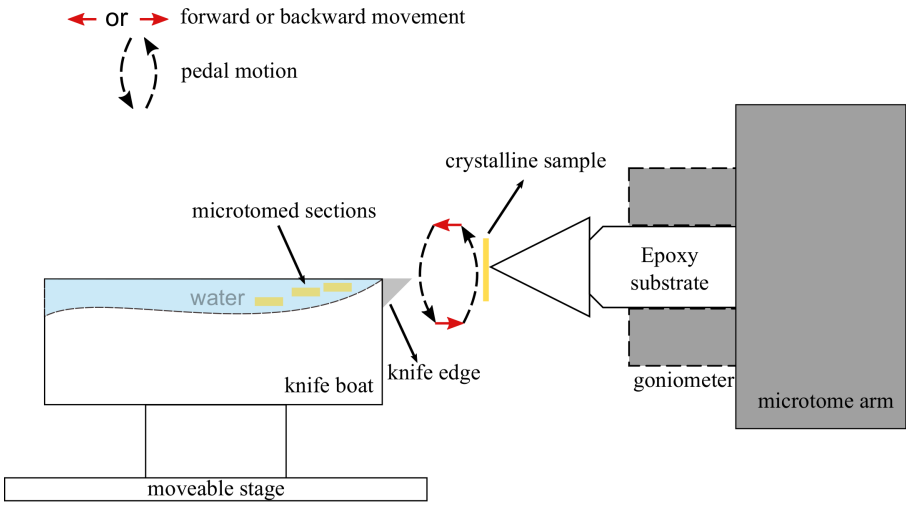

Figure 3.3: The microtomy process. The microtome arm moves towards the knife edge until contact is made with the surface. The arrows indicate the directions of motion of the microtome arm.

microtomy process is illustrated in Fig 3.3. The ultramicrotome in our lab is equipped with a sample holder assembly, a movable stage, a microtome knife for cutting the crystals and an optical microscope for viewing. It is fully automated and can perform cuts as thin as 30 nm. The procedure for cutting the samples is as follows: the crystal to be cut is first glued onto an end of a trimmed (in shape of trapezoid) epoxy resin block, which is then inserted in the sample holder. For small crystals ($< 0.5 \times 0.5$ mm (W $\times$ H), assuming rectangular shape), a pyramidal shaped substrate is used together with the epoxy block and the crystal is fixed to pyrimids apex. After mounting the sample, the holder is attached to the microtome arm supplied with a goniometer (an instrument which allows precise 360° rotation of the specimen). The boat (anodised rectangular block with a trough) is placed on a movable stage, with the knife edge facing the sample, and clamped. The knife edge is made of diamond. Different types of knives can be used depending on the hardness of the material being cut. Diamond is the choice for our work as it can be used for cutting various materials with different values of hardness. For coarse adjustment, the boat is manually translated to bring the knife edge to within a millimeter of the crystal surface. The crystal can be

Figure 3.4: The ultramicrotome in action. Shown are the sections of the spirooxazine crystals.

rotated using the goniometer and is aligned with respect to the knife edge. After the orientation of the crystal is set and the knife edge properly aligned with one of the crystal faces, the trough is filled with clean water until the level is just on the edge of the knife. If too much water is added, a lint-free tissue paper is used to draw some water from the boat. The objective is to produce a low meniscus with the edge of the knife. The desired settings (thickness, cutting speeds) are entered in the controller and the cutting process is initiated. The sample holder starts moving towards the knife in step sizes defined by the desired crystal thickness as set by the user. After each step, the microtome arm moves up and down in a pedal-like fashion. Once the contact between the crystal surface and the knife has been made, sections are created that slide into the boat and can be picked up with a picking tool (a stainless steel loop) for mounting on a glass slide or a

TEM mesh (for diffraction experiments). Fig 3.4 shows the ultramicrotomy of spirooxazine crystal —the system of interest in chapter 4.

3.2.3 Steady-state absorption measurement

It was stated before that the ground state absorption can be used as the first step towards disentangling the different signal contributions in the transient absorption spectrum. For static (ground state) absorption measurements of the samples in solution phase, it is routine to use a commercial spectrophotometer. By measuring the transmission of light through the sample and separately through the solvent used to make up the solution and by comparing the recorded intensities according to Eq 3.5, the absorption spectrum can be easily generated. A spectrophotometer is typically composed of a light source (a continuous lamp), a monochromator, a sample compartment and a detection system. The light source can be chosen such that it emits radiations of the desired wavelengths. The monochromator is made up of a grating, which disperses light into many diffraction orders, and a slit to select the wavelengths. The monochromatic beam passes through the sample and the transmitted beam intensity is measured by a photoreceiver. An issue of using the commercial spectrophotometer in our lab is that the size of the beam (which forms the shape of a vertical line) at the sample position is about 10 x 1 mm. But, absorption measurements of crystals require that the size of the beam be smaller than the physical dimensions of the sample. This is because the probe light must illuminate the crystal evenly and in cases when the beam sizes are larger than the crystal, only that portion of the beam that passes through the sample is attenuated (due to absorption), whereas the rest of the beam reaches the detector unaltered (assuming that the scattering is ignored), leading to erroneous measurements. Large beams can be shaped to small sizes by using a small pinhole (placed in front of the sample), but this inevitably leads to a significant reduction of the incident photon intensity. The crystals used in this thesis work were much smaller than the sizes mentioned above. Therefore, a spectrometer based on the design of Kirchner *et al* [95] was

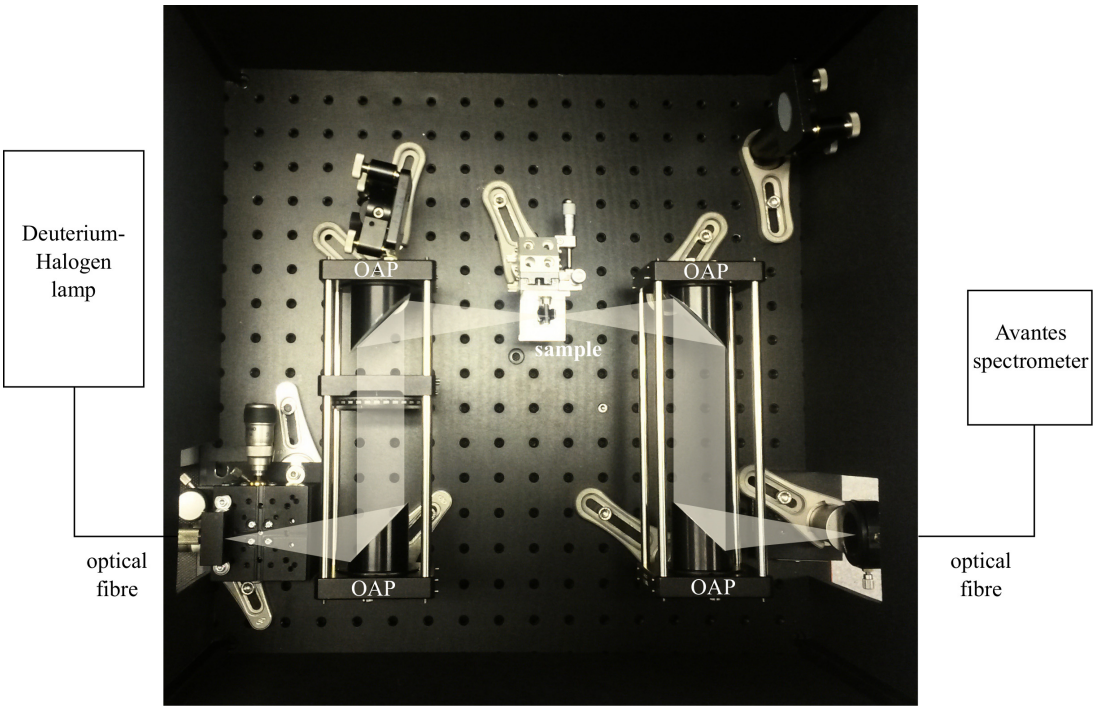

Figure 3.5: The spectrometer mainly designed for measurements of crystalline samples. The sample is placed near the focal point of the off-axis mirror. Also shown are two flat mirrors, which direct a laser beam entering from the top left corner of the figure to the sample position for pump ON-OFF absorption measurements. OAP: off-axis parabolic mirror.

built by Dr Corthey in order to measure absorption spectra of small crystalline samples. Fig 3.5 shows a photograph of the spectrometer. The setup consists of four aluminium 90° off-axis parabolic mirrors (OAP, focal length = 10 cm) mounted on a breadboard and used for collimation or focusing of light. Using mirrors of the same focal length allowed a one-to-one mapping of the beam sizes from the input to the sample position. Two lamps: deuterium and halogen, function as the light source, with the deuterium lamp emitting continuous radiation in the UV range (215-400 nm) and the halogen lamp covering 400-2500 nm. An optical fibre (100 µm core diameter) guides light from the lamps into the setup. The first OAP collimates the input beam and directs it towards the second OAP, which focuses it at the sample (placed near the focal point of the mirror). The light trans-

mitted through the sample is collimated and coupled into another optical fibre (400 µm), which sends it to a commercial spectrometer connected to a computer. The fibres are mounted on a XYZ stage for precise alignment. The all-reflective design allows a broadband wavelength coverage and the focusing can take place without chromatic aberrations, i.e. tighter focus than with a lens. The spectrometer can also house more optics. For example, a laser beam can be coupled into the setup and mirrors placed inside can be used to direct the beam at the sample. This permits time-averaged pump-probe (laser ON and OFF) measurements. As before, measuring the absorption spectrum involves recording the transmitted intensities through the sample and through the substrate/solvent-filled cuvette. All the measurements are performed in the *transmission* geometry.

3.2.4 Reversibility

It is often desirable to perform pump-probe experiments using multiple laser shots at high rates of repetition because the intensities of the laser pulses tend to be less fluctuating and therefore more correlated over short intervals, which can yield good signal-to-noise ratios. In addition, the acquisition times are shorter, which prevent situations such as laser drifts and sample decomposition (in case of sensitive or volatile samples). Moreover, multi-shot experiments allow repeated measurements for building up statistics. Having said that, it is not always possible to run (shot-to-shot) experiments at repetition rates higher than a few kHz. The limitation comes from either the detection instruments, which have finite data readout times, or due to the long relaxation times (after excitation) of the system being studied. In any pump-probe experiment, the system under investigation must return to its initial state between pump laser shots, within the period of the repetition rate. This is the *reversibility* condition and must be satisfied in all cases. This requirement is conveniently fulfilled for measurements involving solutions or gas phase samples by flowing them fast enough so that the probe volume is completely refreshed between laser shots. This is clearly not possible for solids, making their studies much more challenging than gas or solution phase.

Unsurprisingly then, a large body of work is available in literature in which transient absorption spectroscopy or similar pump-probe techniques have been applied that use either solution or gas phase samples. Solid state materials are widely used in ultrafast research in the field of condensed matter physics. However, cases where the photodynamics of chemical reactions occurring in the solid state are probed are rather scarce in comparison. In photochemical reactions, such as those that lead to dissociation of bonds or those that involve structural transformations, products are created that permanently blend with the original reactants in the solid state. As mentioned above, the sample must be reversible to able to faithfully study the dynamics of interest using pump-probe methods. The permanent buildup of photoproducts renders systems irreversible and the studies of many chemical reactions in solid state intractable with multi-shot pump-probe approaches. In addition, other factors that can compound the studies of chemical reactions in solids are low optical and thermal damage thresholds. This is particularly problematic in molecular crystals.

Photochemical reactions taking place in the solid state can be exploited to fabricate dynamic devices, which may be controlled and used for many everyday applications. Also, microscopic understanding of the reactions can provide chemists with clues that can help them to create conditions that help steer reactions towards desired pathways, thereby increasing yields in some solid state reactions. Therefore, there is a need to develop methods that permit non-invasive ultrafast studies of solid state chemical reactions. One approach for doing that calls for translation of the sample, so that the pump laser interrogates a new portion of the sample at every (new) shot. The sample can also be replaced completely after (a few) laser shots. In either case, a large, homogeneous sample area for probing (in the former case) or many high quality, identical samples (in the latter case) would be required (a non-trivial task, especially if it requires synthesis of exotic and complex systems). Samples that are completely irreversible, i.e. those that are irreparably damaged after a single pump shot, must be studied with *single-shot* methods. A single-shot scheme that has been used for ultrafast solid

state studies of chemical reactions employs an echelon (a stepped grating) in the setup [96]. In this scheme, the sample is pumped and the probe (to monitor the change in the sample) is first dispersed into many delayed replicas by the echelon (the delay between the pulses is generated due to the probe travelling a variable amount through the echelon) and then imaged onto the sample. A large time window can be covered in a single shot. The strength of this method is that one avoids measuring signals from damaged regions, but as can be imagined, a single shot can not yield sufficiently high signal-to-noise ratios to unambiguously characterise the sample response and consequently many runs are often required to buildup signal well above the noise floor. Furthermore, the echelon limits the use of very broadband probe pulses and the experiment must be repeated several times (over a range of wavelengths) to obtain complete spectral information. That said, this method is the only choice when experiments with irreversible systems need to be performed. On the other hand, some systems *are* photoreversible, even in the solid state, and by paying attention in ensuring that the buildup of products is kept under check, can be studied using multiple-shot pump-probe methods. For example, Jean-Ruel *et al* exploited solid state photoswitching to study the ultrafast ring-closing dynamics of diarylethene using pump-probe techniques [97]. They excited the system using a UV laser and measured the dynamical response using a WL or electron probe, but before repumping, used a CW helium-neon (HeNe) laser to convert the molecules back to their original form, thereby ensuring reversibility up to at least 1000 pump laser shots. A couple of aspects were critical for the success of their experiments, namely the repetition rate and the degree of the structural change associated with the reaction. The repetition rate of the pump laser was kept very low (effectively 1.9 Hz) in their experiments, which allowed ample time for the CW beam to convert molecules back and furthermore, the structural change in the crystal was fairly moderate, which would have helped preserve the periodic order. Unfortunately, applying this strategy is not possible for every photoreversible system; other systems exist (of which one is the topic of the next chapter) that show a much larger structural transformation,

which calls for the extension of the approach of Jeal-Ruel in order to make a generic method for ultrafast studies of solid-state photoreversible reactions. This will be discussed further in chapter 4, but next the setup is described.

3.3 The transient absorption setup

The transient absorption experiments were performed using a home-built setup, featuring a broadband probe to simultaneously monitor different photophysical processes (by covering a large spectral window) and a NOPA (see chapter 2). The design of the setup was fairly flexible in that it could be used to run both crystalline state and solution phase experiments. It was also possible to integrate a third (NOPA) beam into the setup as will be described below. A schematic of the setup is shown in Fig 3.6. A portion of the fundamental output of the regenerative amplifier (800 nm, 40 fs) operating at 1 kHz was divided into two beams using a beam splitter (BS1). One of the beams was used to pump the NOPA and the other beam (henceforth referred to as the main beam) was sent to the transient absorption setup. This created two independent arms that not only allowed running the experiments with more than two beams, but also with beams having different repetition rates with respect to each other. The repetition rate of the main beam carrying approximately 200 µJ of energy was modulated after sending it through a series of two synchronously running optical choppers (rotating wheels with slots in them).

This beam was then split by another beam splitter (BS2) into two parts. The reflected part of the beam carried 90 % of the energy (180 µJ) and formed the pump arm of the TA setup, while the 10 % transmitted beam (20 µJ) was used to generate the probe light.

The weak beam was guided by a set of reflective dielectric mirrors towards a computer controlled mechanical delay line (DL, 30 cm travel range). The delay line —used to vary the optical path length of the probe beam with respect to the pump beam, consisted of a gold-plated retroreflector mounted on a movable stage.

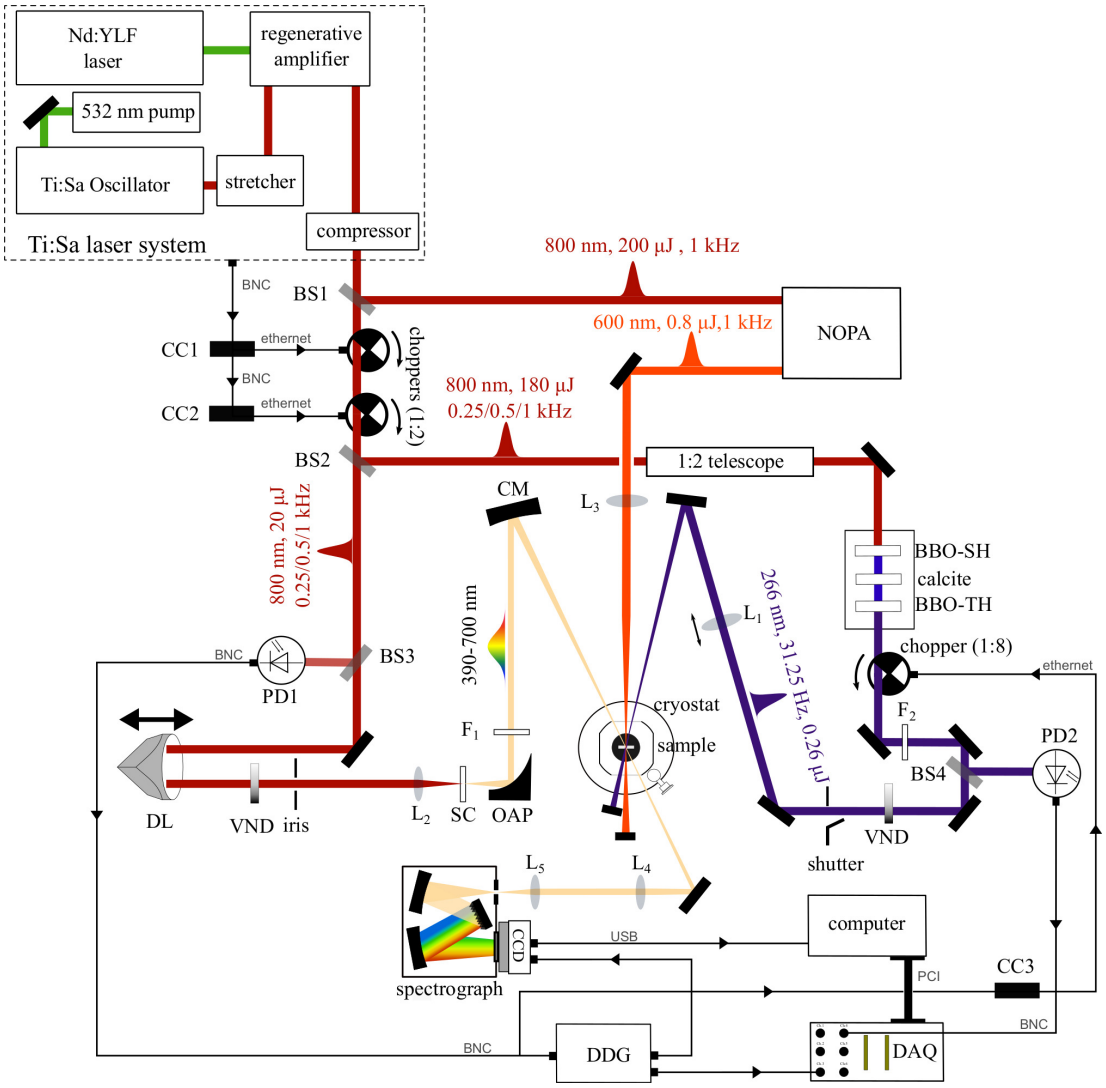

Figure 3.6: The transient absorption setup. BS: beam-splitters; CC(1 & 2): chopper-controller; PD: photodiode; DL: delay line; VND: variable neutral density filter; SC: supercontinuum; OAP: 90° off axis parabolic; DDG: digital delay generator; DAQ: data acquisition card; F: cut-off filters; L: lenses; CM: curved focusing mirror.

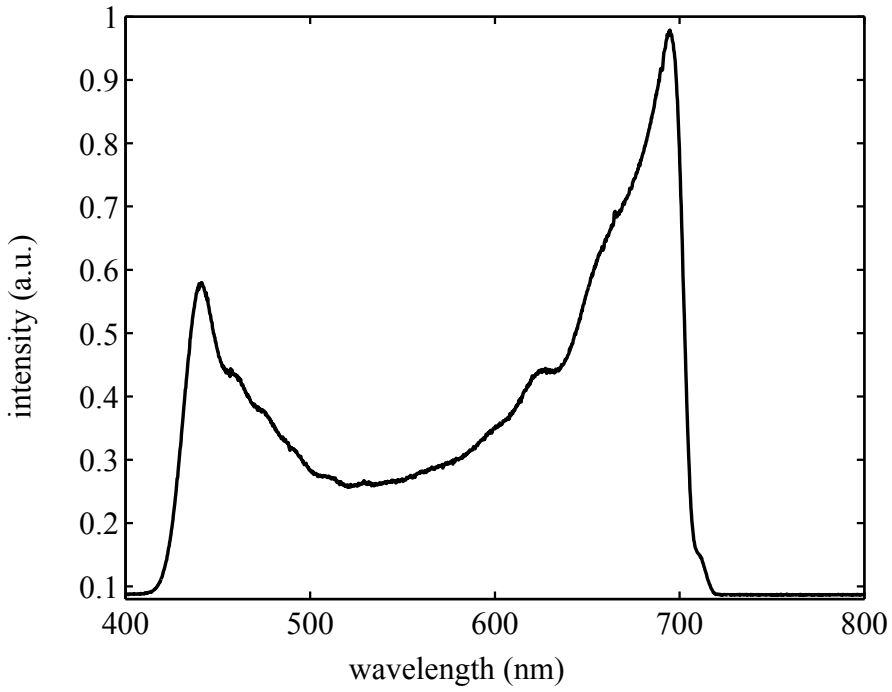

Figure 3.7: The white light continuum spectrum generated by focusing 800 nm in water.

The beam made three reflections inside the retroreflector before being sent in the direction of the WL generation stage. Prior to WL generation, the intensity of the beam was attenuated using an absorptive neutral density filter (VND) to a pulse energy of approximately 2 µJ before being focused inside a cuvette (SC, 2 mm path length), filled with ultrapure water, by a lens (L_2, focal length= 50 mm) to generate a stable WL beam with wavelengths spanning 390-900 nm (see Fig 3.7). The size of the beam before the lens was controlled by an iris. The diverging WL was collimated by a 90° off-axis parabolic mirror (OAP, focal length = 50 mm) and a short-pass filter (F_1, $\lambda_{\text{cut-off}}$ = 700 nm) removed the residual 800 nm light. A concave mirror (CM, focal length = 150 mm) was used to focus the supercontinuum at the sample. Reflective optics were used for collimation and focusing of the WL beam in order to prevent further broadening/chirping. In the pump arm, the fundamental light was frequency-tripled in a process referred to as third harmonic generation (THG), by mixing 800 nm and 400 nm beams inside a BBO crystal as follows: The diameter of the 800 nm beam was first

reduced from 10 mm to 5 mm [2] using a Galilean telescope made from two lenses of focal lengths 200 mm and -100 mm and separated by 100 mm from each other. After the telescope, the 800 nm laser beam was frequency-doubled in a doubling crystal (BBO-SH, $\theta_{\text{cut}} = 29.3°$, 1 mm, Type I). The doubled output (400 nm) was maximised by angle-tuning of the BBO-SH crystal and mixed with the residual 800 nm beam inside a sum frequency generation crystal (BBO-TH, $\theta_{\text{cut}} = 55.5°$, 1 mm, type II). To compensate for the mismatch in the propagating speeds of the two beams prior to mixing in the BBO-TH crystal, a birefringent calcite crystal ($CaCO_3$, 1 mm, $\theta_{\text{cut}} = 45°$) was deployed in which the beams experience different refractive indices, owing to their different wavelengths and polarisations [3]. After passing through the calcite crystal, the two collinear beams were sent into the BBO-TH crystal and 266 nm photons were generated with an efficiency of 4 %. The unconverted 400 nm and 800 nm beams were removed from the generated 266 nm beam using a combination of a short-pass filter (F_2, $\lambda_{\text{cut-off}} = 350$ nm) and harmonic separators. A VND was placed in the beam path to control the intensity and in addition a manual shutter was used to let the beam pass and hit the sample only during data acquisition. Focusing of the pump beam at the sample was achieved by a lens (L_1, focal length = 300 mm) mounted on a translational stage.

The generation of the NOPA beam was discussed in the previous chapter. The output of the NOPA was tuned to give the required central wavelength and was focused on the sample using a lens (L_3, focal length = 300 mm). The path length of the NOPA beam was set such that it was delayed by approximately 10 nanoseconds (1 ns = 10^{-9} s) with respect to the probe beam. The reason why this was done will become clear in the next chapter.

For solution phase experiments, an in-line UV quartz, flow cell (path length 0.5 mm) was used. The sample solution was flowed through the cell using a miniature flow pump. The cell was mounted on a translational stage (which

[2] in order to increase the fluence at crystal to achieve high conversion efficiencies.

[3] Type I phase matching produces the output that has orthogonal polarisation with respect to the input beam.

allowed fine adjustment of the position) and placed near to the foci of the beams. For solid state experiments, the cell was replaced by a cryostat. The microtomed samples were mounted on a fused silica disc (thickness = 1 mm) and secured in the sample holder of the cryostat (see Fig 3.8). The cryostat was used either to run experiments at cryogenic temperatures (77 K) or it served as a 'chamber' in which sensitive samples were kept and dry nitrogen gas was filled in to keep them from oxidising.

The beams for the experiment were spatially overlapped with one another and their sizes at the sample position were determined, e.g. for setting the fluence in the experiment, by placing a set of apertures of known sizes and measuring the transmitted intensity (or power) using a power meter. The FWHM beam sizes (in µm) were calculated using the following formulae

$$w = \sqrt{\frac{2r^2}{\ln\left(\frac{1}{1-T}\right)}} \tag{3.7}$$

and

$$\text{spot size (FWHM)} = \left[w \times \sqrt{2\ln 2}\right] \times 10^6 \tag{3.8}$$

where r is the radius of the pinhole in µm and T is the transmission through the pinhole ($T = \frac{I}{I_0}$ where I_0 and I are the intensities of the unattenuated beam and after passing through the pinhole, respectively). The spot sizes at the sample were measured to be 140 µm (pump), 70 µm (probe) and 170 µm (NOPA). The pump and the NOPA beams were blocked after passing through the sample, while the transmitted probe beam was collected and directed towards a home-built Czerny-Turner spectrograph for detection. The probe entered the spectrograph through a slit (60 µm) and was collimated by a concave mirror (focal length = 150 mm), diffracted by a grating (300 lines/mm) and then focused onto a low-noise, front-illuminated linear CCD array (1 × 2048 pixels) capable of shot-to-shot detection rates of up to 2 kHz.

The data acquisition (DAQ) was controlled with a software developed by Dr

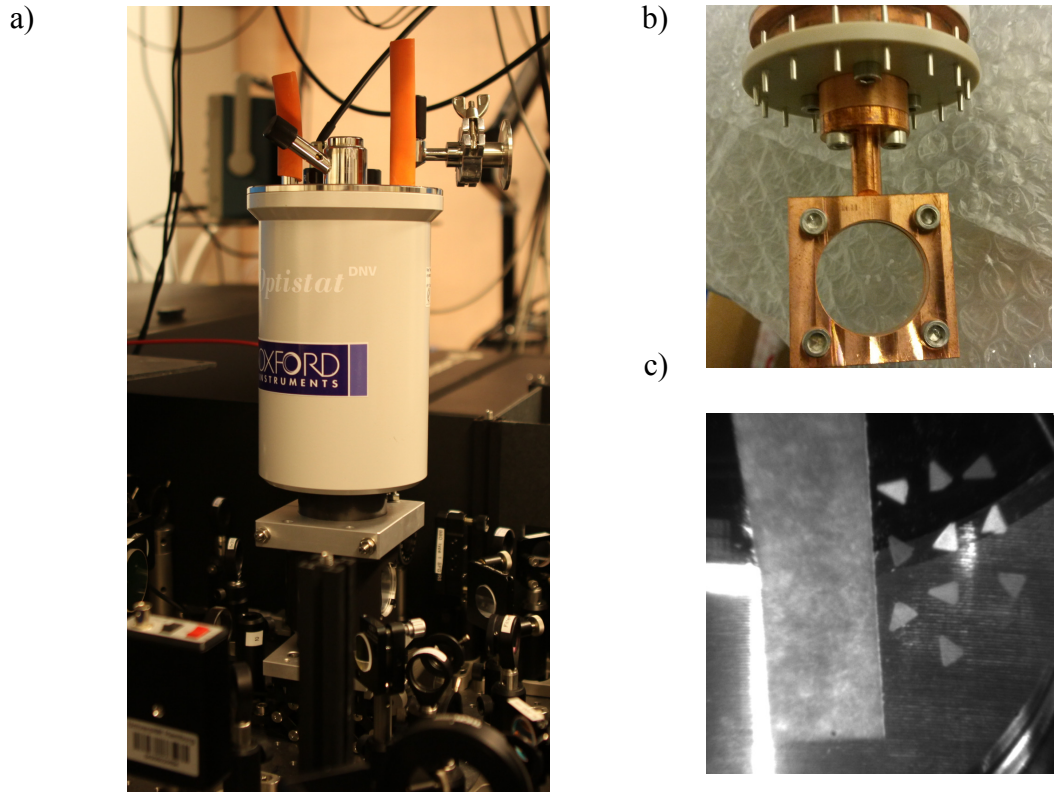

Figure 3.8: a) The cryostat used the in the solid-state experiments b) The sample holder for fused silica discs c) A photograph showing the microtomed samples mounted on the fused silica disc.

Corthey and written in C# language. A Bayonet Neill-Concelman (BNC) cable took a transistor-transistor logic (TTL) signal (1 kHz) from the laser as an input (trigger) for the chopper controller (CC1). The CC1 was configured to reduce the input frequency to exactly half. The output signal from CC1 was sent to the chopping unit (consisting of a spinning motor to which the blade was mounted) using an Ethernet cable. It also triggered the controller of a second chopping unit (CC2), set up to change the repetition rate once again to 1/2 of the input frequency. By adjusting the settings on the two controllers, the chopping units were made to phase lock with one another and with the original laser frequency, so that the main beam passed through the spinning blades without any clipping. By using different chopping blades and settings of the controllers, different chopping schemes could be realised. For example, when the main beam was required to

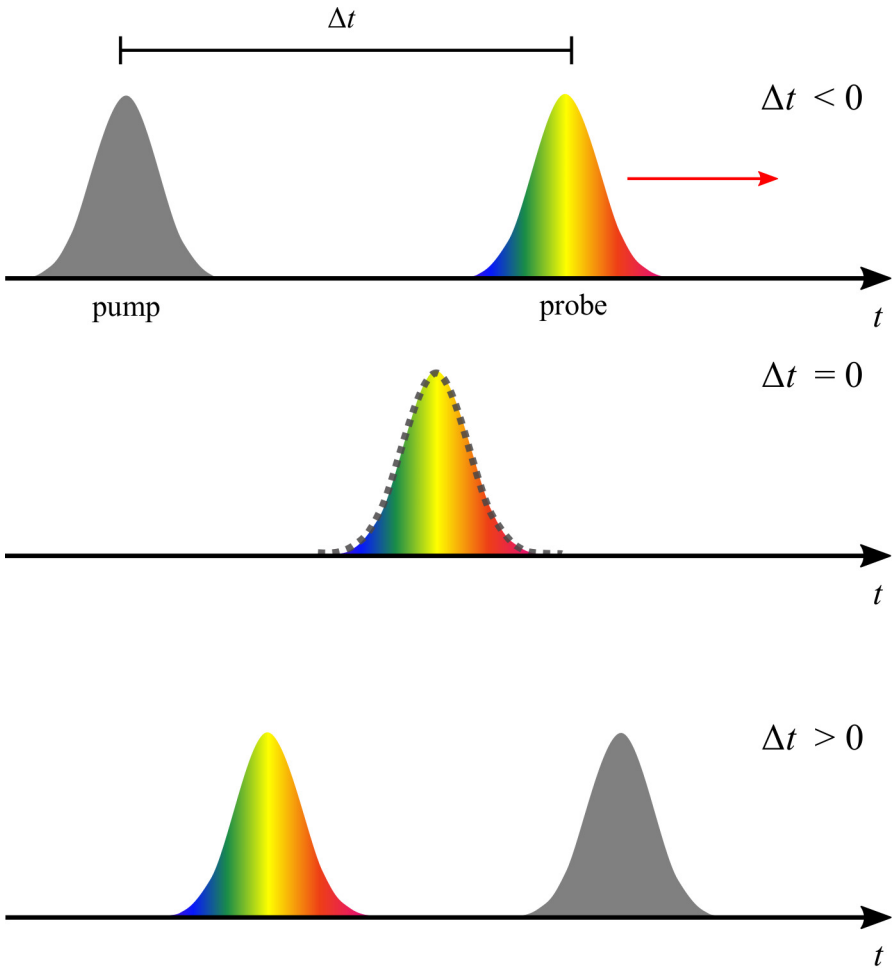

Figure 3.9: The graphical description of different time delays in the pump-probe experiment. The red arrow points to the direction of propagation. At $t = 0$, the temporal overlap between the pump and probe is established with the pump interacting first with the shorter wavelengths of the probe beam.

have a repetition frequency of 1 kHz, both chopping units were turned off or when 500 Hz was desired, one chopper was run while the other stayed off. Inside the TA setup, a beam splitter (BS3) in the probe arm reflected a small fraction (1 %) of the beam into a photodetector (PD1), which generated a voltage signal that was used to synchronise the chopper in the pump line using the controller CC3, but also provided the trigger for the multi-channel digital delay generator (DDG). A custom two-slot chopping blade was employed that reduced the pump beam frequency to 1/8th of the probe repetition rate. The DDG was used to manage

the triggering, delaying and synchronisation events in the experiment. An output of the DDG was used to trigger the DAQ card and a separate output was used to trigger the CCD camera. The software controlled all aspects relating to the experiment including the hardware, e.g. delay line, CCD and also displayed the data (as ΔOD) during experiments and stored it in a readable format in the computer for later processing.

3.3.1 Data acquisition

The pump and probe experiment begins with the probe beam arriving at the sample position before the pump beam (required to get a baseline) and for these time points, referred to as negative time delays, no photoinduced signal is expected. As the delay line is translated, the probe beam is increasingly delayed with respect to the pump and after some travel of the DL, the pump overtakes the probe and a signal begins to be observed. The moment when the pump and probe beams are exactly overlapped in time is referred to as the time-zero (or $t = 0$ and 't-naught') and represents the onset of a photoinduced process. At positive delays, the response of the system after excitation can be measured. Different stages of the acquisition are depicted in Fig 3.9.

3.3.2 Calibration of the spectrometer

The CCD detector is a linear array made up of elements called pixels. Each pixel in the CCD needs to be assigned to a wavelength in order to extract meaningful information from the transmitted spectrum, i.e. it needs to be calibrated. Wavelength calibration is always required when the spectrometers grating orientation is changed, e.g. to change the wavelength range detected by the CCD or if any optical element is removed and replaced from the spectrograph. A standard lamp with a known spectrum can be used for this purpose and colour filters, that have a sharp cut-off at certain wavelengths, can be used to check the goodness of calibration. For our purpose, we used a mercury-argon lamp as the calibration source, which emits radiations in the range 253.6-922.5 nm. The light from the

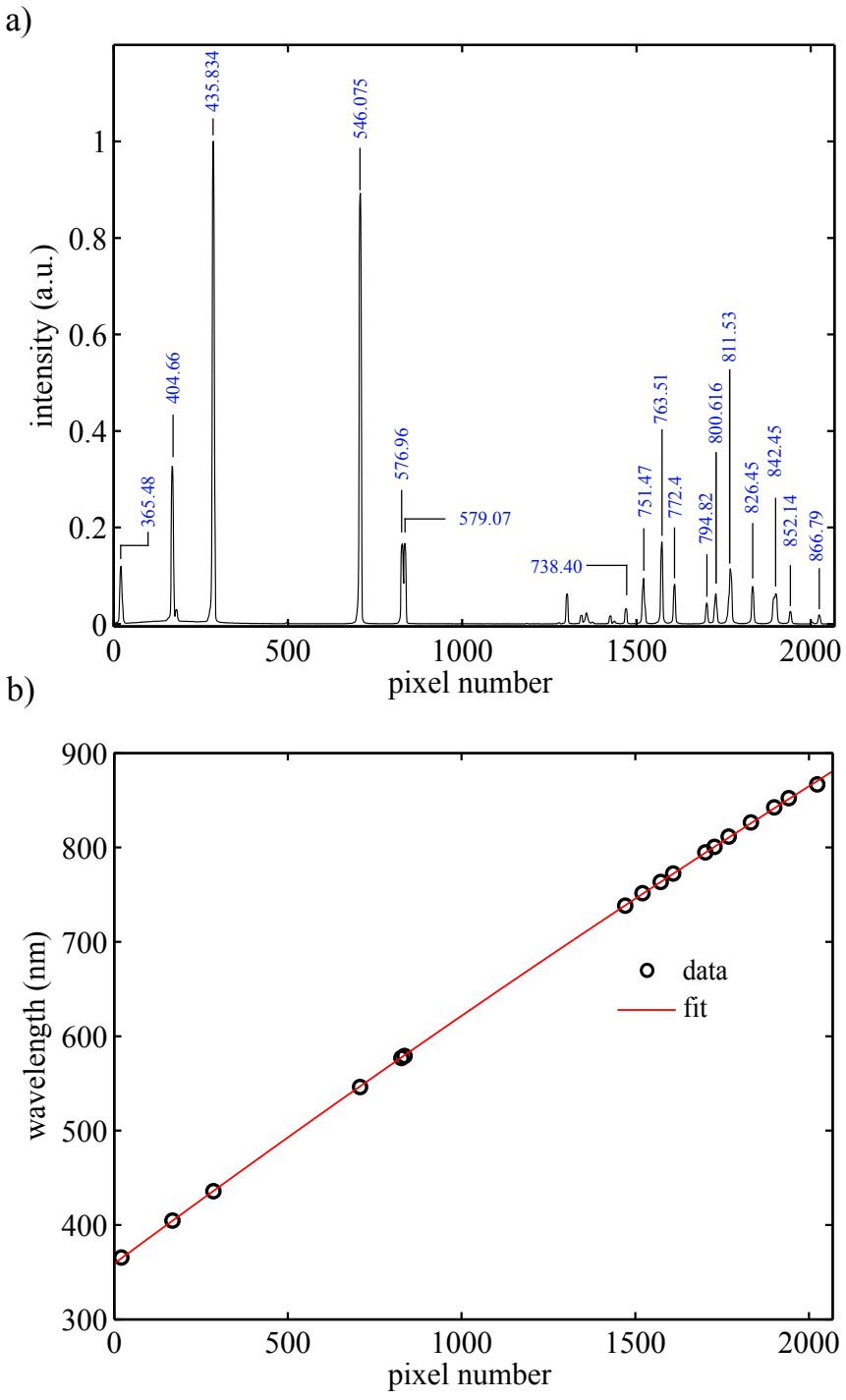

Figure 3.10: a) Measured spectrum of the calibration source. The peaks are assigned to wavelengths (printed in blue), identified with the help of the spectrum of calibration source b) Plot of wavelength vs pixel number and the fit.

lamp was diffracted by the grating in the spectrograph and imaged onto the CCD. The measured spectrum (intensity vs pixels) shows peaks which can be identified by comparing them to spectrum of the calibration source. After peaks had been assigned, a plot of the wavelengths against the corresponding pixel number was created and fitted with a polynomial function. The function used to fit the calibration trace was

$$\lambda_{\text{calibrated}} = -9.6 \times 10^{-6}\text{pix}^2 + 0.277\text{pix} + 359 \tag{3.9}$$

where the variable, pix is the number of the pixel element of the CCD array. The fit function was saved in the acquisition software to correctly display the spectrum in terms of wavelength. Fig 3.10 shows the measured spectrum of the source and the fit.

3.4 Artifacts in TA spectroscopy

As ultrashort lasers feature heavily in transient absorption studies, the time-resolved spectrum often contains two types of signals: from the sample itself and from the solvent and/or cuvette/substrate. The latter can be a nuisance, especially as the very fast dynamics of the sample (10-100 fs) can obscured by them. Fortunately, some of these can be used for characterisation purposes, thus turning them to the experimentalists advantage. The following sections discuss two kinds of artifacts and how to use or counter them.

3.4.1 Cross-phase modulation

The first one is the so-called cross-phase modulation (XPM), which refers to the time-dependent modulation of the refractive index of a medium by an intense laser beam, the effect of which is 'felt' by another pulse that is spatially and temporally overlapped with the intense beam [98]. This occurs without any net energy transfer to or from the sample. In our experiments, the pump beam is of sufficient intensity that it can modulate the refractive index of a transparent

material and if the probe beam is spectrally and temporally overlapped with the pump, it will experience a change in its phase, which can be mapped if the probe beam is spectrally dispersed. Since the process occurs when the pump and probe beam are temporally overlapped, a strong signal is seen at around the time-zero. This was used to characterise the setup, by performing a cross-correlation measurement in which the pump and probe beams were overlapped in a 1 mm thick fused silica disc or a quartz cuvette filled with either ethanol or hexane.

3.4.2 Chirp correction

The concept of chirp was introduced in chapter 2. A chirped broadband probe (390-900 nm) is used in the experiments and thus, the temporal overlap of the pump beam with different wavelength components of the probe is different, i.e. the time-zero is wavelength dependent. This is manifest in the 2D transient absorption spectrum as a strong curvature along the time axis and must be corrected before any kinetic information is extracted from the 2D spectrum, e.g. by global analysis methods. Fig 3.11 shows the cross-correlation measurement of the pump (266 nm, 2.8 mJ cm^{-2}) with the chirped probe.

Panel (a) of the figure shows the 2D TA spectrum from this measurement and panel (b) shows the kinetic traces taken at selected wavelengths. As can be seen from the figure, there is a clear timing offset in the peak positions of the different wavelength components due to the chirp. Notice also that the signals from shorter wavelengths appear before the longer wavelengths. This can be explained by recalling that under normally dispersive conditions, the photons of longer wavelengths travel faster in a medium than the ones with shorter wavelengths. As the experiment begins with the probe beam arriving at the sample position ahead of the pump, i.e. $\Delta t < 0$ (see Fig 3.9) and as the shorter wavelength photons in the probe beam form the trailing edge, they interact with the pump beam before the longer wavelength photons as the delay between the two beams is minimised and time-zero is reached and thus, the response is registered first in the bluer region of the transient absorption spectrum.

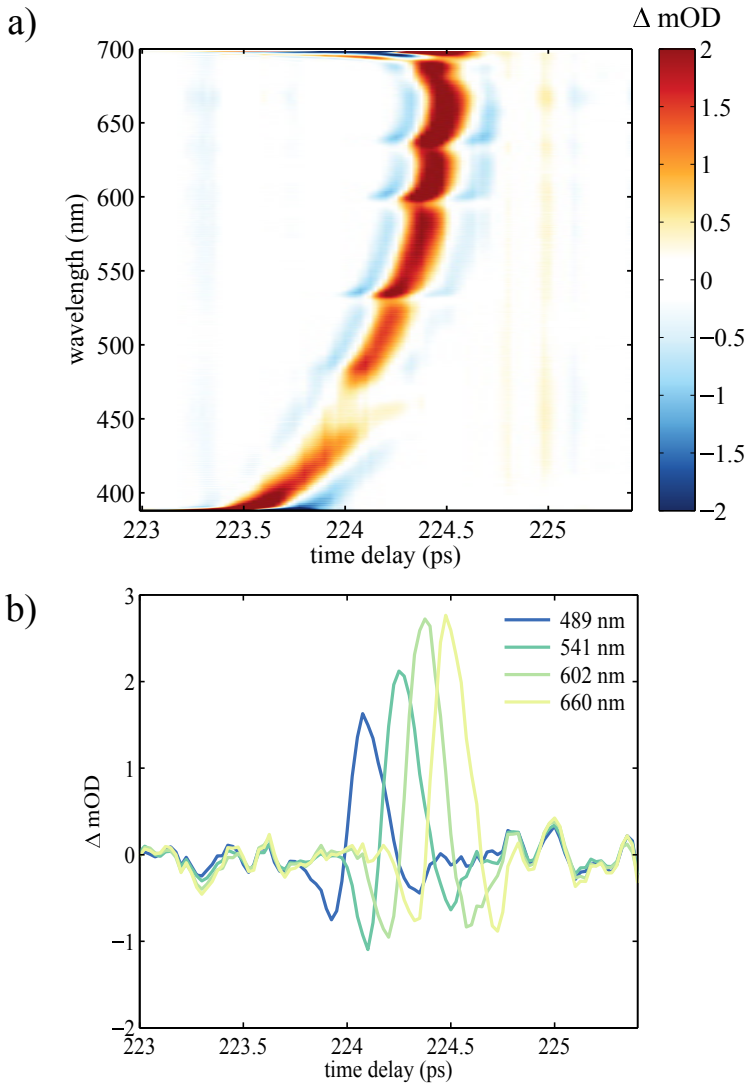

Figure 3.11: a) 2D TA spectrum from cross-correlation measurement in 1 mm thick fused silica b) Kinetic traces at selected wavelengths showing temporal offset due to the probe chirp.

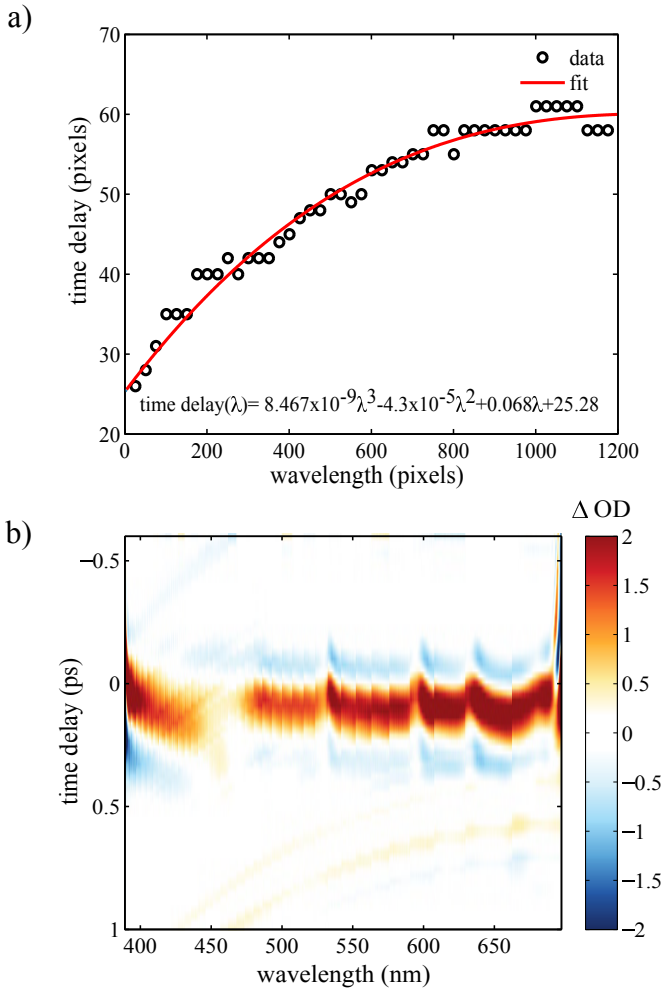

Figure 3.12: a). Plot of time delays against wavelengths (in pixels) from the cross-correlation measurements and the fitting b) 2D spectrum after applying the chirp correction.

In order to correct the chirp, the peak positions (in time) of several different wavelength components must be precisely determined (by fitting the peaks with a Gaussian or some other appropriate function) and plotted against the corresponding wavelengths to give a curve that can be fitted with a polynomial function of the appropriate order [4] and used in subtraction to correct for the chirp as shown in Fig 3.12. Finally, notice that the 2D map shows features that look like sharp bands (for example, look across 600 nm). This structure is very unusual and the origin of this is yet unknown, but most likely is a result of some imperfections of the optics, for example, surface coating; it is not due to any nonlinear response of the medium. This was confirmed by performing the cross-correlation measurements separately using water and sapphire, which had little effect on the appearance (or location) of the bands.

3.4.3 Temporal resolution

The temporal resolution (also called the instrument response function, IRF) of the pump-probe setup can also be determined by using the cross-correlation measurement. Fig 3.13 shows a trace along a selected wavelength and fit. A second-order derivative of a Gaussian was used to fit the trace and the full width at half maximum was approximated as the time resolution of the instrument [99]. The (average) time resolution, estimated from the fitting several kinetic traces, was 230 fs.

[4] A third-order polynomial was used to fit the data. The equation is given in Fig 3.12

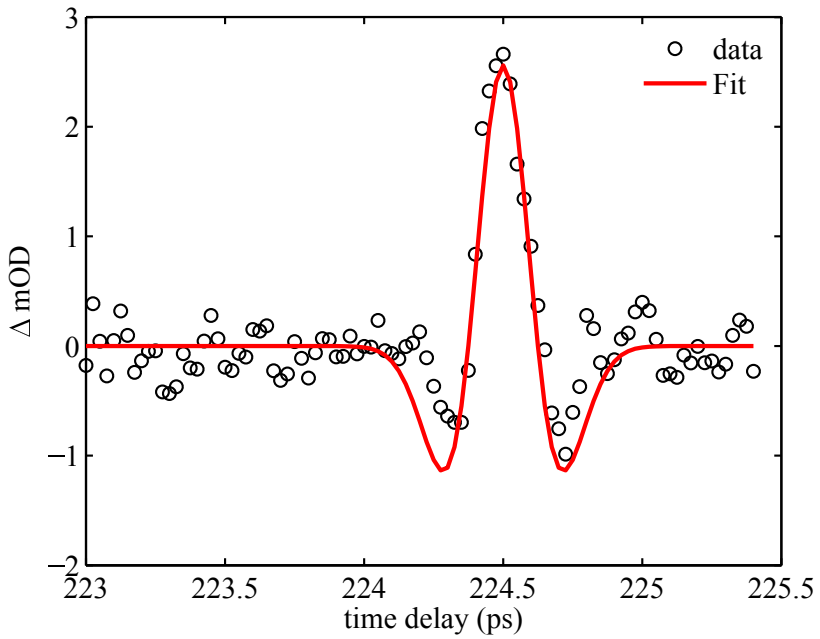

Figure 3.13: Result of cross-correlation of the 266 nm pump and white light probe. The trace was fitted with a second derivative of a Gaussian.

Chapter 4

Synchronised Photoreversion of Crystalline Spirooxazines

The work reported here is motivated by the aim to perform femtosecond electron diffraction studies on molecular systems in order to investigate the mechanisms of photochemical processes, such as bond dissociation, isomerisation and pericyclic rearrangements, in the solid state. This chapter present a method that has been developed to achieve this goal. The chapter is structured as follow. First, the system selected for a proof-of-principle demonstration will be introduced and its photochemistry will be reviewed briefly. This will be followed by a section that describes the method of synchronised photoreversion. Following that, the results of the experiments will be presented and discussed before concluding the chapter with some remarks.

4.1 Introduction to Spirooxazines

Spirooxazines (SOs) belong to a family of compounds that have the ability to change conformation after absorbing a quantum of light and are able to configure back to the original form through absorption of a photon of different wavelength. Such light-responsive compounds are called photochromic systems [100]. They typically possess two distinct absorption bands, characterising the

two different conformations. Spiropyrans [101], spirooxazines [102], diarylethenes [103], azobenzenes [104], fulgides [105] and their derivatives are all examples of such systems. Accompanying the reversible photochemical change, is alteration of, amongst others, fluorescence/absorption, magnetic properties, refractive index, dielectric constants and coordination [106]. As a result, these photochromic systems have attracted huge interest for various potential applications, such as memory storage devices [107], logic gates [108] and photoswitches [109]. The applicability of photochromic systems, such as the SOs, to these devices will depend on the switching time scales and the respective quantum yields as well as on the photofatigue resistance, that is to say the number of photochemical cycles that they can perform before significant degradation of their photoactivity occurs.

Spiropyrans and spirooxazines have been known to undergo photochromic reactions with ultrafast timescales which makes them suitable candidates for some of the applications mentioned above. Spirooxazines are considered to be more promising, however, because of their superior fatigue resistance as compared to spiropyrans [110]; they were shown to undergo tens to hundreds of photochromic cycles without any loss of photochemical activity [111]. This high photofatigue resistance has been attributed to the stabilisation provided by the nitrogen atom of the oxazine ring [112].

Of many SOs, Spironaphthooxazines (SNO) have been a subject of intense investigation by many groups over the last two decades or so. SNO consists of two heterocyclic, nearly planar rings (indoline and oxazine) linked by an sp^3 hybridised spiro carbon. Due to the orthogonal relationship (see the stereochemistry of SNO in Fig 4.1) between the indoline and oxazine rings, the overlap of the orbitals in the two moieties is poor, therefore the gap between the highest occupied molecular orbital (HOMO) and the lowest unoccupied molecular orbital (LUMO) is large (on the order of 3-4 eV) [113]. Consequently, a solution of SNO shows strong absorption in the UV and appears colourless. Conjugation is achieved through a structural change —that involves an almost 90° degrees rotation of the oxazine unit relative to its position in the SNO, after absorption of a

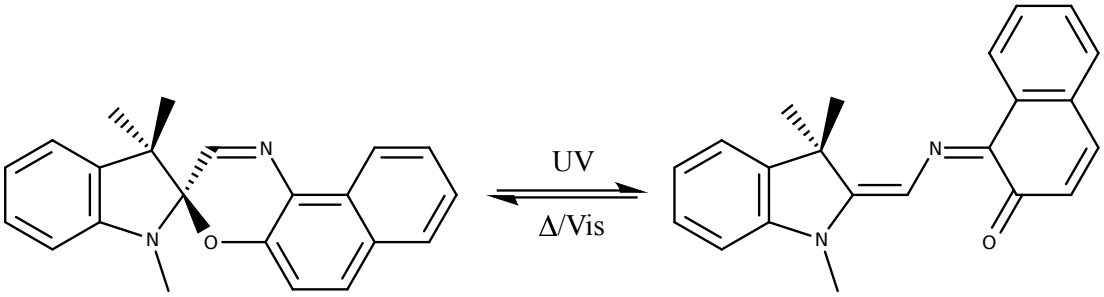

Spironaphthooxazine (SNO) Merocyanine (MC)

Figure 4.1: Photochromic reaction of spironaphthooxazine (SNO) to give merocyanine (MC).

UV photon which alters the HOMO-LUMO gap (makes it smaller) and intense absorption in the visible region of the electromagnetic spectrum occurs. The resulting planar structure is known as merocyanine (MC). The MC can return to the SNO form either thermally or photochemically. The reaction scheme of SNO is shown Fig 4.1. An extensive body of theoretical [114–116] and experimental work already exists on the photodynamics of SNO in solution [117, 118], polymer matrices [119], including some studies performed in the gas phase [120] and one ultrafast study in the solid state [121]. A general picture of the mechanism of photochromism in SNO that has emerged from time-resolved solution phase experiments is that, upon absorption of a UV photon, a rapid breaking of the bond between the spiro-carbon (the one that joins the two rings) and the oxygen in the oxazine ring takes place and leads to ring-opening and isomerisation to a trans-merocyanine product. It has been shown that the photochromic reaction of unsubstituted SNO occurs solely on singlet state surfaces, on account of very fast rates measured for the ring-opening reaction and the lack of oxygen effects observed on the formation and the decay rates of merocyanine [122].

Tamai and co-workers were one of the first to perform time-resolved absorption experiments on SNO using femtosecond lasers. They conducted their experiments in 1-butanol using a 355 nm laser light for excitation [123]. In their measurements, a peak at 490 nm appeared after excitation and decayed over time to be replaced

by a broad absorption band in the 550-700 nm region, with a maximum at 580 nm. This followed a shift of the band to shorter wavelengths in 2 ps. After 100 ps, a peak with a maximum at 610 nm and a shoulder at 575 nm remained. The authors assigned the 490 nm absorption to $S_1 \rightarrow S_n$ transition. They reported a short lifetime of 700 fs for the peak at 460 nm and attributed it to the relaxation of the S_1 state of spiro form. Furthermore, the broad absorption was assigned to a ring-opened nonplanar intermediate, X following the cleavage of the C-O bond and the 610 nm absorption was ascribed to the relaxed form of the merocyanine.

Antipin *et al* reported similar findings as Tamai and co-worker after conducting their own transient absorption study on SNO, but chose 305 nm wavelength for excitation [124]. They observed a signal at 490 nm emerging within 0.25 ps, which they assigned to the absorption from the singlet excited state to higher lying states. After 1 ps, the absorption decreased and a shift to the blue region (460 nm) was observed, followed by a decay of the short-wavelength band and a simultaneous increase of absorption at longer wavelengths. They modelled their results based on a potential energy scheme in which the S_1 surface has two minima, where one of the minima corresponds to the equilibrium configuration of the initial SNO form, i.e. with the C-O bond intact and the other, with slightly lower energy, to the ring-opened species with parent geometry (intermediate X) and this minimum lay directly above the barrier that separated SNO from the MC in the ground state. They proposed that excitation from 305 nm (which populates the S_2 state of the SNO) results in a rapid internal conversion to excited vibrational states of the S_1 state, followed by relaxation to the potential well of the S_1, causing the formation of the intermediate X and the 460 nm absorption was attributed to be from this structure. As time evolves, the intermediate X is converted to merocyanine isomers, following a non-adiabatic transition to the ground state surface (facilitated by a rotation of the bonds during isomerisation). The resulting isomers absorb in the redder regions of the spectrum. The simultaneous drop of intermediate X and rise of merocyanine absorption appeared as an isosbestic point (a point at which spectra momentarily merge) in their tran-

sient spectra, leading them to hypothesise that intermediate X leads directly to merocyanine products.

However, the notion that intermediate X could be the precursor to the MC product was challenged by Buntinx *et al* [125], who performed experiments on solutions of unsubstituted and substituted spirooxazines, prepared in different solvents, to study the effect that it may have on the reaction dynamics and to clarify the role of the intermediate X in the ring-opening reaction. They carried out the experiments with 377 nm and 252 nm femtosecond lasers as the pump source and used a supercontinuum generated from calcium fluoride (CaF_2) to monitor the changes in absorption after excitation. In the case of unsubstituted SNO, they observed an instrument-response limited rise of a band lying in the 400-550 nm region (referred to as the blue band in their paper) with, $\tau_{\mathrm{SNOrise}} = 0.17\,\mathrm{ps}$ that decayed as time evolved. Moreover, they observed that another band at 550-650 nm, corresponding to the open merocynanine form, rose with a time constant of $\tau_{\mathrm{MCrise}} = 0.75\,\mathrm{ps}$ after excitation. The peak of this band shifted towards longer wavelengths when the experiments were conducted with substituted SNOs. The same trend was observed when they used more polar solvents in the experiment. In addition to the two bands, they located another band above 700 nm in the near-IR region. The kinetics of this band showed similar trends as the 400-500 nm band, leading the authors to ascribe it to the same transient species.

In their measurements using different solvents, the authors observed that the decay of the blue band did not always coincide with the rise of the visible band. This was especially apparent for acetronitile, where the MC band had formed well before the complete decay of the blue band. Moreover, the quantum yields for SNO $\rightarrow$ MC reaction showed a trend towards higher MC yields with nonpolar solvents than with polar solvents. Based on these observations, the authors concluded that the previously believed X intermediate could not be the precursor of the ring opened merocynanine. Furthermore, they hypothesised that the competition between processes (barrier crossing to potential minimum of SNO or MC) should determine the fate of the reaction, i.e. whether it will lead to formation

of MC or not. They theorised that vibrationally hot molecules would be able to overcome the barrier to form the MC, while those whose energies are stabilised, for instance by interaction with polar solvents, would return to the SNO form. The underlying assumption in this rationale was that the barrier height of X→ MC form is much higher than for X→ SNO. The authors backed up their claims by referring to the calculations of potential energy surfaces by Maurel *et al*, who used a combination of time-dependent density functional theory (TD-DFT), complete-active space self-consistent field (CASSCF) and semi-empirical methods for PES construction. They found that the X→ MC barrier was indeed much larger, by an order of magnitude, than the X→ SNO [126].

Suzuki *et al* were the first to investigate the photochromic behaviour of crystalline spirooxazine using ultrafast pump-probe spectroscopy [127]. They grew microcrystals of the unsubstituted SNO, crushed and placed them inside a 1 mm path length cuvette. They developed a diffuse reflectance spectroscopy apparatus (with instrument response on the order of a picosecond) to study the dynamics induced by a femtosecond laser pulse on SNO crystals [128]. The excitation light in their setup was the second harmonic of the fundamental of Ti:Sa amplifier, i.e. 390 nm, operating at 10 Hz and a supercontinuum (produced from a water jet) was used as the probe beam. They measured the reflectance changes of the sample upon excitation and related them to % absorption. Two different fluence regimes were explored by the authors: low fluence ($< 1\,\mathrm{mJ\ cm^{-2}}$) and high fluence regime ($> 1\,\mathrm{mJ\ cm^{-2}}$). In order to avoid measuring signals from damaged areas of the sample, they moved the probe spot to a new region after every 50 shots of the pump.

Under low excitation conditions (fluence of $<0.5\ \mathrm{mJ\ cm^{-2}}$), they observed a transient absorption feature which appeared immediately after excitation and peaked at 500 nm and accompanying it was a broad absorption band extending from 600 to 800 nm. They ascribed the 500 nm peak to the absorption of excited singlet state to higher lying excited states, i.e. $S_1 \rightarrow S_n$. The absorption signal decayed in about 3 ps. They reasoned that the long lifetime of this state, when

compared to that in the solution (0.7 ps), was likely due to strong restriction to structural changes of molecules embedded in a crystalline lattice. Even after the S_1 absorption band had decayed, peaks at 460 and 740 nm remained and these were assigned to be from the nonplanar, open form of the SNO. The lifetime of these bands was found to be 2 ns. No detectable absorption from the merocyanine product was observed by the authors, even after irradiating the sample with several thousand pump shots. They theorised that the constraints imposed by the compact lattice environment would make the merocynanine production very unlikely.

On the other hand, under high fluence conditions, clear absorption from merocyanine was observed. The authors carried out experiments with varying excitation densities and noticed that the MC absorption increased nonlinearly with increasing pump powers. Moreover, at higher fluences, the spectral profile of the MC band was sharper and narrower than when the fluence was lower, leading them to propose that at lower excitations (above the merocynanoine production threshold), a number of isomers contribute to the spectral profile, while at higher fluences, only the trans-merocynanine, similar to that formed in solution phase, is predominately generated. For the cases when the fluence was below $4\,\mathrm{mJ\ cm^{-2}}$, multi-shot experiments were necessary to see the change. The authors speculated that every pump pulse produces defects in the crystal (which accumulate over time), until it becomes possible to trigger the production of trans-planar merocynanine. This formed the basis of a cooperative model that they proposed, wherein excitation with an intense femtosecond laser pulse induces bond breaking and ring-opening at multiple sites within the crystalline lattice, resulting in local disorder, which ultimately creates free volume around the molecule, making it possible for the excited species to undergo large structural changes to give trans-planar PMC [129].

4.2 Experimental section

4.2.1 Sample preparation

SNO [1] was purchased from Sigma-Aldrich (product # 322547) and used without further purification. Crystals of SNO were grown by dissolving approximately 10 mg of powdered SNO ($M_r = 328.41\,g\,mol^{-1}$) in either high purity ethanol or methanol or a mixture of the two, under mild heating (40° C) and slowly evaporating the super-saturated solution in darkness[2]. Attempts to crystallise SNO by dissolving the powder in nonpolar solvents, such as hexane, proved futile. The bulk crystals had either bi-pyramidal or plate like morphology. Most crystals showed a change of colour (colourless to brown) after being stored under atmospheric conditions for a few days. The colour change was most likely the result of oxidation, so it was decided to keep the crystals in a vessel filled with dry nitrogen. Crystals of the highest quality (inspected with an optical microscope) were selected for experiments and sliced along one of the faces using ultramicrotomy. The sections were mounted on a fused silica disc (1 mm thick). A sample thickness of 500 nm was chosen for the transient absorption experiments. To check whether the microtomed sections were (single or poly) crystalline, static electron diffraction patterns were obtained using our home-built femtosecond electron diffraction apparatus (see chapter 5). For this measurement, the thickness of the sections was 100 nm (to ensure transmission of electrons) and the crystal films were mounted on a copper TEM mesh, with 1000 square grids per inch. The electron diffraction pattern showed discrete spots (see next chapter), revealing that the thin sample was single crystalline.

[1] 1,3-Dihydro-1,3,3-trimethylspiro[2H-indole-2,3-[3H]-napth[2,1-b][1,4] oxazine].

[2] Dr Rossos and I worked on the SNO sample preparation and microtomy with help from Drs Hayes and Murphy

4.2.1.1 Crystal structure

The crystal structure of SNO is available in literature and has been determined by Harada and co-workers using x-ray diffraction methods [130]. The SNO crystal belongs to the orthorhombic crystal system with unit cell lengths: **a** = 17.16 Å, **b** = 16.83 Å and **c** = 12.41 Å. Each unit cell contains a total of eight molecules as shown in Fig 4.2.

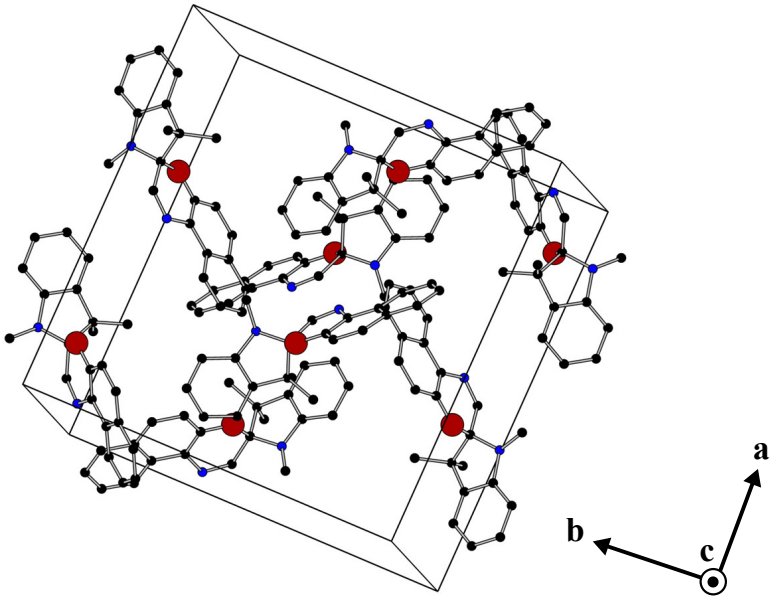

Figure 4.2: A view of the unit cell of SNO represented in balls and sticks. Carbon atoms are depicted by black balls, nitrogen with blue and oxygen with red balls. Hydrogens are omitted from the figure for clarity. There are a total of eight molecules in the unit cell.

4.2.2 Synchronised photoreversion

The importance of reversibility was discussed in the previous chapter. It was emphasised that in a pump-probe experiment, the molecules under investigation must return to their original form, to allow every pump pulse to induce the same photoreaction and to prevent measuring erroneous signals. A short review of some approaches that have been used in the past to tackle this issue was briefly provided. It was hinted that the approach implemented by Jean-Ruel *et al* [97]

to study diarytethenes was a particularly promising one, especially for ultrafast studies of photoreversible solid state reactions, with multiple laser shots. The approach implemented in this chapter is an extension of their work and is described below [131].

The idea is a simple one: trigger and probe the reaction of interest, but before the next pumping cycle, stimulate the products back to the original configuration, thereby preventing photoproducts from remaining in the probe region. As can be imagined, this requires an additional laser beam to perform the back pumping and that it must be done in a synchronous fashion. The inclusion of an additional beam makes this a three-beam approach. Three-beam experiments are not uncommon in ultrafast spectroscopy. In fact, a few schemes that exploit three laser beams in TA setups have been developed for different purposes over the years, such as the pump-repump-probe [132] and pump-dump-probe [133] schemes to name a couple. The scheme implemented here can be referred to as a "pump-probe-recover" scheme. The choice of the third beam (henceforth called the photoreversion beam), i.e. what photon energy to use, will depend on the system under investigation, but should have a wavelength that corresponds to the maximum of product absorption. In addition, it must come from an ultrashort laser source, ideally from the same laser from which the pump and probe beams are derived, as precise synchronisation is then automatically ensured. The reason for using ultrafast laser pulses as opposed to CW beams (or for that matter, a nanosecond pulsed laser) is that they offer much higher beam flux, making them much more effective for photoreversion, but also because ultrashort duration of the pulses allows the photoreversion process to be driven faster than the deformation of the crystal (due to the propagation of strain), the timescale of which can be on the order of a few hundred picoseconds to nanoseconds [134]. This approach, therefore, relies on "recovery before destruction" idea.

4.2.3 Acquisition scheme

In order to implement the approach described above and to actively monitor the state of the sample (whether it is damaged or not), a scheme for the acquisition of the data, different from a more conventional (pumpON-PumpOFF) one, was developed. The pump laser was chosen to run at a repetition rate of 31.25 Hz. As was alluded to in chapter 1, repetition rates lower than 100 Hz are typically required to keep the sample from getting thermally damaged. The choice of 31.25 Hz was made as it was found to be a good compromise between fast acquisition and minimum sample damage and also because the appropriate set of chopper blades happened to be available during the time the experiments were performed. The probe, on the other hand, was made to run at 250 Hz and additionally, the photoreversion beam (derived from the NOPA) was used in the experiments, operating at 1 kHz as shown in Fig 4.3.

A pump and probe cycle comprised of a single pump pulse impinging on the sample to initiate the dynamics and eight probe pulses hitting the sample, a set time delay later. The very first probe pulse, i.e. the one which monitors the transient absorption change in the sample, was labelled as 0 and the subsequent pulses, with increasing delay in ms range, were labelled from 1 to 7. As the repetition rate was 250 Hz, the probe pulses were separated by 4 ms $\left(\frac{1}{250\text{ Hz}} = 0.004\text{ s}\right)$. The spectra of all the probe pulses were recorded. This permitted us to follow how the sample was recovering (after the removal of the excitation pulse) in milliseconds intervals. The delay line used in the experiments had a travel range that provided a coverage of 1.5 ns, so in order to ensure that the photoreversion pulses did not interfere with any pump-probe sequence in the time-resolved scan, the optical path length of the NOPA beam was set so that it always arrived at least 10 ns after the first probe pulse (with label 0). The NOPA beam was chosen to run at a much higher repetition rate than the probe or pump to have maximum chance of converting molecules back to their initial state. Thus, immediately after the pulse 0, 32 NOPA pulses (4 between each probe pulse) separated by 1 ms, hit the sample. Two sets of spectra were measured: one relating to the transient

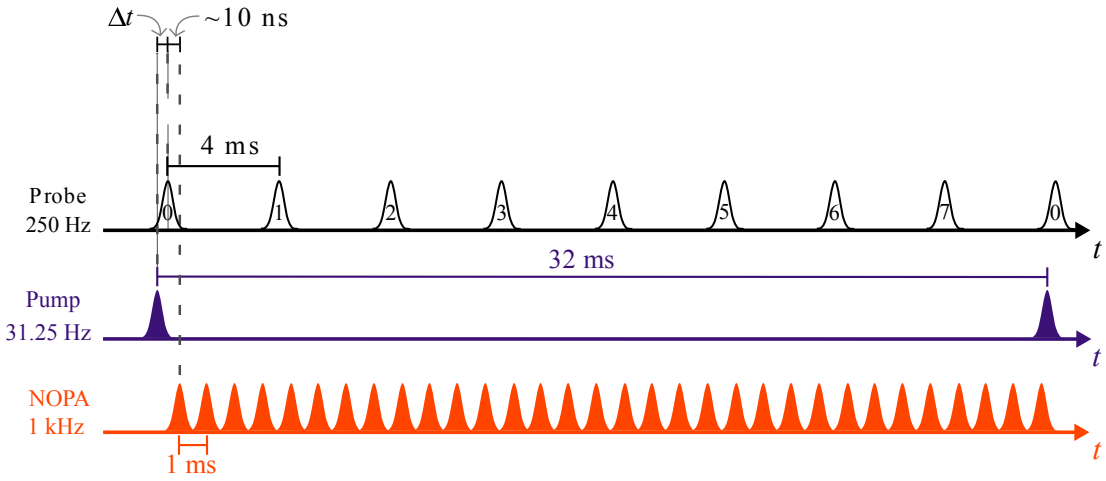

Figure 4.3: The synchronisation scheme used in the experiments involving crystals.

absorption, $\Delta\mathrm{OD}_{\mathrm{TR}}$, recorded after the excitation event and other being the *buildup* spectra, $\Delta\mathrm{OD}_{\mathrm{M}}$ corresponding to the steady-state absorption measured at $\Delta t + 4n$ ms after excitation, where n is the probe pulse number and $n > 0$. The $\Delta\mathrm{OD}_{\mathrm{TR}}$ was calculated as

$$\Delta\mathrm{OD}_{\mathrm{TR}}(\lambda, \Delta t) = \log\left(\frac{I_7(\lambda, \Delta t)}{I_0(\lambda, \Delta t)}\right) \tag{4.1}$$

where λ is the wavelength of the probe, Δt is the time delay of the probe with respect to the pump, $I_0(\lambda, \Delta t)$ is the transmitted intensity of the pulse 0, measured a time delay, Δt after the pump pulse and corrected for background, $I_7(\lambda, \Delta t)$ is the transmitted intensity of pulse number 7, which is measured 28 ms + Δt after the pump pulse. The buildup spectra, $\Delta\mathrm{OD}_{\mathrm{M}}$, on the other hand, was calculated using

$$\Delta\mathrm{OD}_{\mathrm{M}}(\lambda, s) = \log\left(\frac{I_{\mathrm{ref}}(\lambda)}{I_7(\lambda, s)}\right) \tag{4.2}$$

where $I_{\mathrm{ref}}(\lambda)$ is the transmitted spectrum through the crystal, measured before any excitation and s denotes the number of pump shots. The following must be ensured: the sample must be in the same state at pulse 7 as before starting

the experiment. If this is not the case, then the sample is not reversible and the buildup spectrum will correspond to the species that remain in the probe volume.

4.3 Transient absorption of SNO

Transient absorption experiments were performed in dilute solution of SNO and on the crystalline samples. The apparatus used to carry out the experiments was described in detail in the previous chapter. Solution phase experiments were performed so that the results could be compared with transient absorption experiments performed with crystalline SNO, but also to calibrate the performance of the setup. The sample in this case was prepared by dissolving a measured amount of SNO ($M_r = 328.41\,\mathrm{g\ mol^{-1}}$) in hexane to make up 20×10^{-3} M solution. The data were collected using 266 nm light (produced by third harmonic generation of the fundamental beam, 800 nm as described in the previous chapter), operating at 250 Hz, as the pump and the white light probe repetition rate was set at 500 Hz, i.e. every second pump pulse was blocked. The sample was flowed through a 0.5 mm cuvette at high enough flow rates that it was completely refreshed between pump laser shots. The relative polarisations of the probe and pump beams was set to the magic angle (54.7°). For each time delay, 250 pump-probe spectra were collected and transient absorption spectra were calculated by comparing the pumpON and pumpOFF intensities as

$$\Delta \mathrm{OD}_{\mathrm{TR}}(\lambda, \Delta t) = \log\left(\frac{I_{\mathrm{pumpOFF}}(\lambda, \Delta t)}{I_{\mathrm{pumpON}}(\lambda, \Delta t)}\right) \tag{4.3}$$

4.3.1 Data analysis

The data were analysed by assuming that the kinetics of the system can be described by a sum of exponential decays, convoluted with the instrument response of the setup [92]. Eq 4.4 was used to perform the fitting by taking kinetic traces

at selected wavelengths.

$$f(t) = \left\{ H(t-t_0)) \cdot \left[\sum_{n=1}^{i} A_i \cdot e^{\left(-\frac{t-t_0}{\tau_i} \right)} \right] \right\} \otimes \text{IRF}$$
$$f(t) = 0.5 \cdot \left[\sum_{n=1}^{i} A_i \text{e}^{\left(-\frac{t-t_0}{\tau_i} \right)} \cdot e^{\left(\frac{\sigma^2}{2\tau_i} \right)} \cdot \left[1 + \text{erf}\left(\frac{t-t_0-\sigma^2/\tau_i}{\sqrt{2\sigma}} \right) \right] \right] \tag{4.4}$$

In Eq 4.4, A is the signal amplitude, σ is the width of the IRF (which was modelled with a Gaussian function), t_0 is the time-zero and erf is the error function, resulting from the convolution of the Gaussian with the Heaviside step function, $H\ (t-t_0)$. The fittings were performed in the MATLAB environment using the built-in least-squared curve fitting function (see Appendix). The least-squared method works by minimising the sum of the squares of the residuals resulting from the difference between the data and the model used to fit it.

4.3.2 Steady-State spectra

Fig 4.4 shows the steady-state spectrum of SNO measured in solution. MC was produced after irradiating the SNO solution with the 266 nm laser light and has an intense absorption band in the visible region. The measurements were performed using the microspectrometer (see chapter 3), on 0.5×10^{-3} M solution of SNO in EtOH. The cuvette used had a path length of 1 mm. The optical density at 266 nm is approximately unity and the extinction coefficient, therefore is, $2 \times 10^4\,\text{M}^{-1}\text{cm}^{-1}$. The vertical excitation energies for (isolated) SNO are given in Table 4.1. The excitation energies were calculated by Dr Kochman (see later for the employed computational method).

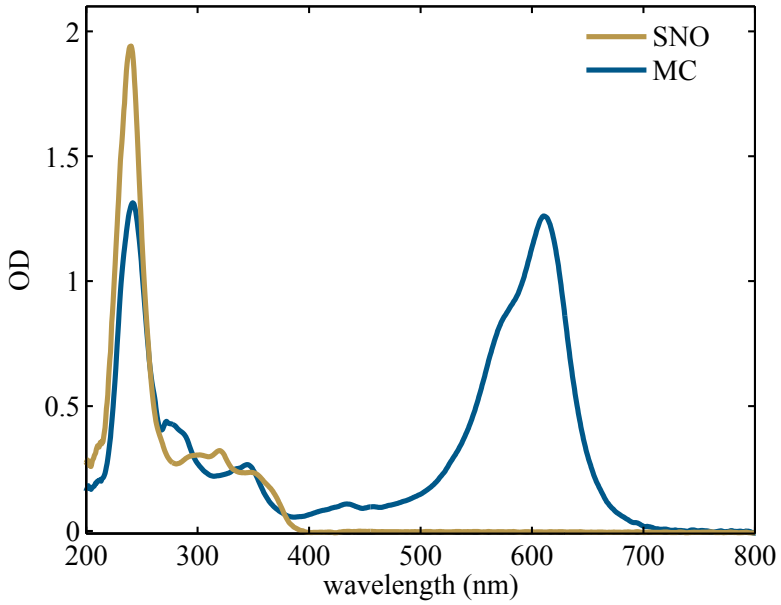

Figure 4.4: Steady-state Spectra of SNO (brown) and MC (blue) measured in EtOH. The MC is produced after 266 nm irradiation.

electronic state	ΔE (eV)	oscillator strength, f
S_1 ($\pi\pi^*$)	3.796	0.077
S_2 ($\pi\pi^*$)	4.093	0.020
S_3 ($\pi\pi^*$)	4.347	0.059
S_4 ($n_N\pi^*$)	4.599	0.004
S_5 ($\pi\pi^*$)	4.717	0.057
S_6 ($\pi\pi^*$)	4.945	0.033

Table 4.1: Vertical excitation energies and corresponding oscillator strengths for some low-lying excited electronic states of SNO. Calculations were performed by Dr Kochman.

4.3.3 Solution phase experiments

4.3.3.1 Results and discussion

The transient absorption spectra ranging from -2.5 to 6 ps, measured with 100 fs time steps and between 15 to 90 ps, measured in 1 ps intervals, are shown in the Fig 4.5.

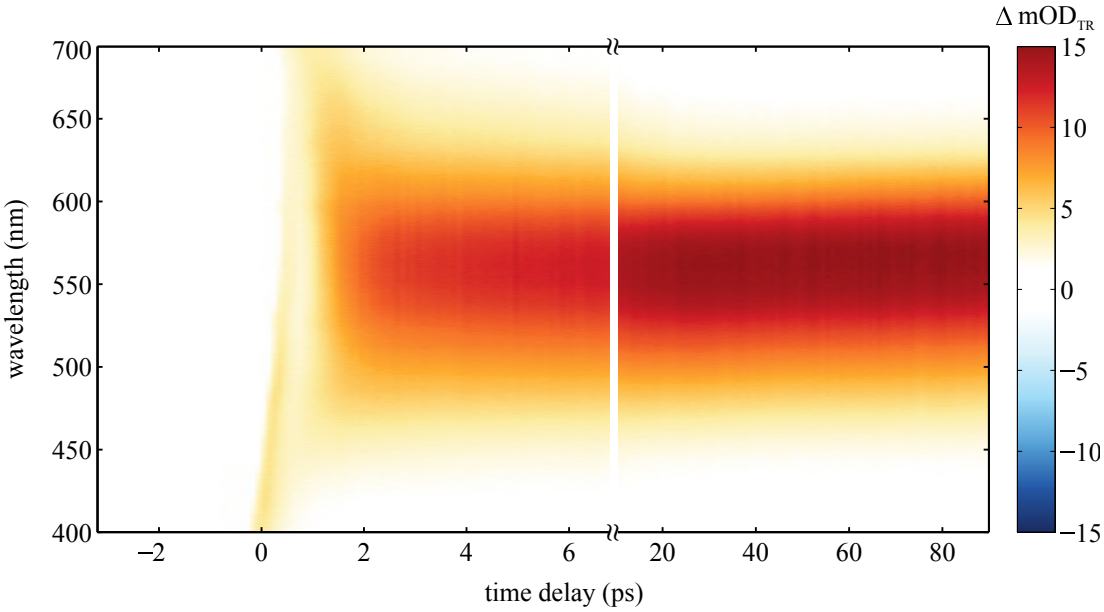

Figure 4.5: 2D transient absorption spectra corresponding to short and large steps (100 fs and 1 ps), respectively.

The spectra are an average of three separate runs of the experiment. The pump fluence was 0.46 mJ cm^{-2}. The colour bar reflects the magnitude of the absorption change, where red corresponds to an increase in the absorption and blue to a decrease in absorption.

In the short-delay range, two bands can be distinguished. A positive band featuring in the 400-450 nm region forms within the width of the instrument response and another, broad absorption band (500-600 nm) appears after about 1 ps. Fig 4.6 shows the kinetic traces taken for 430 nm and 600 nm. Bi-exponential fits of the data were carried out. Two exponents were necessary to fit the data in which one exponent was used to account for the decay or rise kinetics and

the other to the dynamics beyond 6 ps. The coherent artifact contribution was neglected in the fitting process. The decay constant of the 430 nm band was found to be approximately 580 ± 34 fs, while the rise time of 600 nm band was found to be about 800 ± 35 fs.

It is also interesting to note the spectral evolution in the visible region (Fig 4.7). Initially, a broad absorption band spanning all of the visible region is observed after 1 ps. The band grows more strong and its bandwidth becomes increasingly narrow for 80 ps, after which a constant state is reached that resembles the steady-state spectrum of the ground state merocynanine product.

These results were interpreted as follows: the 266 nm excitation prepares the SNO molecules in a high-lying singlet excited state (S_5), from where they undergo rapid internal conversion down to the S_1 state, at a rate much faster than can be measured by the instrument. The initial positive band at 400-500 nm region then corresponds to the $S_1 \rightarrow S_n$ absorption and the subsequent decrease is attributed to the decay of the S_1 state. The initially broad absorption in the visible region is likely due to a distribution of isomers that are created, most probably in hot vibrational state, which converge towards the most stable one as time evolves, causing narrowing of the spectrum and shift to slightly longer wavelengths ($\Delta E = 351.7\,cm^{-1}$ between 5 ps to 100 ps).

The evolution ends once the most stable configuration of the MC has been assumed (the trans-MC isomer) in around 100 ps. This interpretation is in line with literature [123, 125] results and verified that the setup was performing well.

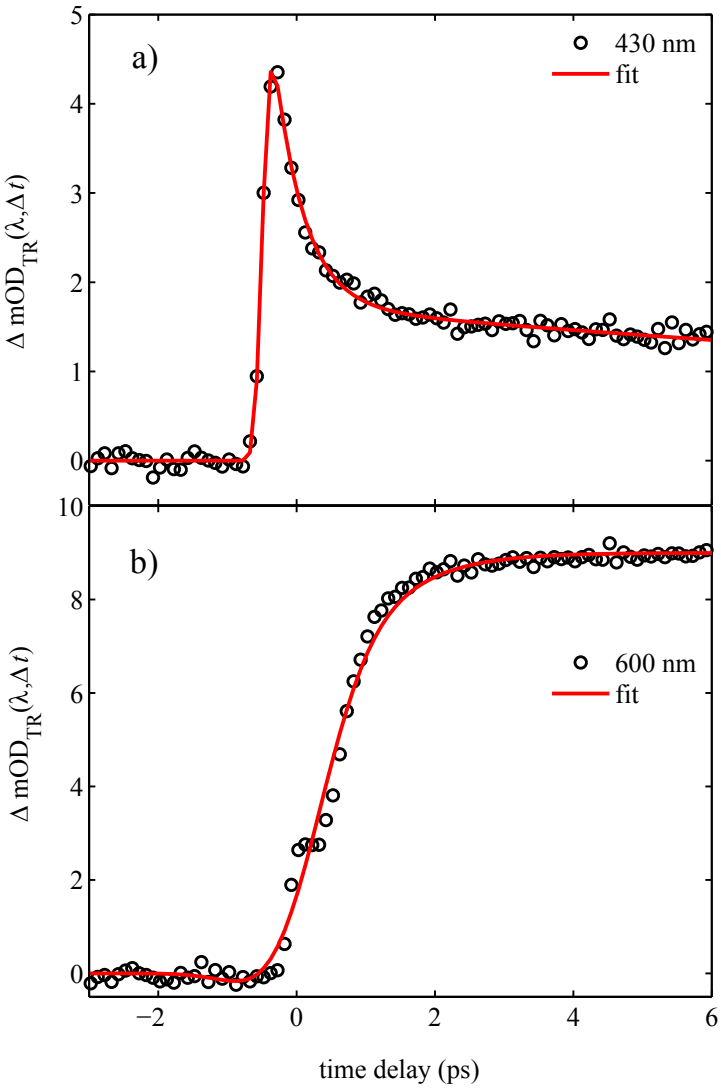

Figure 4.6: Kinetic traces for two wavelengths a) 430 nm and b) 600 nm. The decay in a) is attributed to the decay of the singlet excited state and the rise at 600 nm to the production of the merocynanine products. Note the offset in time-zero. Fitting in this case was done without chirp correction.

.

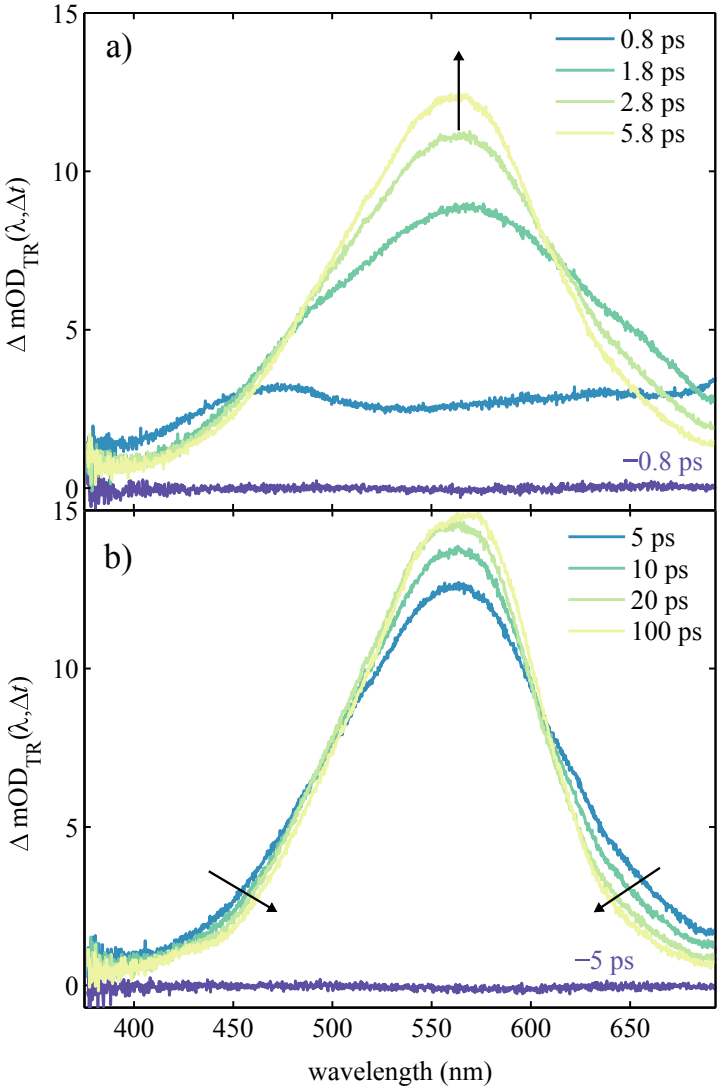

Figure 4.7: The evolution of the transient absorption spectra at different times over the course of the reaction. a) transient spectra from early time delays and b) from long time delays. The arrows show that as the system evolves, the visible band becomes increasingly stronger and narrower and after 80 ps when the steady-state has been reached.

.

4.3.4 Solid state experiments

4.3.5 Reversibility in the solid state

To show that synchronised photoreversion is required to achieve adequate reversibility, a control experiment was first performed, in which only two beams, namely the pump and the probe were used. The pump and probe laser parameters, such as repetition rates, pulse energies, were kept constant in the control and the three-beam experiments. Again, 266 nm light was used to initiate the dynamics and the fluence was set at 1.4 mJ cm^{-2}, corresponding to 7 % excitation of the sample (see calculation in Appendix A). The pump fluence was chosen keeping in mind electron diffraction experiments, where a reasonably high fraction of excited molecules is required to confidently recover time-resolved signals. The polarisations of the pump and the probe were horizontal with respect to the incidence plane of the crystal. While the polarisations of the laser beams are very important, as the absorption of light will be dependent on the orientation of the electric field vectors relative to the direction of the transition dipole moment of the molecule (maximum when parallel, zero when orthogonal), it was considered to be not very critical for the SNO crystal, as the molecules assume different orientations within the unit cell (see Fig 4.2). A polarisation dependence measurement was, therefore, not carried out. Besides, the main focus here was to demonstrate the effectiveness of the proposed three-beam method.

Fig 4.8a shows the measured 2D TA spectrum, $\Delta\mathrm{OD}_{\mathrm{TR}}(\lambda, \Delta t)$, from the control experiment. Once again, the time step for the measurements was 100 fs and over 800 averages of the probe (corresponding to 100 pump shots, as probe:pump ratio = 8:1) were performed per time step. As the 2D map shows, immediately after time-zero, a broad absorption feature spanning 400 nm to 500 nm is observed, which then starts to decay after about 1 ps. Curiously, a negative feature extending from 550 nm to 670 nm starts to appear after 2.5 ps and grows more and more intense during the course of the time scan. Spectral slices at selected time delays are shown in Fig 4.8b. The arrows in the figure indicate the trend in

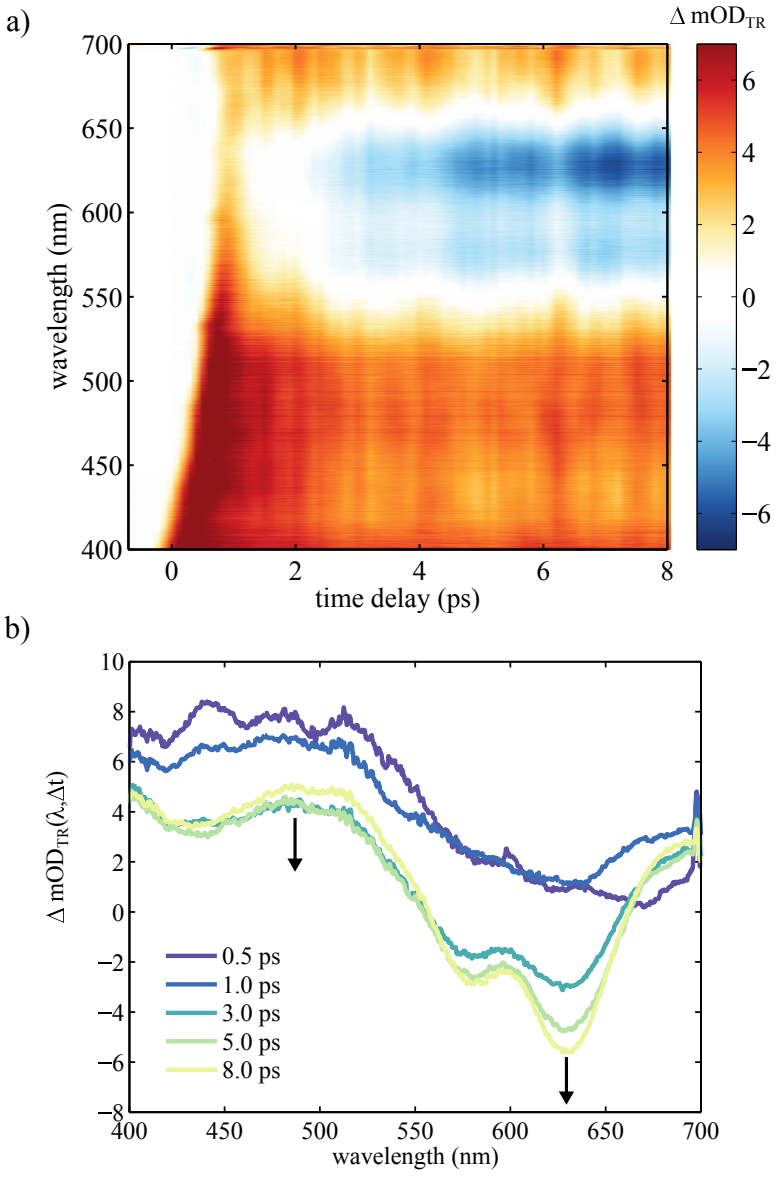

Figure 4.8: The results of two-beam experiment with 266 nm pump (1.4 mJ cm^{-2}) pump at 31.25 Hz. a) The 2D transient absorption spectrum and b) selected spectral traces.

the absorption change as a function of time delay. As was mentioned earlier, in addition to the transient absorption spectrum, a spectrum to monitor the photoproduct buildup was also measured and this is shown in Fig 4.9. Focusing our attention to this figure, it can be seen that the absorption in the probe region gradually grew with increasing number of pump laser shots hitting the sample and a constant value was reached after exposure of approximately 10^4 pulses. Upon reaching the steady-state, comparison with the spectrum of the MC measured in solution revealed almost identical absorption profiles (see Fig 4.4), except that the absorption maximum was shifted to longer wavelengths in the case of the crystal. This clearly points to the production of the merocynanine form in the crystals and importantly, needed nearly 1000 shots at this fluence before it could be detected. This result indicated that the merocynanine products were not returning back to the spiroform. The production of the MC form may be explained if one imagines that, intense excitation will create many ring-opened species, thereby disrupting the lattice somewhat and as more and more pump pulses impact the sample, more ring-opened species are formed and soon the periodic order is lost. This was indeed observed in diffraction experiments (performed prior to the transient absorption measurements), where discrete spots diffused out to a ring after a few hundred pump shots. While no information can be gleaned from the diffraction pattern as to the existence of the merocynanine state, if the long-range order has been lost, absorption spectroscopy can sensitively probe its formation because the merocyanine product will absorb light regardless whether the crystallinity is maintained or not. The slight loss of crystal order presumably provides some SNO molecules with enough local free volume to undergo isomerisation and form the MC. The MC which is then formed does not return to the spiro form (at least within the timescale of our experiments) and remains trapped. This trapped MC can get excited by subsequent 266 nm pulses, which results in the negative feature (due to depletion of the ground state population), corresponding to the bleach band seen in Fig 4.8.

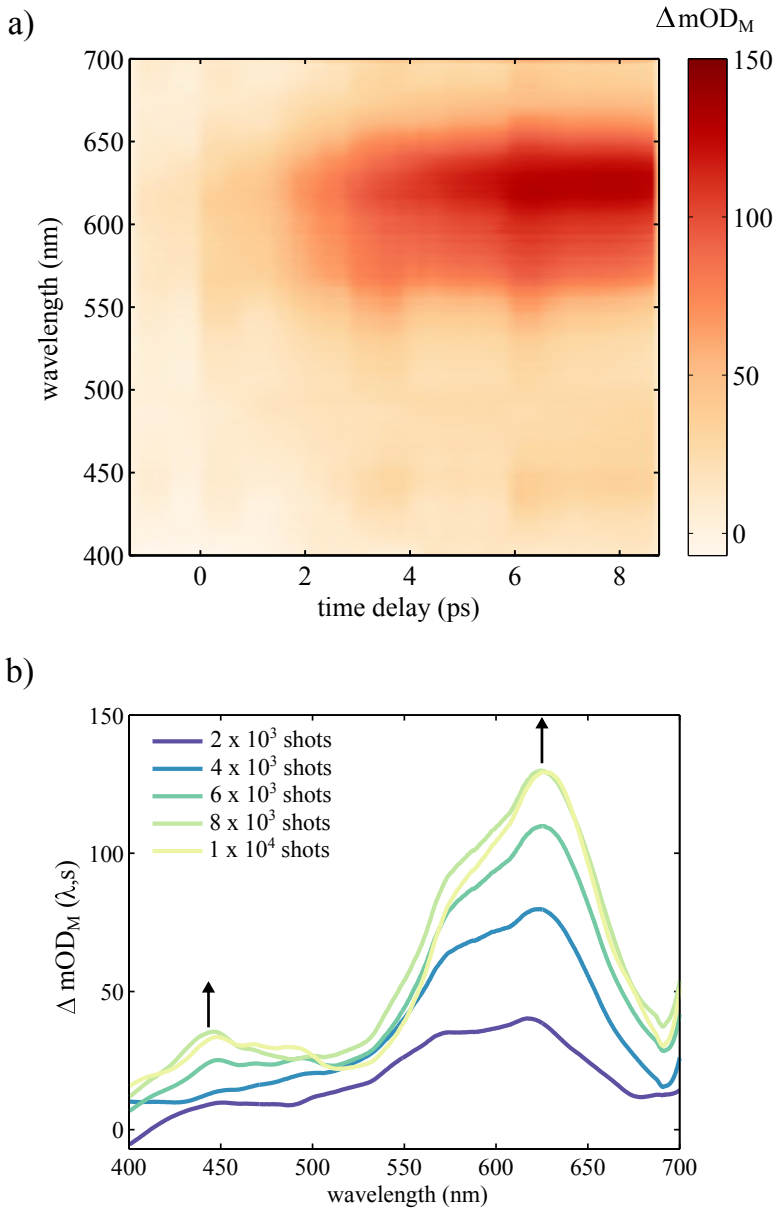

Figure 4.9: The results of two-beam experiment with 266 nm pump (1.4 mJ cm^{-2}) pump at 31.25 Hz. a) The 2D buildup map and b) the signal measured at 28 ms after excitation as a function of pump laser shots.

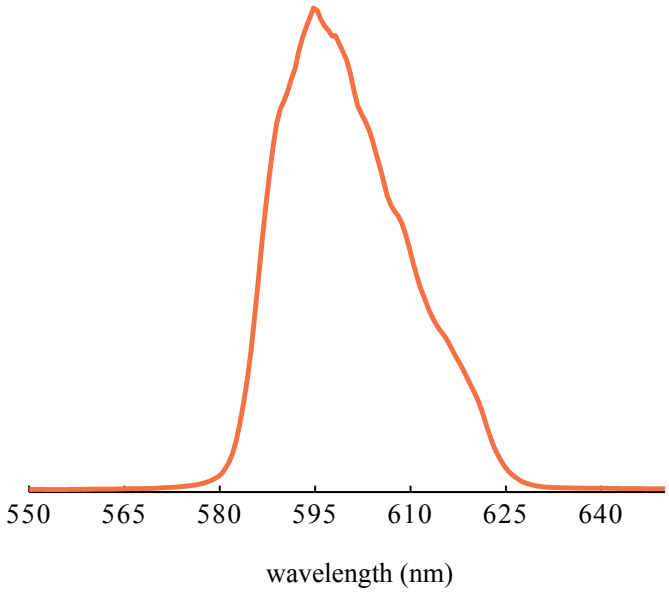

Figure 4.10: The spectrum of NOPA. The spectrum has a bandwidth of about 20-25 nm (FWHM).

It is also important to mention here that the buildup was seen regardless of the repetition rate used in the experiment. Measurements (not reported here) were performed where the pump repetition rate was set to be as low as 2.5 Hz (factor of 12.5 lower than that used above), but the absorption from merocynanine products was still observed, though it took more pump shots to detect it. The slow buildup in this case can be ascribed to longer relaxation time afforded to the crystal (400 ms intervals between pump pulses as opposed to 32 ms), whereby some ring-opened molecules can convert back to the spriooxazine form, but the key point here is that there was still a significant population that remained and their absorption was detectable, i.e. irreversible conditions.

After confirming that the conventional approach of using only two beams does not guarantee reversible conditions in our experiments, the three-beam experiment with the synchronised photoreversion scheme was performed. The photoreversion pulse from the NOPA was tuned close to the maximum of the photoproduct absorption (610 nm, see Fig 4.10 for NOPA spectrum) and the pulse energy was adjusted to a fluence of 2.8 mJ cm^{-2}. Fig 4.11 shows spectral traces corresponding to the same number of pump shots as in Fig 4.8 for compar-

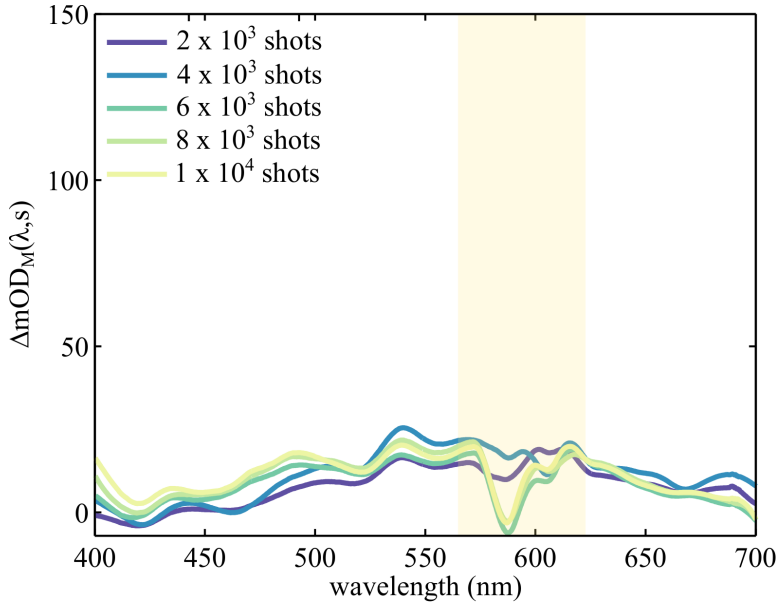

Figure 4.11: The buildup spectrum using the photoreversion scheme showing that even after 10,000 shots no significant population of photoproduct remains in the probe region. Yellow area denotes the region covered by the photoreversion pulse.

ison. It can be clearly seen that no significant amount of the product remained in the crystal, even after exposing the sample to over 10,000 pump shots. Indeed, the only variation in the absorption change is due to the fluctuations of the white light probe intensities and the NOPA beam, which is particularly noisy around 580-620 nm region. This result clearly demonstrates that an additional ultrashort beam, when used with the synchronisation scheme described above, can provide an effective way to arrest the amassing of the species (which do not revert back to their initial forms) produced in a photochemical reaction.

The crystal was inspected after the experiments described above and remarkably, the region on the thin crystal used in the control experiment showed marked colouration, due to permanent formation of merocyanine products, while the region that was used in the synchronised photoreversion experiment, could not be distinguished from unexcited regions (see photograph in Fig 4.12).

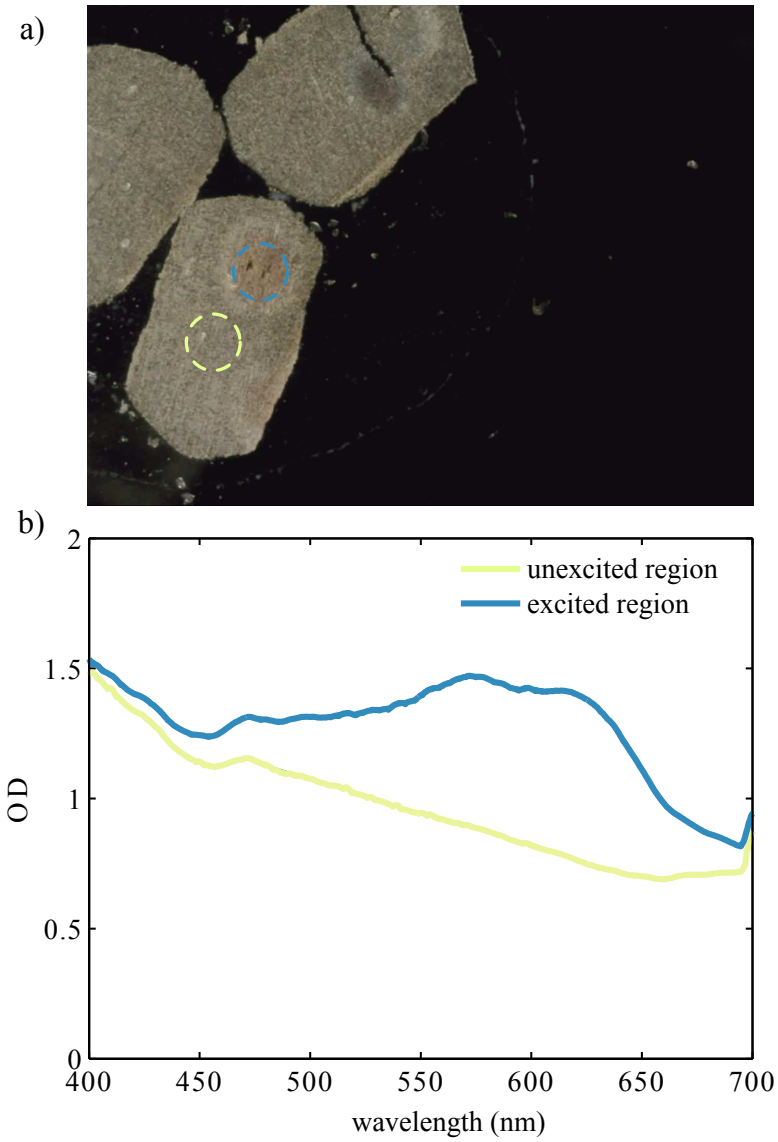

Figure 4.12: a) Photograph of the one of the samples used in the experiment. The blue dashed circle marks the region due to pump beam damage in the case of two-beam experiment and yellow circle corresponds to an unexcited region b) steady-state spectra from regions marked in a).

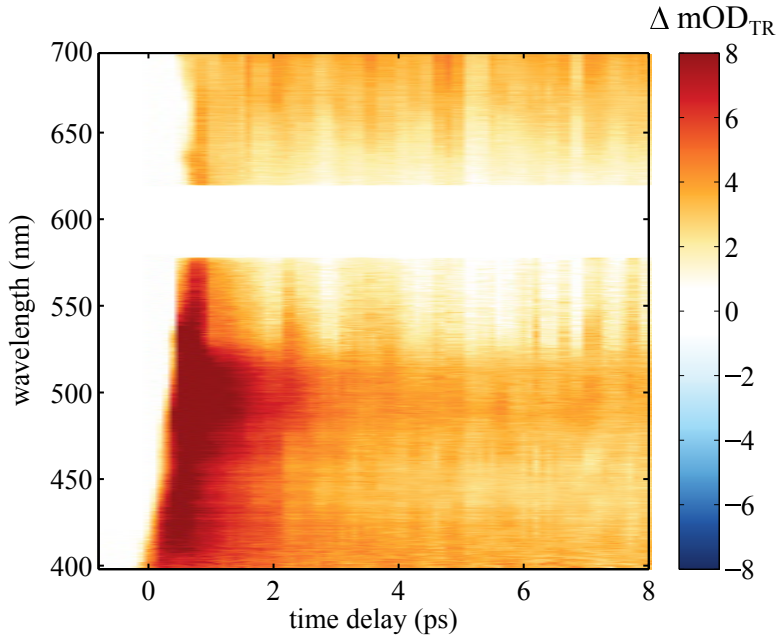

Figure 4.13: 2D transient absorption spectra of SNO crystal. The region due to signal from NOPA is masked.

.

Having ascertained that the sample was returning to the original state before each pump-probe sequence, transient absorption experiments were carried out. The data were collected from three different regions on the SNO crystal, each exposed to a total of 10^4 shots of the pump beam, and then averaged. Experimental conditions were the same as before. The 2D transient absorption map from the measurements is shown in Fig 4.13.

Similar to the two-beam experiment, a strong decaying absorption band (400-550 nm) with a peak at around 500 nm is observed immediately after excitation. Moreover, a positive absorption band is also detected at 650-700 nm, but it is much less intense than the 500 nm band. Fig 4.14 shows how the spectrum evolves with time. The 400-550 nm and the 650-700 nm bands decay after the initial rise, though the decay in the 400-550 nm region is much more pronounced than the 600-700 nm spectral region.

The time profile of 500 nm absorption is shown in Fig 4.15 and was fitted to yield a decay constant of 800 ± 32 fs. As was interpreted by Suzuki *et al*,

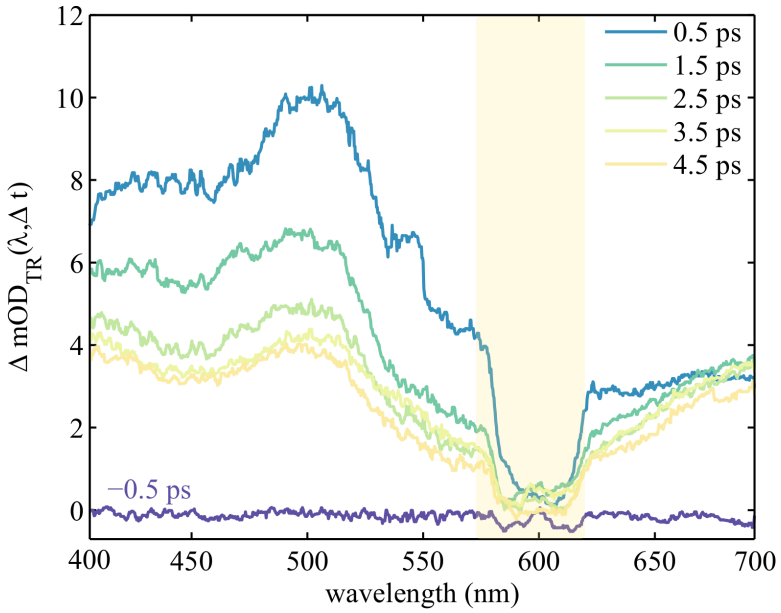

Figure 4.14: Spectral traces showing how the SNO spectrum evolves after excitation. The region obscured by the photoreversion beam is shaded in yellow.

.

this band is assigned to the decay of the S_1 state and to the production of ring-opened SNO, with orthogonal parent geometry, following the cleavage of the C-O bond. A noticeable difference from the solution phase transient absorption spectrum is the absence of absorption from merocyanine, which absorbs in 550-600 nm region. In solution, molecules have much more freedom to switch from one form to the other, but in the crystal, molecular packing will largely determine whether the ring-opened SNO molecules are able to fully isomerise to the MC form or not. As has been mentioned already, in a unit cell of SNO, a single SNO molecule is surrounded by at least seven other SNO molecules, so unless pockets of space are created in the crystal (due to product accumulation as in the two-beam experiment), the restriction imposed by the lattice makes isomerisation to planar MC highly improbable. Therefore, we arrive at a conclusion which agrees well with Suzuki's interpretation of their low excitation experiments.

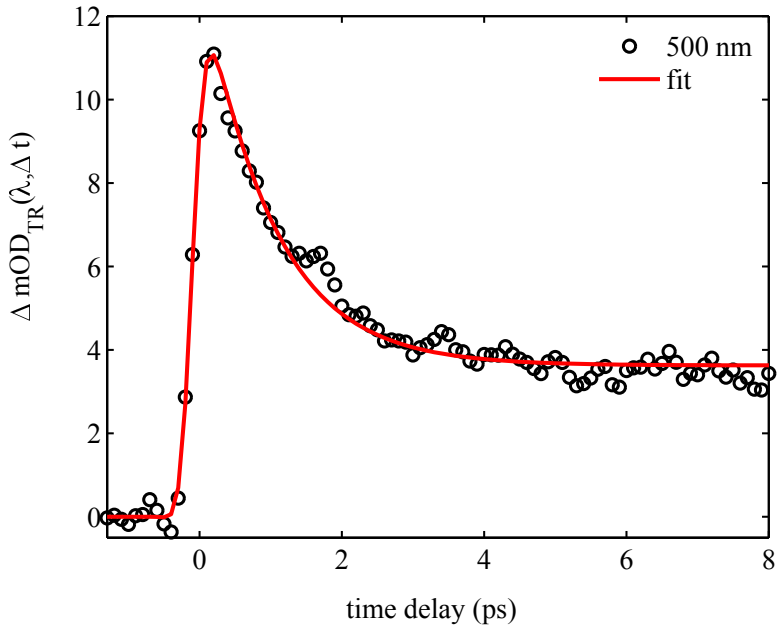

Figure 4.15: The kinetic trace for 500 nm absorption band and the corresponding fit.

.

To support the experiments, quantum chemistry simulations were run by a colleague in the group, Dr Kochman, on a single unit cell (selected from of a cluster of cells called a supercell), constructed by using the lattice constants taken from the crystal structure reported in [130] and placing eight symmetry-equivalent SNO molecules (in their parent geometry) inside it. The periodic boundary conditions were imposed, which made it possible to select one of the eight molecules to be 'excited' (see Fig 4.16). The geometry of this molecule was optimised using Møller-Plesset perturbation theory of the second-order (MP2), whereas other molecules were treated semi-empirically. Møller-Plesset is a post-Hartree-Fock (*ab initio*) method in which correlations between the electrons —which are omitted from the Hartree-Fock (HF) theory, are taken into account to improve on the HF solution. The correlation is treated as a perturbation and added to the Hamiltonian of the system and results in the stabilisation of energy, bringing it closer to the 'true' energy of the system. A cc-pVDZ basis set was used, where VDZ stands for valence double-zeta and 'cc-p' denotes correlation-consistent.

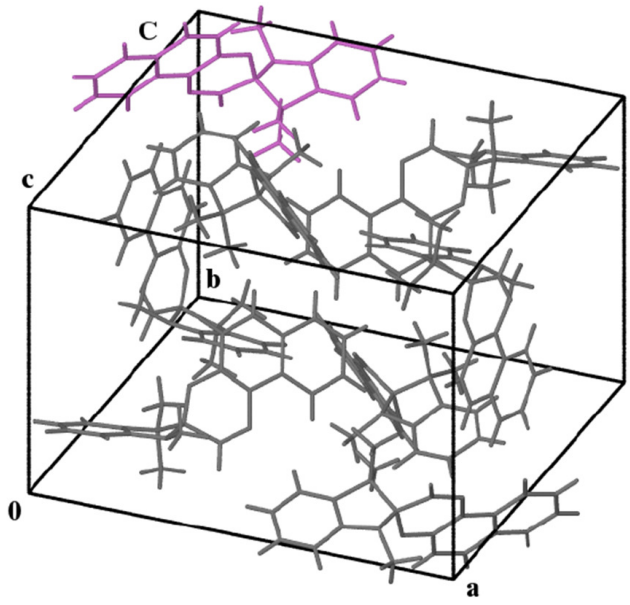

Figure 4.16: A unit cell with showing eight SNO molecules constructed for simulation. The molecule chosen for excitation is highlighted in violet.

.

Molecular orbitals (MO) describe the electronic behaviours of the molecules and are constructed from a linear combination of atomic orbitals (LCAO) (where an orbital is a one-electron function) [135]. The basis sets are functions (centered on the nuclei) that describe the orbitals. The larger the basis set, the better the description of the orbital and hence the electron density around an atom, but equally high is the computational cost. The chosen method with cc-pDVZ basis sets was found to describe well the packing of the molecules in the cell when compared with experimentally determined crystal structure. Dr Kochman ran the simulations using the computational chemistry software package, Turbomole version 6.3.1 [136]. The C-O bond of the selected molecule was manually sliced and the molecule was allowed to change its geometry without restriction. Geometry optimisation was carried out using the methods described above. The results of the simulation are shown in Fig 4.17.

As can be seen from the figure, the bond breaking resulted in the displacement of the two rings from their original crystallographic positions, but still

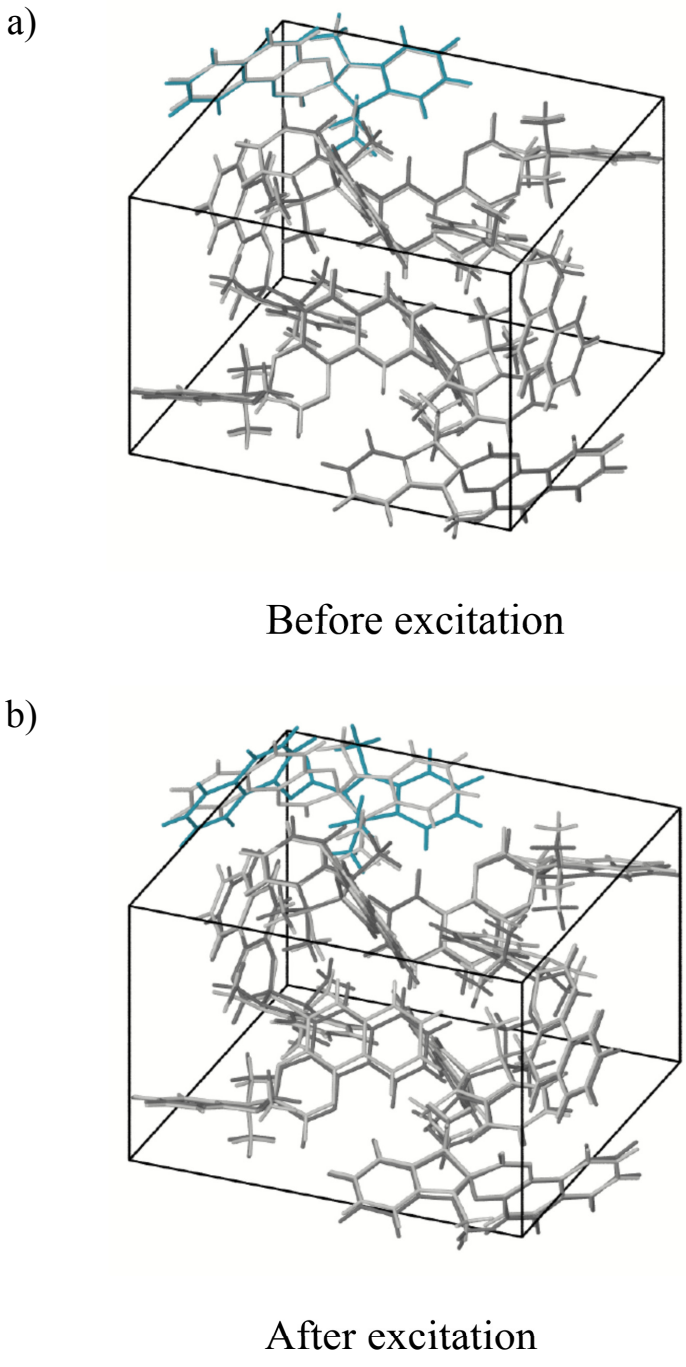

Figure 4.17: The results of the simulation. a) The unit cell showing the selected SNO molecule before bond-breaking and b) after bond-breaking and structural change.

maintained their orthogonal relationship. Some SNO molecules are also somewhat shifted from their original positions in the crystal, though it is not very obvious due to congestion of molecules in the cell. Nevertheless, this simulation clearly predicts the production of a ring-opened species, relating to excited SNO molecules, which can not undergo isomerisation to planar merocyanine products. Dr Kochman also computed the vertical excitation energies corresponding to SNO and the ring-opened form (o-SNO) in the crystal and these are plotted in Fig 4.18 along with the oscillator strengths. Algebraic diagrammatic construction (ADC) method [137] was employed and a def2-SV (P) basis set was used for this purpose. An intense transition located at 450 nm can be seen, but transitions in 550-600 nm region are clearly absent. These results compare favourably with the experiments in which the 550-650 nm spectral region lacked absorption signature. The intermediate with 500 nm absorption peak is, therefore, assumed to be a ring-opened form of SNO, in which the oxazine and indoline rings remain orthogonal to each other.

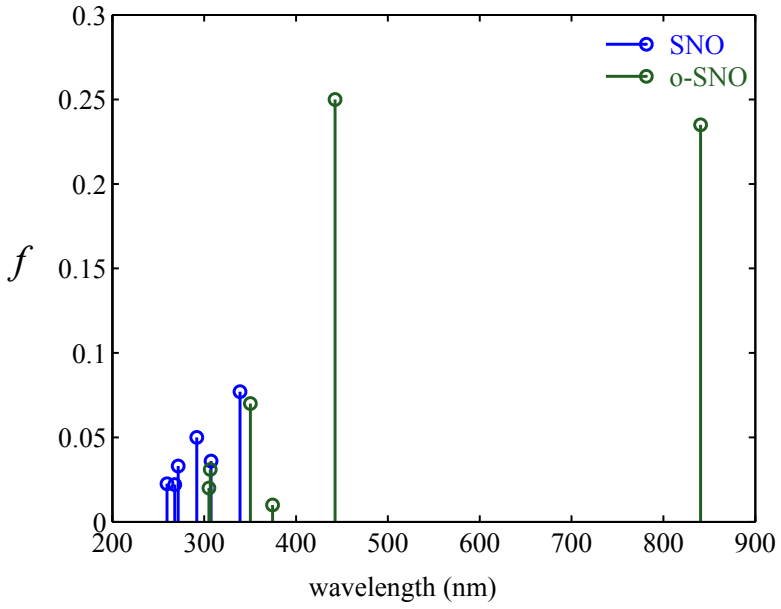

Figure 4.18: Plot showing the probabilities of transitions computed for SNO and the ring-opened isomer (o-SNO) formed inside the crystal.

Finally, what effect that the photoreversion beam can have on the sample, other than converting products back, needs to be considered. Recall that, SNO is completely transparent in the visible region (due to the orthogonal rings), which means that the photoreversion beam will pass through (unexcited) SNO crystal without being absorbed. This can, of course only be true if the peak intensity remains within the limit of single photon absorption, i.e. below the multi-photon absorption threshold. Though the pulse duration of the NOPA (the photoreversion) beam was not measured, it is estimated to be around 500 fs, on account of the fact that no compression of the beam was attempted and additionally it passed through a few transmissive optics *en route* to the sample. Using this as our estimate for the pulse duration, the peak intensity $\left(\text{peak intensity (W cm}^{-2}) = \frac{\text{fluence (J cm}^{-2})}{\text{pulse duration (s)}}\right)$ at the fluence used (2.8 mJ cm^{-2}) works out to about 5.6×10^9 W cm^{-2}, which is below the multiphoton threshold (typically $> 10^{10}$ W cm^{-2} in solids). The fact that no unusual features appear in Fig 4.11 confirms this and shows that NOPA beam performs only one function; that of photoreversion.

4.4 Conclusion

It was shown in this chapter that by using an ultrashort, post-excitation pulse, it is possible to prevent the buildup of the photoproducts being formed in a constraint environment such as a crystal. It was demonstrated that should the photoproducts be allowed to accumulate, not only would the measured signals contain contributions from unrecovered species (which can easily lead to wrong assumptions regarding the dynamics), but it irrefutably leads to damage of the crystalline sample. Ultrafast studies of photochemical reactions have largely been limited to single-shot techniques due to this reason. Synchronised photoreversion represents an alternative approach to single-shot methods as it can help circumvent product buildup issue and as such, provide an actual account of the dynamics of the chemical reaction in solids. This "recover before destroy" ap-

proach uses the 'pump-probe-recover' scheme and can be applied, in principle, to any system as long as there is a well-defined absorption for the photoproduct state that allows selective back pumping. Photochromic systems, of which there are many, will readily fulfill this requirement. Furthermore, it is equally notable that this method should provide the prospect of probing dynamics of the back reactions (where applicable) and thus, can help to develop a complete picture of bi-directional chemical processes.

That said, there is still room for optimisation and further avenues to explore. For instance, it would be interesting to calibrate the effect of the photoreversion beam once a significant population of the photoproducts has been accumulated. For example, in the work mentioned here, due to the large difference in the relative repetition rates of the pump and the photoreversion beams, the population of the unwanted species was removed whilst the pump beam was off for a significant amount of time. If the photoreversion can be performed equally efficiently with the pump beam operating at much higher repetition rates (so giving the photoreversion pulse much less time to remove the species between pump shots), then this would lead a great improvement in the signal-to-noise ratios, as more data could be obtained from a single experiment. It will also be helpful to fully characterise the photoreversion beam and to perform measurements with different pulse durations of the beam to monitor the effect on the photoreversion process. Finally, in the experiments described above, the photoreversion beam was almost normal to the crystal surface and scattering from the crystal walls reached the detector, obscuring the region of the beam spectrum. In this work, the spectral bandwidth of photoreversion beam was narrow enough that it was still possible to look for the signature (if any) of MC product absorption, but it may not be true in other cases. Therefore, it would be important to eliminate the scattering signal completely. A change of incidence angle will be attempted as a first step to counter this issue.

Experiments with SNO crystals using synchronised photoreversion showed no evidence for the formation of merocynanine, instead a transient that lived for the

duration of the time-resolved scan was observed. The rationale given for this was the constraint imposed by the crystal lattice, which allows bond breaking and ring opening, but any large conformational changes are prohibited. The structure of the transient is speculated to be close to that of the parent molecules, but with the C-O broken and with slight displacement of the indoline and oxazine rings, based on the results of the simulations carried out by Dr Kochman and from what is predicted in the literature. It is anticipated that time-resolved electron diffraction experiments should be able to shed more light on the intermediate and are currently being pursued in the lab.

Chapter 5

Time-resolved Crystallography: Introduction and Methodology

A large part of the thesis work also focused on applying diffraction techniques to study different systems, of which one forms the theme of the next chapter. Diffraction is the bending of waves around an edge of an object, which then interfere constructively (add up) or destructively (cancel out). Thomas Young discovered the wave properties of light by performing his famous double-slit experiment in 1803 [138]. Later, Louis de Broglie in 1924 proposed the wave-particle duality of matter [139] and Clinton Davisson and Lester Germer carried out an experiment at Bell Labs in 1927 to measure the energy of the electrons, scattered from the surface of a nickel crystal and observed diffraction, thus confirming de Broglie's hypothesis [140]. We exploit the wave nature of electrons in the femtosecond electron diffraction experiments. Mostly, samples that we used were crystalline. This chapter, therefore, introduces some concepts relating to crystallography and also provides a description of the experimental setup.

5.1 The crystal system

A crystal can be defined simply as a periodic arrangement of atoms or molecules, held together by interatomic/intermolecular forces. Due to the periodicity, translational symmetry is an intrinsic property of crystals [1]. A crystal can be represented by an infinite array of points called a real (or direct) lattice, where each *lattice point* represents either an atom or molecule (a basis or motif, in crystallographic terms) and has identical environment. Within this lattice framework, it is convenient to subdivide the lattice into small entities called unit cells, which when translated in three dimensions can reproduce the original lattice. The unit cell is then any parallelepiped whose vertices are the lattice points. It is characterised by the three distinct lengths of the edges and three distinct angles, subtended by the edge of the parallelepiped (see Fig 5.1), which collectively are known as the lattice parameters or unit cell constants. To specify the location of an atom in a unit cell, a lattice vector from the origin is defined

$$\mathbf{r}_i = \mathrm{x}_i\mathbf{a} + \mathrm{y}_i\mathbf{b} + \mathrm{z}_i\mathbf{c} \tag{5.1}$$

where $\mathrm{x}_i\,, \mathrm{y}_i$ and z_i are fractional coordinates used conventionally in crystallography and **a**, **b** and **c** are the basis vectors of the cell. Although there is no restriction on the choice of the unit cell , e.g. on its shape, certain conditions must be met. For example, the unit cell type should fill the space without leaving any gaps. A polygon-type cell, with a five-fold rotational symmetry (it remains unchanged if rotated by 72° about the rotational axis), will violate this condition and as such does not exist in crystallographic reading. It is noteworthy to mention that symmetry will play a crucial role in determining which type of unit cell will be allowed. The lattices formed by the unit cells that completely fill the space are known as Bravais lattices. Thus, the crystallographic crystal system is composed of unit cell types that can form the Bravais lattices. There are a total of seven types that contain exactly one lattice point and are called primitive unit

[1] A special case is that of a quasicrystals, which lack the translational symmetry, but are ordered [141].

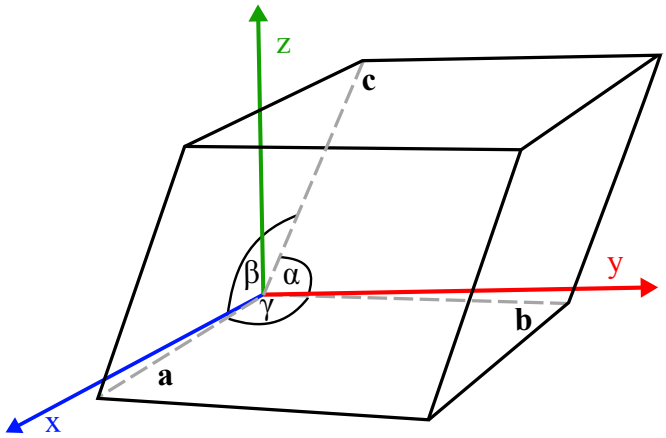

Figure 5.1: The definition of the unit cell parameters.

cells and seven non-primitive cells, which contain more than one lattice point per unit cell. These have either a lattice point at the faces (face-centred) or in the centre (body-centred).

Crystallographers often like to define a minimum set of atoms (ions or molecules) that, after applying the necessary symmetry operations, are able to reproduce the whole content of the unit cell. The unit, that contains the set, is known as the asymmetric unit. If the asymmetric unit is known then there is no need to determine the position of every atom in the unit cell in order to describe the complete crystal structure.

Aside from the concepts introduced above, another very useful one is that of crystal planes. A crystal or lattice plane is one which consists of at least three lattice points. In a diffraction experiment, the incident waves are scattered from the crystal planes, the orientation of which can provide information about the arrangement of the atoms. In order to label (index) a plane, Miller indices (h k l) are used and h, k, l are all integers, which define the reciprocals of the fractional intercepts, which the plane makes with the crystallographic axes. For example, a plane with indices (h k l) cuts the **a**, **b** and **c** axes with $1/h$, $1/k$ and $1/l$ intercepts. Notice that, the indices of a plane are enclosed by round

brackets, but for a family of planes[2] curly brackets are used. A set of planes, whose intersections are parallel, form a zone and the direction of intersection is called the zone axis. The notation for a zone axis is [UVW], where U, V, W are integers. As an example, a set of parallel planes with Miller indices (h k 1) belong to the [001] zone axis.

5.2 Bragg's Law

After the discovery of x-rays by Röntgen in 1895, it was soon realised that they could be used to study structure of materials by exploiting diffraction. The first x-ray crystal diffraction experiment was performed by Sommerfield in 1912 [142] and Max von Laue laid down the theory of diffraction in crystals in the same year, but it was the work of father and son duo of W.H.Bragg and W.L.Bragg in 1913 that elegantly described the process [143]. Together, they devised what is now known as the Bragg's law, which describes the geometrical conditions under which diffraction can be observed. Fig 5.2 illustrates the law graphically.

Two rays that are initially in phase are incident upon a set of planes of atoms in a crystal and are scattered. One of the rays is 'reflected' off an atom in the outer plane and the other from an atom in the inner plane. The distance travelled by the first ray is shorter than the second ray, which travels an extra distance of BC + CD. Bragg's law says that, if the two rays are to be in phase after scattering, the extra distance must be an integral multiple of the wavelength λ , i.e. nλ = BC+ CD. Using simple trigonometry

$$\mathrm{BC} = d \sin\theta. \tag{5.2}$$

where d is the interplanar spacing. Recognising that BC = CD, Bragg's law is then given as

[2]Set of equivalent planes. For a cubic lattice, a family of plane is given by all possible permutations of the h,k,l indices

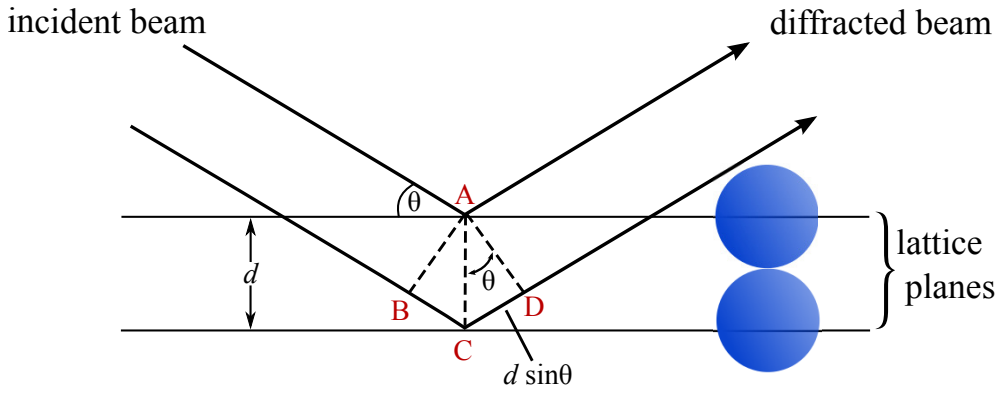

Figure 5.2: Illustration of the Bragg's law.

$$n\lambda = 2d\sin\theta \tag{5.3}$$

where θ is known as the Bragg angle.

A remarkable feature of Bragg's law is that it can be used to describe diffraction not only with x-rays, but also electrons. As electrons are used in this thesis work, it is useful to define some of the properties in relation to the experiments.

The de Broglie wavelength of the electrons is given by

$$\lambda_e = \frac{h}{m_e v} \tag{5.4}$$

where h is the Planck's constant ($h = 6.02 \times 10^{-34}$J s), m_e is the mass of electrons and v is the velocity. At very high acceleration voltages, electrons travel close to the speed of light and their mass is not the same as the rest mass, thus their wavelength is worked out using relativistic theory.

$$\lambda_e = \frac{h}{\sqrt{2em_eV + \left(\frac{e^2V^2}{c^2}\right)}} \tag{5.5}$$

where V is the accelerating voltage, c is the speed of light ($c = 2.998 \times 10^8$ m s^{-1}) and e is the elementary charge (1.6×10^{-19} C). For electrons accelerated at the voltage of 110 kV, the wavelength is 3.51×10^{-12} m (or 3.51 pm), which is several

times shorter than the typical bond distances (100 pm).

5.3 The reciprocal space

Earlier, the concept of lattice was introduced which provided a convenient way to describe the arrangement of atoms in the crystal. The description of the lattice was given in relation to the real crystal or in the 'direct space'. A lattice can also be described in an imaginary space, known as the reciprocal space (also called the momentum (k) or Fourier space), in which the relationship to the direct lattice is a reciprocal one. That is to say, a large separation in the direct space constitutes a small one in the reciprocal space. The existence of reciprocal lattice is a consequence of the periodic nature of the direct lattice and is connected through it by Fourier transformation. While the actual physical properties of a crystal are related to the real lattice, the reciprocal lattice picture conveniently describes how waves (x-rays or electrons) interact with the crystal.

The definitions of the basis vectors of the reciprocal lattice are

$$\begin{aligned} \mathbf{a}^* &= \frac{\mathbf{b} \times \mathbf{c}}{\mathrm{V}} \\ \mathbf{b}^* &= \frac{\mathbf{a} \times \mathbf{c}}{\mathrm{V}} \\ \mathbf{c}^* &= \frac{\mathbf{a} \times \mathbf{b}}{\mathrm{V}} \end{aligned} \tag{5.6}$$

where $\mathbf{a}$, $\mathbf{b}$ and $\mathbf{c}$ are real space lattice vectors and V is the unit cell volume given by $\mathbf{a} \cdot (\mathbf{b} \cdot \mathbf{c})$. Furthermore, the above relations show that $\mathbf{a}^*$ is perpendicular to the direct lattice vectors $\mathbf{b}$ and $\mathbf{c}$, $\mathbf{b}^*$ is orthogonal to $\mathbf{a}$ and $\mathbf{c}$ and similarly, $\mathbf{c}^*$ to $\mathbf{a}$ and $\mathbf{b}$. A point in the reciprocal lattice is described by the reciprocal lattice vector

$$\mathbf{g}_{hkl} = h\mathbf{a}^* + k\mathbf{b}^* + l\mathbf{c}^* \tag{5.7}$$

where h, k and l are the Miller indices. An important property of the recip-

rocal vector, $\mathbf{g}_{hkl}$ is that it also has a reciprocal relationship with the interplanar distance, d

$$\mathbf{g}_{hkl} = \frac{1}{d_{hkl}} \tag{5.8}$$

Therefore, each point in the reciprocal lattice can not only represent the direction of a related crystal plane, but also the spacing between planes. The waves that are diffracted by the crystal planes will appear as 'peaks' in the reciprocal space. Moreover, the symmetry in the reciprocal space reflects also the symmetry in the real space. If the direct lattice is primitive, the reciprocal lattice also becomes primitive. Finally, a detector will measure the reciprocal lattice, if, it is placed in the Fourier plane (this describes exactly the diffraction experiment), so it becomes clear to see the usefulness of the reciprocal space concept.

5.3.1 The Ewald's sphere

The Ewald's (pronounced 'A-valt') sphere, named after the German crystallographer Peter Ewald, is a geometric construct that describes the conditions necessary to observe diffraction in the reciprocal space as opposed to the direct space, that is to say, it illustrates the fulfilment of Bragg's law in the reciprocal space. The Ewald's sphere shows which sets of planes are at (or close to) their Bragg angles for diffraction to occur. A two-dimensional representation of the Ewald's sphere, sketched over the reciprocal lattice, is shown in the Fig 5.3. Whenever the sphere intersects a lattice point, the Bragg condition is fulfilled. A beam incident on a crystal with wave vector, $\mathbf{k}_0$ and magnitude, $\frac{1}{\lambda}$ will be scattered and the scattered beam has the wave vector, $\mathbf{k}_s$. The energy and momentum are conserved (elastic scattering) in the process so that

$$\begin{aligned} \Delta\mathbf{k} &= |\mathbf{k}_\mathrm{s} - \mathbf{k}_\mathrm{i}| \\ &= 2\frac{1}{\lambda}\sin\theta \end{aligned} \tag{5.9}$$

As the two waves have the same length, the scattering vector, Δk must lie on the surface of the sphere (radius$\frac{\pi}{\lambda}$). Because, $\Delta\mathbf{k} = \mathbf{g}_{hkl} = \frac{1}{d_{hkl}}$ (Eq 5.8), Eq 5.9 can

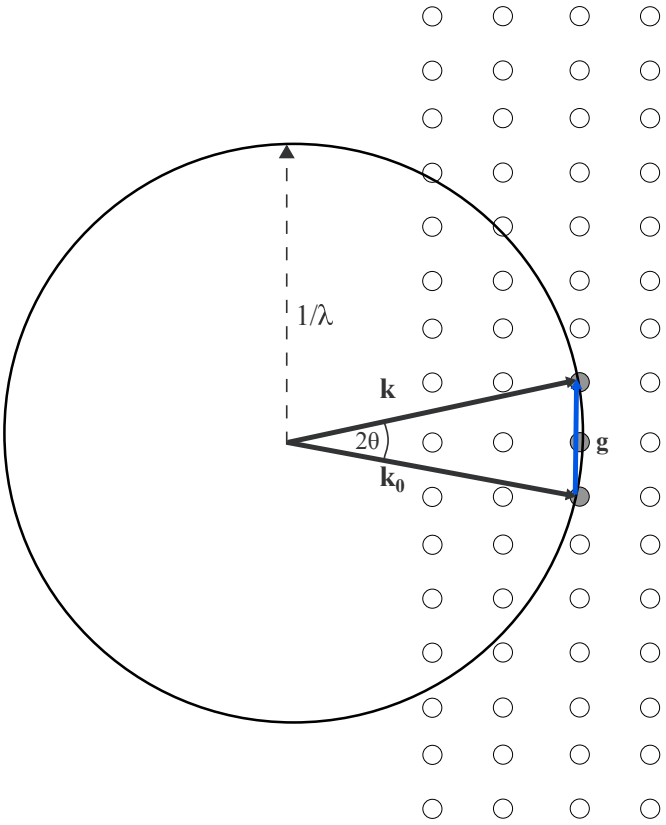

Figure 5.3: The Ewald sphere construction.

be rearranged to show that it leads to Bragg's law.

It should be said that, if the points in Fig 5.3 were truly points in the reciprocal space (as they would be in case of an infinitely large, ideal crystal) and if the beam were monochromatic (containing only a single wavelength) with the crystal oriented along a zone axis, then the Ewald sphere may not intersect reciprocal lattice points at all and diffraction will not be observed. However, in reality due to several reasons, such as the mosaicity of the measured specimen, i.e. presence of domains of different sizes or some other imperfections, not to mention the finite dimensions, reciprocal points have finite dimensions and shapes. When very thin samples are used (as in the case of electron diffraction experiments, see later) the reciprocal points elongate to rods (and so are called relrods), as dictated by Fourier transformation. Also, as the radius of the Ewald sphere depends on the wavelength, a polychromatic beam or an beam with a wavelength (energy) spread will produce a distribution of radii, which will act to thicken the sphere.

And finally, because the radius of the sphere is a reciprocal of the wavelength, electron with their far shorter wavelength as compared to x-ray produce a nearly flat sphere. As a result, several lattice points are intersected by the sphere, fulfilling the Bragg condition to a variable extent and causing the spots to be observed in the experiment. By contrast, the Ewald sphere of the x-rays, with their much longer wavelengths as compared to the electrons, is much more curved, resulting in fewer reciprocal points cutting the sphere, which is why crystals need to be rotated over many angles (often covering the whole 360°) in order to collect enough number of reflections to enable structural analysis.

5.4 The Structure factor

The structure factor, F_{hkl} is a central concept used to account for the observed features in a diffraction pattern. It is the Fourier transform of the electron density and, therefore, contains information on the locations of atoms within a unit cell. The structure factor can be written as the sum of the A_i terms, where $A = f_i e^{i\phi}$, f_i are the atomic form factors and represent the scattering power of atoms (heavier the atoms, the higher the scattering power) and the exponential term contains the phase information. The expression for the structure factor is

$$\begin{aligned} \mathrm{F}(hkl) &= \sum_{n=1}^{N} f_n e^{i\phi_\mathrm{n}} \\ &= \sum_{n=1}^{N} f_n(Z, d_{hkl}) e^{2\pi i(h\mathrm{x}_n + k\mathrm{y}_n + l\mathrm{z}_n)} \end{aligned} \tag{5.10}$$

where Z is the atomic number, N is the number of atoms per unit cell and x_n, y_n, z_n are fractional coordinates of the nth atom. The structure factor is a complex quantity and as such, only the product of F_{hkl} with its complex conjugate can be directly measured in a diffraction experiment

$$I = \mathrm{F}^*_{hkl}\mathrm{F}_{hkl} = |\mathrm{F}_{hkl}|^2 \tag{5.11}$$

where the above relation shows that the measured intensity is proportional to the square of structure factor amplitudes. Therefore, only the moduli of the structure factor amplitudes can be recovered from the diffraction experiment and the phase information is lost. This is the root cause of the well known phase problem in crystallography [144], which is a hindrance for structural determination, but fortunately many computer software exist today that use algorithms, which are based on methods that can solve the phase problem [145]. Notice that, the expression used for structure factor in Eq 5.10 did not include the effect of temperature. Atoms are not stationary in crystals; they jiggle about their equilibrium positions. An increase in temperature, however, can lead to displacements further away from the equilibrium positions and should be accounted for. The form factor due to temperature rise, f_T is given by

$$f_T = f e^{-\left(\frac{B \sin^2}{\lambda^2}\right)} \tag{5.12}$$

where B is often referred to as the temperature or Debye-Waller factor and is given by $B = 8\pi < u^2 >$, where u is the root mean square displacement of the atom from its average position. Consequently, the structural factor, with temperature effects included, becomes

$$\mathrm{F_T}(hkl) = \mathrm{F}(hkl) e^{-\left(\frac{B \sin^2}{\lambda^2}\right)} \tag{5.13}$$

An increase in the temperature factor, B reduces the structure factor.

Having discussed the concepts of reciprocal space, Ewald sphere and structure factors, a short discussion on the features seen in a diffraction pattern is useful. There is a lot of information that can be gleaned from a diffraction pattern about a specimen. If the specimen is crystalline in nature, then the appearance of the diffraction pattern can reflect the nature of the crystalline phases. For example, a highly oriented (or single) crystal (those exhibiting an undisturbed periodic structure over the whole area, i.e. no grain boundaries) specimen with its zone axis oriented parallel to the electron beam direction will typically give

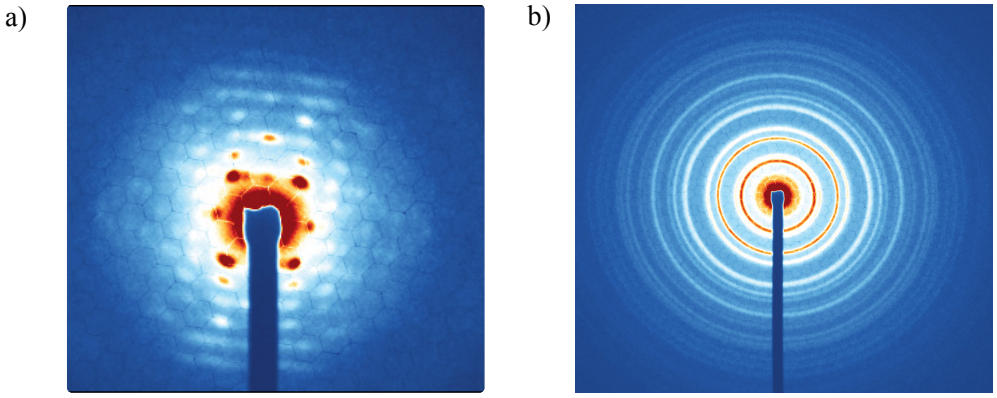

Figure 5.4: Two different patterns reflecting different nature of the crystal order. a) diffraction pattern from a single crystal and b) a polycrystalline sample.

rise to a pattern that consists of a regular array of spots on the detector. The intensities of the spots are determined by the corresponding structure factors. If the specimen is polycrystalline (consisting of many small single crystals that are randomly oriented), however, then rings (sometimes called Debye-Scherrer rings, if the specimen is powdered) corresponding to an average of all the orientations of the crystallites are produced. This is shown in Fig 5.4. Sometimes amorphous films are used as substrates for some specimen. In such films, long-range order is absent and their diffraction pattern consist of diffuse concentric rings. It is also noted that in the diffraction pattern, there exists a centre of inversion. This means that each point in the reciprocal space with indices *h,k,l* is related to an equivalent point with indices, *-h,-k,-l*. This feature is present in the diffraction pattern at all times (except in case of anamolous scattering) and according to Friedel's law, the related points form a pair that have equal amplitudes, but opposite phases.

$$\begin{aligned} |\mathrm{F}_{hkl}| &= |\mathrm{F}_{\bar{h}\bar{k}\bar{l}}| \\ \phi_{hkl} &= -\phi_{\bar{h}\bar{k}\bar{l}} \end{aligned} \tag{5.14}$$

5.5 The FED setup

This section describes the FED setup[3] which can be broken down into three different parts: the electron gun chamber, the sample chamber and the detection unit. A schematic of the setup is shown in Fig 5.5.

The electron gun chamber is a cylindrically symmetric stainless steel chamber, pumped by a turbomolecular pump (VP) to pressures down to 10^{-8} mbar. It is here that the generation of electrons takes place and therefore, houses the photocathode assembly. The photocathode is made from a thin layer of Gold (Au, 30 nm thickness), which is deposited onto a 1 mm thick round sapphire disk by thermal vapour deposition. A 5 nm thin layer of chromium is coated on the disk before the deposition. Chromium provides Au with the necessary adhesion to cling to the disk whilst remaining completely transparent to the laser beam. The reason for choosing sapphire as the material for the substrate is because it provides high transmissivity of nearly 80 % over a large wavelength window (0.17-5.5 µm). The cathode is placed inside a holder made from an insulating glass ceramic material known as Macor. Besides providing good insulation, other advantages of using a Macor are its excellent vacuum compatibility and easy machinability. The holder is placed about 12 mm from the anode plate, which is made from a highly polished thin-Silicon wafer (0.5 mm thickness) with a hole drilled at the centre (700 µm diameter). A negative bias is applied to the cathode through contact with a high-voltage (HV) feedthrough, which transfers high voltage from the power supply (maximum voltage = 200 kV) to the cathode. A potential difference is formed between the cathode and the earthed anode plate. When a voltage of -110 kV is applied to the cathode, a field gradient of 9.17 MV/m can be reached. High field gradients are important for achieving high brightness and shorter electron bunches. High vacuum is also essential in order to maintain high field strengths. A pinhole (120 µm diameter) is placed after the anode to collimate the beam.

[3]The design and construction was undertaken by Dr Hayes. Other details relating to the setup can be found in [146].

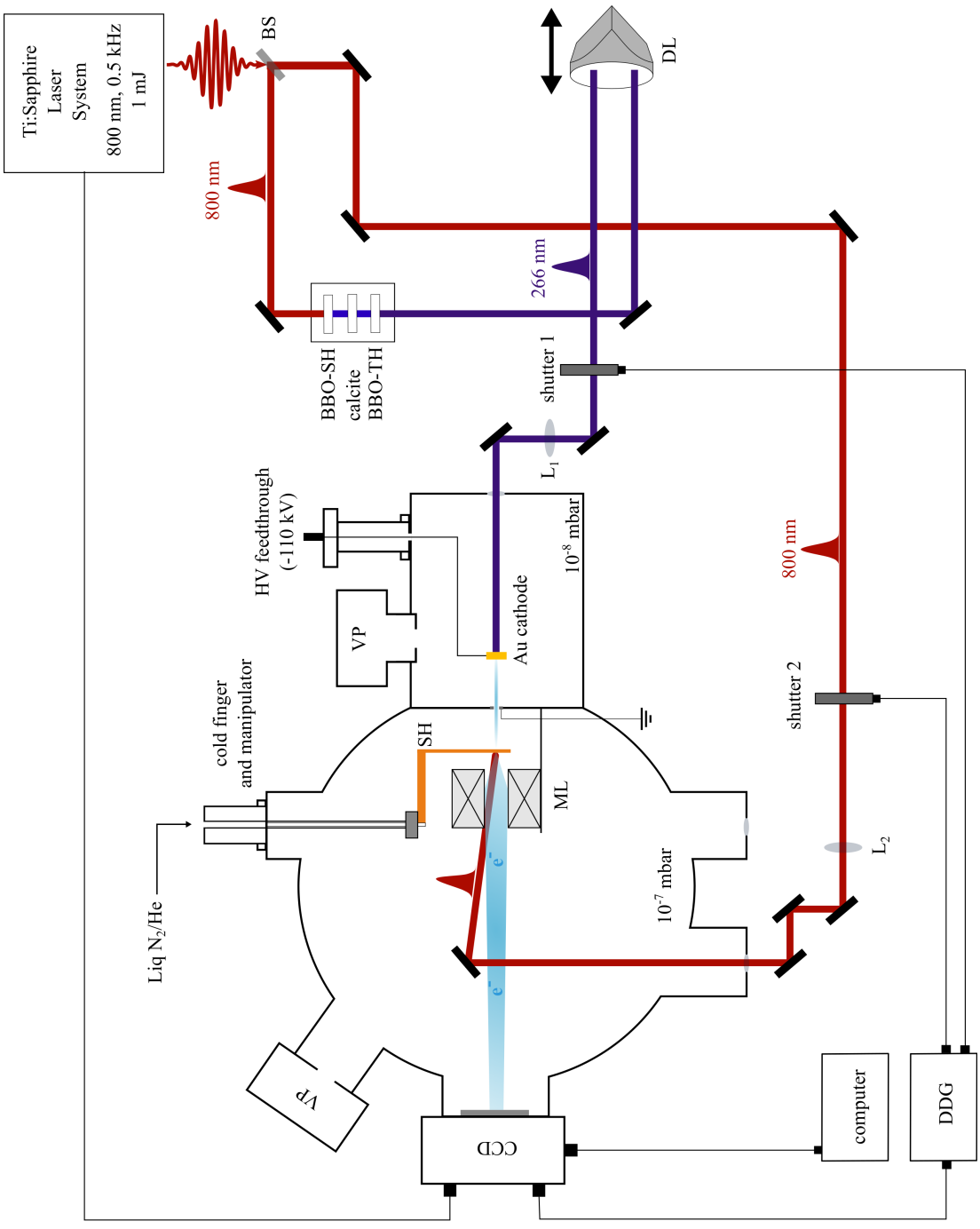

Figure 5.5: The FED Setup. BS: beam-Splitter; VP: vacuum pump; ML: magnetic lens; SH: sample holder; DL: delay line; L1 & 2: lens; DDG: digital delay generator; CCD: charge-coupled-device.

The sample chamber is where the laser and the electron beams interact with the crystalline sample. The crystalline sample is mounted on a TEM mesh (Cu) or a silicon-nitride (SiN) window, depending on the experiment, and placed in the sample holder (SH), made from a copper block (see Fig 5.6) with holes for sample mounting. Once the samples have been mounted, a stainless steel cover is placed on top to secure them. The SH is then attached to a commercial manipulator. The manipulator is a three-axis stage that allows for precise movement (precision = 10 µm, backlash = 50 µm) of the holder in three Cartesian axes (x, y and z). The SH is moved only in x (vertical) and y (horizontal) directions in the lab frame, with the z direction defined as the direction of electron travel. The manipulator also incorporates a cold finger, which offers the possibility to use liquid nitrogen/helium in experiments that require cryo-cooling (4-77 K). Alternatively, a Peltier element attached directly to SH, can be used to cool the holder down to $-50\,^{\circ}$C. A proportional-integral-derivative (PID) controller is used to control the temperature of the SH and hence the mounted samples. A platinum wire makes a direct contact with the holder and when the temperature changes, the resistance of the wire changes also. The PID calculates the difference between the user set temperature and the actual temperature of the holder and applies corrections accordingly. Further down is a solenoid magnetic lens (ML) used for focusing the electron beam onto the detector. It sits on two stainless steel bars, providing good thermal contact. The lens is made from winding a copper wire (2000 turns) and passing current through the wires. The chamber is pumped by an Edwards vacuum pump, backed by a scroll pump (Edwards). Pressure in the chamber is maintained at 10^{-7}mbar. The chamber also houses laser beam optics, such as the turning mirrors, used to direct the pump beam at the sample position. Furthermore, to measure the current of the electron beam, a Faraday cup (not shown in Fig 5.5) is used. The cup is attached to a manual movable stage for correct positioning in front of the detector. For measurement of the beam current, the sample holder is moved completely out of the path of the electron beam and the current is measured with an ammeter connected to the cup.

The detection unit consists of a Phosphor screen and a fibre-optical taper coupled to a CCD camera. The Phosphor used in the setup is a P43, which has high conversion (electron to photon) efficiencies, but long fluorescence decay times (approximately 1 ms to decay to 10 %) and the camera consists of 2048 × 2048 pixelated array with the pixel size of 25 µm. Electrons impinging on the phosphor screen are converted into light flashes, which are imaged onto the CCD camera with minimum loses by the optical taper. The complete detection assembly is connected to the end of the sample chamber by a Conflat (CF) flange. The CCD is coated with a 100 nm thick layer of aluminium to minimise detection of scattered/stray background light from the laser. To prevent saturating the detector, the main beam is blocked by a thin piece of aluminum placed in front of the camera.

In order to generate photoelectrons, laser beam is required as mentioned already. Electrons are emitted from the cathode via the photoelectric effect. This requires that the laser wavelength closely matches the work function of the cathode. The work function is defined as the minimum amount of energy an electron needs to escape from a metal surface. The application of the external electric field results in the reduction of the photoemission barrier and hence lowering of the work function. This is known as the Schottky effect [147]. The effective work function is given by

$$\begin{aligned} \phi_{\text{eff}} &= \phi_{\text{w}} - \phi_{\text{Schottky}} \\ &= \phi_{\text{w}} - e\sqrt{\frac{eF_a}{4\pi\varepsilon_0}} \end{aligned} \tag{5.15}$$

where ϕ_{w} is the work function, F_a is the applied field and e is the electron charge. For the case of Gold photocathode at 110 kV, the effective work function (ϕ_{eff} = 4.72 eV, using the value of ϕ_{w} from [148]) is in the range of the 266 nm laser beam photon energy (4.69 eV), which is easily generated by tripling the fundamental output of the Ti:Sa amplifier (800 nm). As with the optical pump-probe setup, the probe beam path is varied, so the laser beam for electron generation is made to travel through the delay line. The beam enters the electron gun cham-

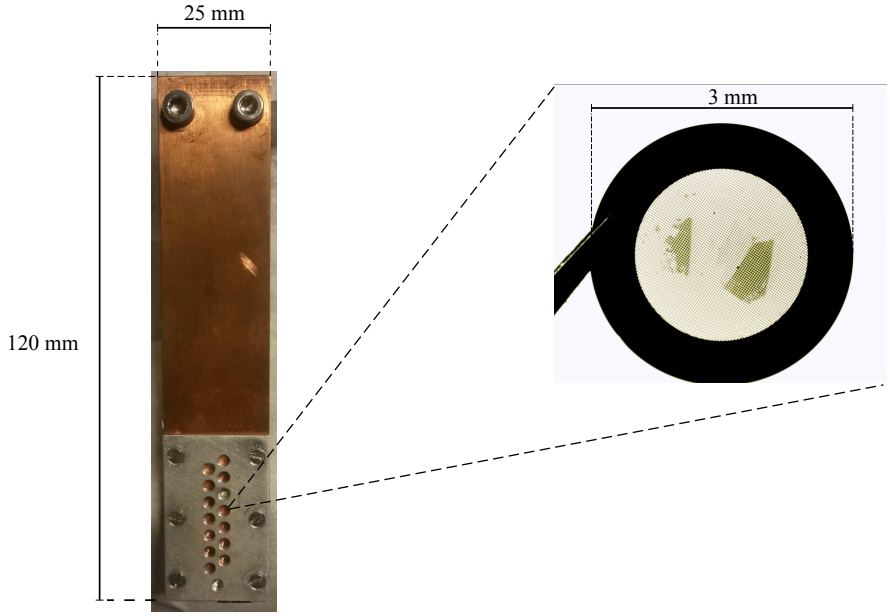

Figure 5.6: The sample holder used in the FED experiments. A magnified optical microscope picture of the TEM mesh with the sample is shown.

ber through a rear window (fused silica). Two turning mirrors, that form part of a periscope assembly, direct the beam inside and are also used for alignment. A lens (L_1, focal length = 500 mm) is placed outside the chamber to focus the beam at the photocathode. The cathode is thus back-illuminated. The intensity of the laser beam is controlled by turning the ND filter wheel placed before the periscope. Very high intensities result in high beam currents and consequently strong space-charge effects and should be avoided. Typical 266 nm pulse energy used is 0.5 µJ. Electrons are photoemitted from the cathode and accelerated by the static electric field gradient, towards the anode. The electrons escape the gun chamber and enter the sample chamber through the pinhole and interact with the solid state sample approximately 1 cm downstream. Most of the electrons pass the sample unscattered, but a small fraction that is scattered is focused by the ML onto the detector, which then sends the data to the computer for processing.

In the pump-probe experiments, shutters are used to control the pump and probe sequences. The time-resolved changes are monitored by recording diffrac-

tion patterns of the sample a delay, Δt after it has been pumped (pump+probe image) and of the unpumped sample (probe only image). Subtracting the two images yields a difference pattern with absolute changes at a particular time delay. At negative time delays (probe arrives at sample before pump), signals are not expected. However, if the specimen under investigation does not relax back thermally before the next sequence or gets damaged by the pump, signals might be observed before time-zero is reached. In case of sample heating, all of the peaks go down in intensity due to the Debye-Waller effect mentioned above. A sign of a structure change is when some peaks go up in intensity and some go down. It must be kept in mind that, due to Freidel's law, the peaks forming the Friedel pair must follow the same trend (if one goes down, the other should also go down in intensity and vice versa).

An important parameter concerned with femtosecond electron diffraction is the coherence length. Coherence is the property that determines whether diffraction from molecules in a crystal is discernible or not. When two waves maintain a degree of phase relationship, they are said to be coherent with one another and the distance in which they remain in phase is known as the coherence length. One distinguishes between longitudinal and transverse coherence of the electron beam. The longitudinal coherence length, L_z is coherence length in the direction of propagation and can be on the order of few tens of nanometers. Transverse coherence length, L_x, on the other hand, is defined as the coherence of the electrons in the direction perpendicular to the propagation of the beam and is more critical for appearance of diffraction. In order to observe diffraction, the transverse coherence length at the sample position must be larger than the unit cell dimensions of the crystal being used in the experiment [149]. This is because only such scatterers that lie within the coherence volume of the electron packets can contribute to the contrast of a diffraction pattern. If the coherence length is comparable to the unit cell length, the diffraction peaks start to overlap. The transverse coherence length is given by [33]

$$L_x \approx \frac{\hbar}{\sigma_{px}} \tag{5.16}$$

where $\hbar = \frac{h}{2\pi}$ is the reduced Planck's constant and σ_{px} is the momentum spread of the electron beam. For typical parameters used in our electron diffraction setups, the transverse coherence length is on the order of a 1-3 nm nanometers, which is sufficient for studying small molecular systems (with cell length of a few tens of Å), but not proteins which form crystals with unit cell lengths of 5-10 nm. Improvements to the coherence length can be made, for instance, by using small spot sizes at the cathode for electron generation or by minimising the mismatch between the wavelength of light and the work function of the cathode (thereby reducing the energy spread). Other ways include replacing the cathodes with tips to reduce the angular spread, but discussion of this goes beyond the scope of this thesis and the reader is referred to the following articles for more details: [149, 150] .

Another important parameter (which can be set easily by the user) is that of sample thickness. With electron energies used in our experiments (80-130 kV), too thick a sample ($>$ 250 nm) will not transmit electrons and too thin ($<$ 50 nm for an organic crystal) would result in weak diffraction. A compromise is sought, but a few aspects need to be considered; the thickness should not exceed that which would lead to multiple scattering. All of what has been discussed so far assumed that electron is scattered only once as it interacts with the sample. This is the basis of the kinematic theory of diffraction. Multiple scattering is certainly possible, but must be avoided, if possible, as treating multiple scattering events can be very complicated and requires invoking dynamical theory of diffraction, which is much more involved than the kinematic theory. A useful figure which can help decide what thickness to use in order to remain in the kinematic regime, is the electron elastic mean free-path, which is defined as the average distance an

electron travels before being scattered and is given by

$$\Lambda_{\text{elastic}} = \frac{1}{n\sigma_{\text{elastic}}} \tag{5.17}$$

where n is the number density and σ_{elastic} is the electron elastic scattering cross-section. Lets calculate it for Spirooxazine crystals. The crystal density is known from literature to be $\rho = 1217.59$ kg m^{-3}. As the molecule is organic and made up of mainly carbon atoms with only a single oxygen, one nitrogen and few hydrogens, we can treat it as if it were made up of only carbon atoms. The total electron elastic cross-section for carbon at 100 keV is 8.8×10^{-19}cm^2 [151]. Using Eq 5.17, this gives the mean free-path of 200 nm. Therefore, the crystal thickness should not exceed 200 nm in order to remain in the elastic scattering regime.

5.5.1 Camera length calibration

Calibration of the camera length, L_{cam} is one of the most common experimental procedures performed in electron diffractometers and microscopes, but also an important one. Camera length is defined as the distance between the sample plane and the centre of the detector (see Fig 5.7). For a fixed magnification, the camera length is also fixed. Without any imaging system, i.e. lenses after the sample, the camera length can be measured simply by using a ruler. However precise calibration of the camera length is normally required as it allows for faithful indexing of the diffraction patterns. Factors that can affect the camera length are temperature of the sample holder or tilt. It should be pointed out that changing the settings of the magnetic lens and hence the magnification will also lead to a change in the camera length. Therefore, it is quite common to calibrate L_{cam} for a number of magnifications. From Fig 5.7 the following geometric relationship between the Bragg angle and the camera length can established

$$L_{\text{cam}} = \frac{r_{\text{pix}}}{\tan 2\theta} \tag{5.18}$$

where r_{pix} is the distance of a Bragg peak from the centre of the detector. Recall that the Bragg angle is given by $\theta_{\text{bragg}} = \sin^{-1} \dfrac{\lambda_{\text{elec}}}{2d_{hkl}}$, where d_{hkl} is the interplanar

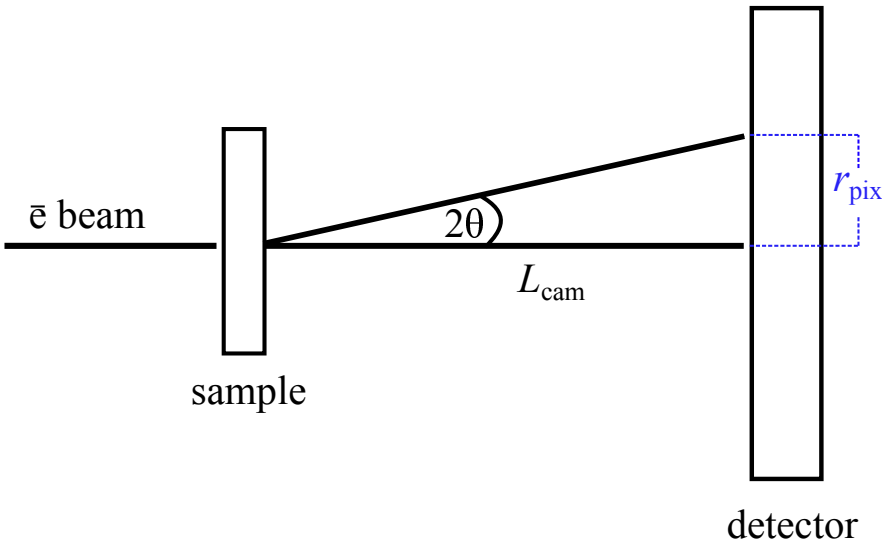

Figure 5.7: The definition of camera length.

distance between planes of indices (h k l) and λ_{elec} is the electron wavelength, which can be calculated using Eq 5.5 (0.0351 Å for 100 kV). Inserting, θ_{bragg} in Eq 5.18 gives the following expression that can be used to calculate L_{cam}

$$L_{cam} = \frac{r_{pix}}{\tan 2\left(\sin^{-1}\frac{\lambda_{elec}}{d_{hkl}}\right)} \tag{5.19}$$

The following procedure for camera length calibration was followed. The diffraction pattern of a standard sample with known lattice spacing, d_{hkl} was measured at a fixed magnification. A free-standing film of polycrystalline gold (Au) was used for this purpose. A gold crystal has a face-centre cubic (fcc) unit cell with a lattice constant of $\mathbf{a}$ = 4.08 Å [152]. After recording the image, a radial average[4] of the pattern was computed and the peaks were indexed (see Fig 5.8) by comparing the measured diffraction pattern with a one simulated using the CrystalDiffract software [153]. The expression for d_{hkl} for a fcc crystal is

$$d_{hkl} = \frac{\mathbf{a}}{\sqrt{h^2 + k^2 + l^2}} \tag{5.20}$$

where $\mathbf{a}$ is the lattice constant and h, k, l are the Miller indices of the allowed reflections, which must be all odd or all even for a fcc lattice, according to crys-

[4]azimuthal integration at a fixed distance from the image centre.

	hkl	r_{pix}/pixels	L_{cam}/mm
a	111	75	251.30
b	200	86	249.54
c	220	122	250.29
d	311	143	250.17
e	331	189	251.52
f	422	209	247.44

Table 5.1: Calculated values of camera length using a magnetic lens current of 0.98 Amperes and acceleration voltage of 110 kV (0.0351 Å).

tallographic rules. The camera lengths were calculated for peaks identified in Fig 5.8 and are tabulated in Table 5.1. The radii in pixels were converted to metric units. The image was binned 2×2 during collection, giving the effective pixel size of 50 µm. The camera length was found to be 250.04 mm.

5.5.2 Spatial overlap and time-zero

As has been mentioned before that in order for observe a time-resolved signal, it is essential that the pump and the probe beams are spatially overlapped at the sample position. Ideally, the electron beam should be within the width of the pumped volume, so that it probes areas that are homogeneously excited. Therefore, a pump size of about 2 or 2.5 times larger than the probe is desirable. The electron beam size can only be changed in our setup by changing the pinhole on the anode plate, which is a tedious operation. The pump beam size at the sample, on the other hand, can be changed simply by varying the position of the lens used to focus it, so it is this that is adjusted instead. The beam size measurement and spatial overlap are carried out simultaneously. A small aperture with the hole diameter of 50 µm is placed in one of the slots in the sample holder and is scanned over the electron and laser beam profiles in x and y directions. The transmitted beam intensities are measured by either the CCD camera (electron beam)

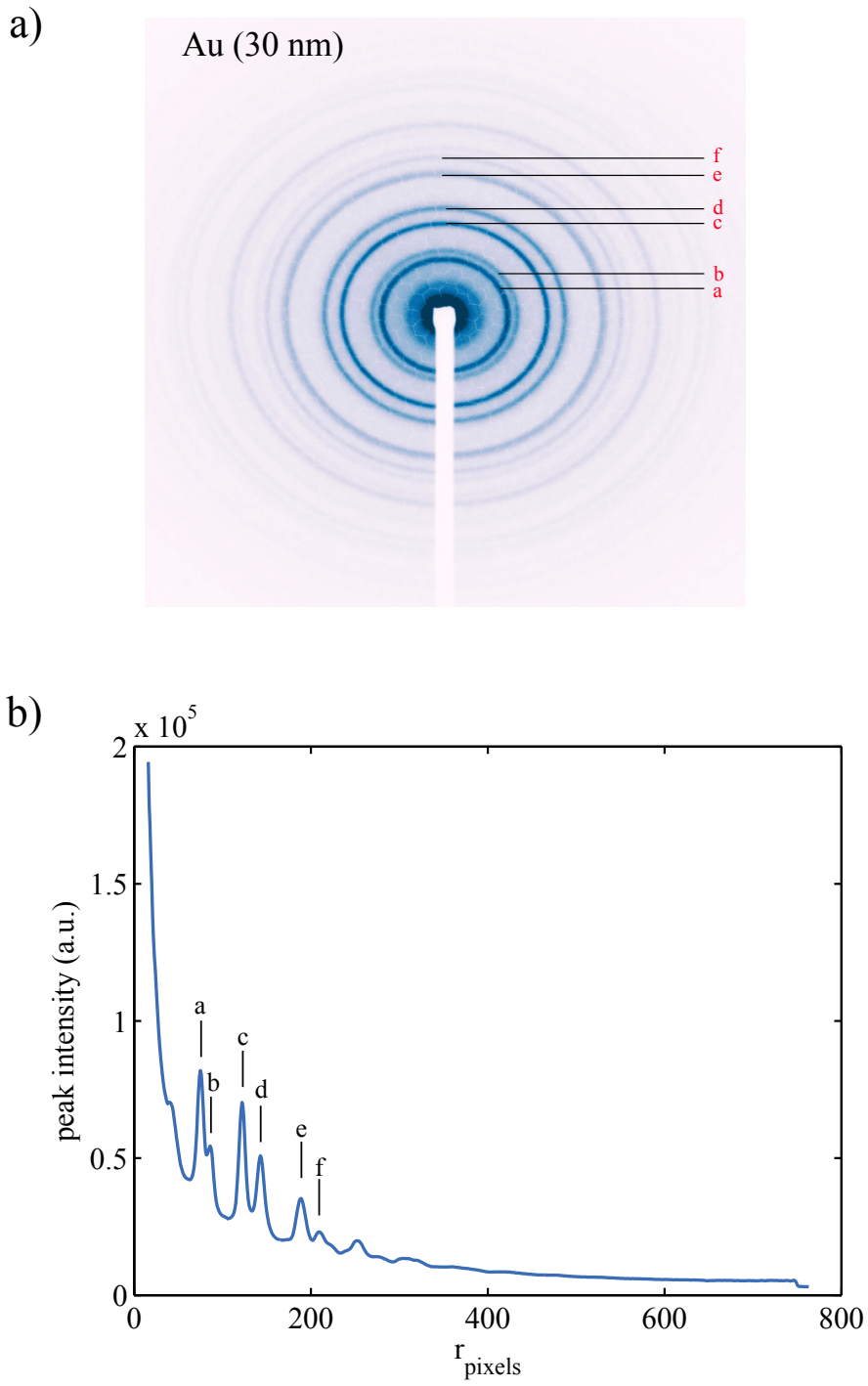

Figure 5.8: a). Diffraction patten of polycrystalline gold film (30 nm thick) measured with 110 kV electrons b). The radial integration of the diffraction pattern.

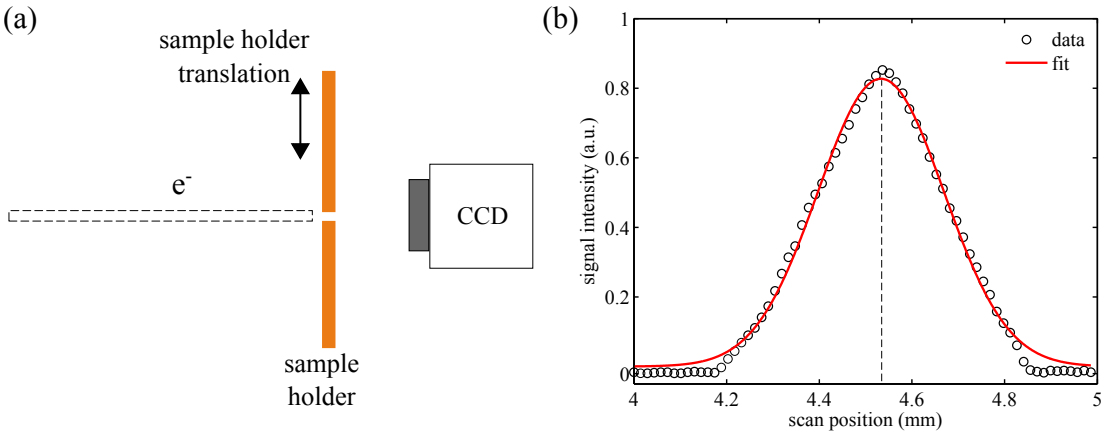

Figure 5.9: a) A schematic of beam scanning measurement and b) an example of measured intensity distribution.

or a CMOS camera (laser beam) looking in the chamber from the side window. The intensity distributions resulting from the beam scans (see Fig 5.9) are fitted with a Gaussian function to yield the mean and standard deviation, taken as the coordinate(s) for sample position and FWHM beam size (after multiplying by a factor), respectively.

For determination of time-zero, once more a free-standing polycrystalline gold film (30 nm) was used. 800 nm laser beam (7 mJ cm^{-2}) was used to pump the gold sample and the response was measured with the electron probe. The difference images from the experiment are shown in Fig 5.10. The drop in the intensity of the rings is due to the increase of the lattice temperature and hence the Debye-Waller factors. The zero-time determined in this way was accurate to within 0.5-1 ps. This gives a good starting point for its refinement, which must be performed using the actual sample (if possible) that one wishes to investigate, as translating the sample holder may cause a shift in time-zero due to tilt or simply by the change of location.

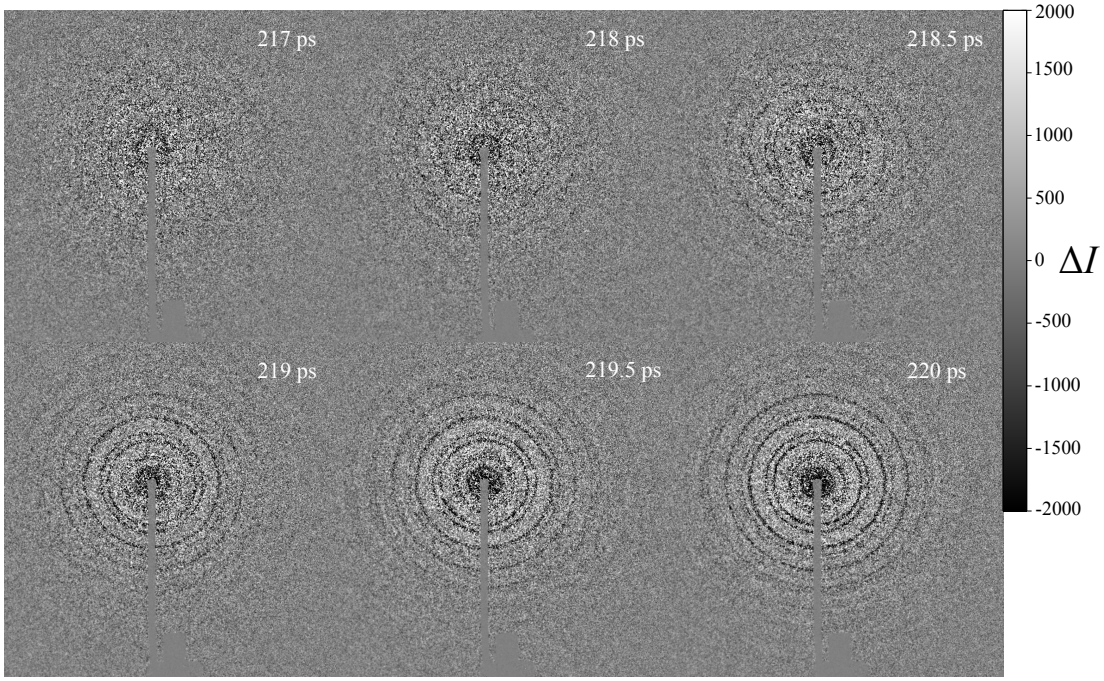

Figure 5.10: The time-zero determination using Gold film (30 nm)excited by 800 nm laser beam. The time delays refer to the delay on the translational stage.

Chapter 6

Femtosecond Electron Diffraction of EDO-MeEDO

This chapter reports on the ongoing efforts to investigate properties of an organic salt, EDO-MeEDO using static and time-resolved electron diffraction. This chapter will set out to describe the experiments that have been performed to date and present results and the current state of understanding on the system.

6.1 A short background

Molecular organic crystals have attracted a lot of interest due to their scope for technological applications, such as in molecular electronics [154] and as potential light harvesters [155]. They have also become a target of many researchers, amongst them synthetic chemists, wishing to functionalise them to build new materials (a field of material design) and on the other hand, condensed matter physicists wishing to understand the many exotic features (such as superconductivity [156, 157]) associated with some of these systems.

A particularly interesting class of organic crystals are the quasi-one-dimensional crystals which can be fabricated by packing planar, conjugated molecules together into stacks. The overlap of the π-orbitals between molecules along the stack results in one-dimensional electron transport, which not only makes them conduct-

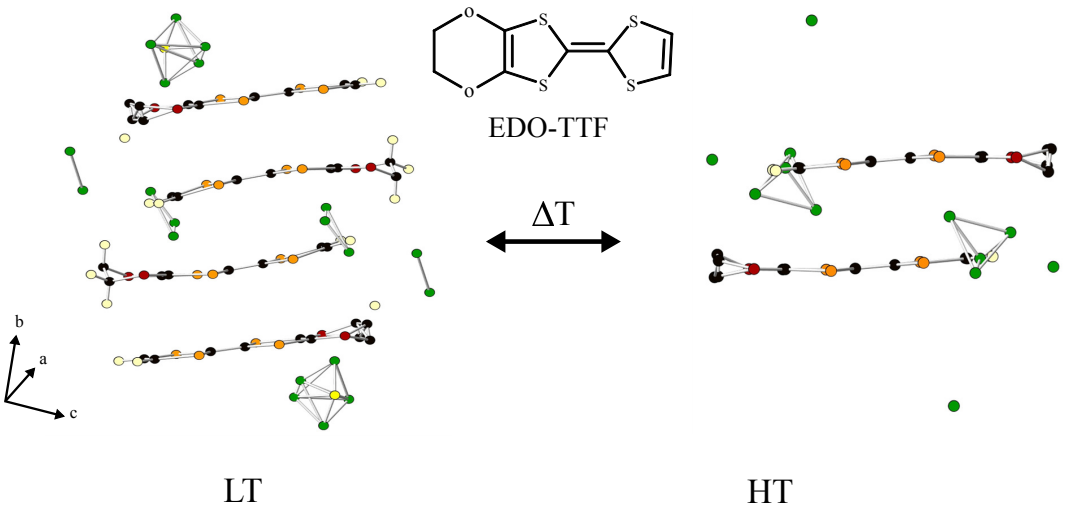

Figure 6.1: Schematic of phase transition in $(EDO{-}TTF)_2PF_6$. The b-axis almost doubles at 280 K (LT) due to Pierels distortion.

ing, but also gives rise to strong electron correlations. Conversely, the interstack π-orbital overlap is weaker [158]. Strong correlations and crystal flexibility (due to the relatively weak intermolecular forces binding the 1D chains) lead to interplay between electrons and the lattice vibrations (phonons) and therefore these materials exhibit complicated electronic structures, complex phenomena and phase diagrams [159]. Owing to the strong electron-electron and electron-lattice interactions, they are also known as strongly correlated electron-lattice systems.

A system that is relevant to this work is 4,5-ethylenedioxytetrathiafulvalene (EDO-TTF, Fig 6.1), whose complex with the PF_6 anion, $(EDO{-}TTF)_2PF_6$ has been studied extensively in the last decade by various ultrafast techniques, such as femtosecond mid-infrared and infrared spectroscopies and femtosecond electron diffraction [160–164]. In this charge transfer complex, EDO-TTF molecules act as electron donors and form alternating head/tail stacks. From x-ray diffraction and vibrational spectroscopy, it was determined that at room temperature the charge distributes equally at each site in the complex and that all donor molecules are planar. Furthermore, electrical conductivity measurements showed that this complex had metallic character at room temperature. As the temperature was

lowered, however, the resistivity increased and the complex became an insulator. The change is referred to as a metal-to-insulator phase transition and occurs at a temperature of 280 K. The insulating phase is brought about by a large structural change based on the molecular deformation of EDO-TTF. Structural analysis of $(EDO{-}TTF)_2PF_6$ crystals at 280 K showed that two EDO-TTF moieties bend towards each other and together with other two EDO-TTF molecules, which retain their planarity, form a tetramer (see Fig 6.1) leading to doubling of the unit cell caused by Peierls distortion [165]. This is manifested in appearance of new peaks (known as superlattice reflections) in the diffraction pattern that emerge between rows of Bragg peaks seen at 298 K. Vibrational spectroscopy also revealed that in the insulating phase, the charges are no longer uniformly distributed between sites, instead a clear ordering of charge, (0110) where neutral = 0 and cationic = 1, was observed which implies that charge ordering instability also facilitates the phase transition. Aside from the thermal phase transition, EDO-TTF also undergoes a highly efficient photoinduced phase transition (PIPT) from low temperature phase, which make it a promising candidate for ultrafast switching applications.

Recently, an attempt was successfully made to dope $(EDO{-}TTF)_2PF_6$ with the intention to tune its properties by adding 'impurities' to the original salt [166]. Our collaborators at Tokyo Institute of Technology, Japan have undertaken the task to study the ultrafast dynamics of this system using infrared spectroscopy and we aim to perform time-resolved electron diffraction experiments to investigate how the doping affects the physics of phase transition in this material.

6.2 Introducing the system

The system under investigation is a complex consisting of a mixture of two different organic donor molecules namely 4,5-ethylenedioxy-4'-methyltetrathiafulvalene, MeEDO-TTF and EDO-TTF (see Fig 6.2). The general formula of the salt is $[(EDO{-}TTF)_{1\text{-}x}(MeEDO{-}TTF)_x]_2PF_6$, where x is the mole fraction of MeEDO-

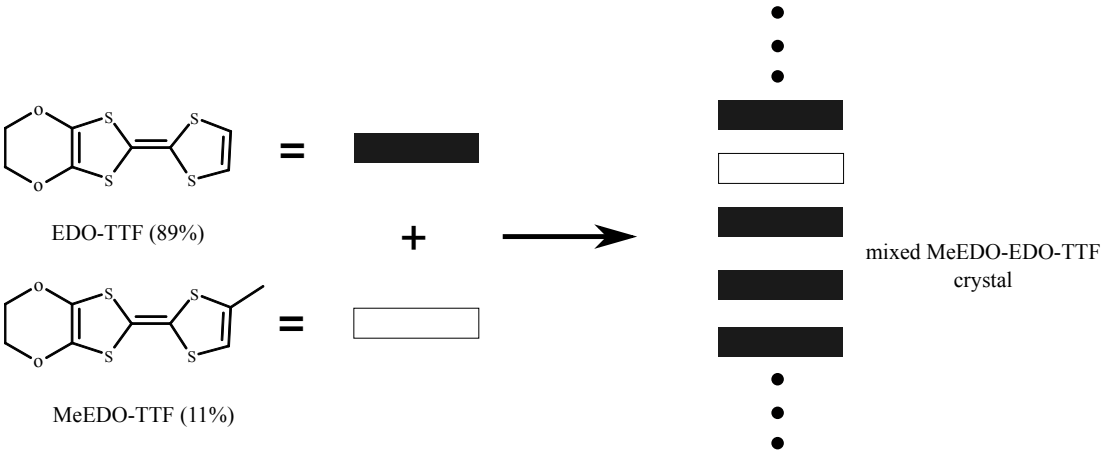

Figure 6.2: Schemeatic of EDO-TTF mixed crystal. Each MeEDO-TTF molecule will replace one in 10 EDO-TTF molecule along the stack.

TTF donor molecule. For simplicity, the system will be referred to as EDO-MeEDO henceforth. The properties of the salt were studied by Murata *et al*, who first synthesised the mixed complex using different ratios of EDO-TTF and MeEDO-TTF [166]. The authors characterised the resulting alloys by x-ray diffraction, electrical conductivity measurements and Raman spectroscopy. They reported that the incorporation of MeEDO-TTF into $(EDO{-}TTF)_2PF_6$ suppressed all the main phase transition mechanisms that were present in $(EDO{-}TTF)_2PF_6$. Especially, the charge ordering feature was strongly suppressed as x increased and seemed to disappear in the x = 0.13 alloy. The results of electrical conductivities on the alloys as measured by the authors are shown in Fig 6.3. As can be seen from the resistivity curves, at small x values, there is a sudden jump in resistivity towards higher values as the temperature is lowered, corresponding to the initially conducting phase undergoing a first-order phase transition [1] to an insulating state. This behaviour is also found in $(EDO{-}TTF)_2PF_6$ crystals. The arrows in the figure mark the temperatures at which the phase transitions occur. When mole fraction is x = 0.13, the resistance change is no longer abrupt,

[1] First-order phase transition is one in which the first derivative of the free energy with respect to the order parameter, i.e. temperature, conductivity, magnetic susceptibility is discontinuous.

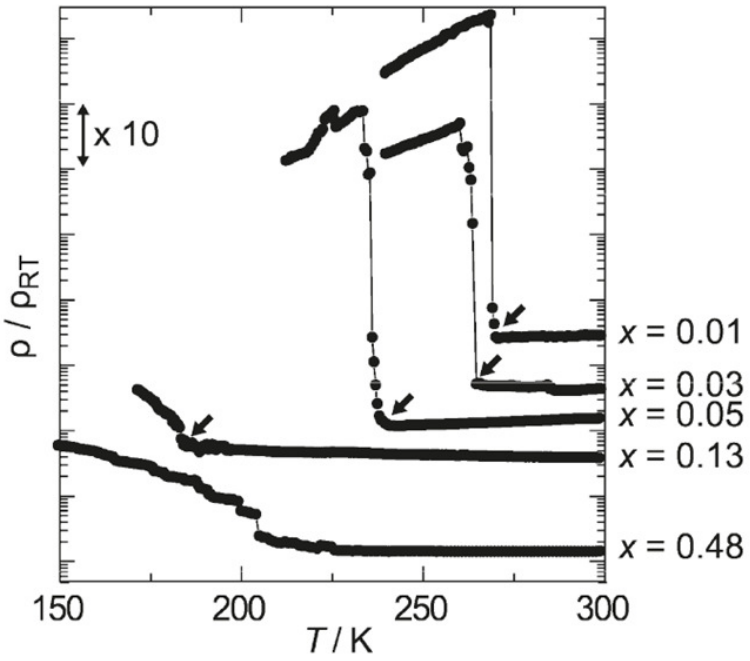

Figure 6.3: Resistivity curves for EDO-MeEDO crystals with a range of x values as a function of temperature. When x = 0.01-0.05, the case is identical to $(EDO{-}TTF)_2PF_6$ crystals. Figure taken from [166].

but instead gradual (second-order phase transition) and the critical temperature is shifted to lower values when compared to EDO-TTF (with x = 0.01). The authors also measured the temperature dependence on the x-ray diffraction patterns of these EDO-MeEDO crystals and used direct methods to solve the crystal structures. They found that the EDO-TTF rich alloys (x < 0.5) were isostructural with pristine $(EDO{-}TTF)_2PF_6$ and when x > 0.5, MeEDO-TTF molecules incorporate randomly in the stacking column, leading to an extension of the lattice constants and elongation of donor-anion distance, which the authors concluded was responsible for different physical properties of the complexes when compared to the EDO-TTF rich alloys (x < 0.5). The unit cell parameters for $[(EDO{-}TTF)_{1-x}(MeEDO{-}TTF)_x]_2PF_6$, where x = 0.13, as determined by the authors are reported in Table 6.1. As the table shows, going from high temperature (HT) to low temperature (LT), the unit cell parameters change. The most notable change is in the formula number Z, which denotes the number of chem-

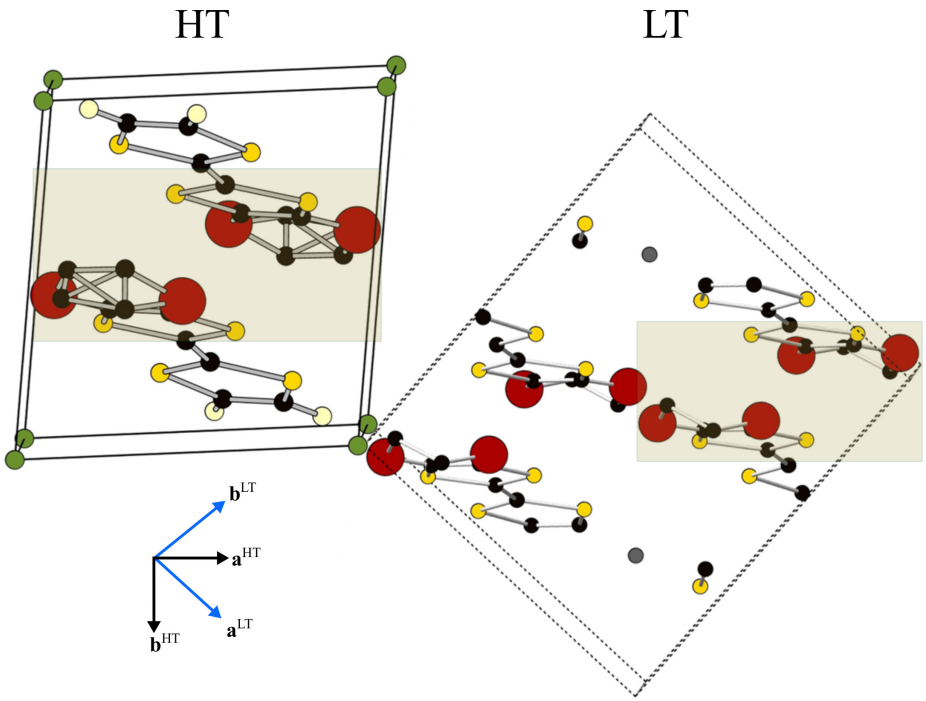

Figure 6.4: 3D models of the crystal structure at HT and LT and the relationship between them. Notice that by tilting the LT cell clockwise, the orientation of molecules in both cells is identical.

ical units per unit cell and which was found to be doubled at LT. The volume at LT also is twice that of the volume at HT. The 3D models of the crystal at the two temperatures were inspected using software suite CrystalMaker [167] and are shown in Fig 6.4. The red balls denote the oxygen atoms, yellow ones denote sulphurs, black represent carbons and green corresponds to phosphorous of the PF_6 counter anion. Some of the atoms have been removed from the models for clarity. It can be seen that at HT, there are only two molecules per unit cell (each EDO-TTF molecule has two oxygen atoms), while at LT there are a total of four. Furthermore, in order to compare the two cells, the LT model has to be titled clockwise with respect to the HT origin, so that direction in which they are viewed is the same. This suggest that different unit cell bases were used by the authors in order to construct the structures and for a more meaningful comparison of the LT and HT structures, both unit cells need to be re-defined into a

	HT (300 K)	LT (150 K)
a (Å)	7.21	9.55
b (Å)	7.35	10.82
c (Å)	12.02	11.95
α (deg)	93.61	101.84
β (deg)	75.37	99.19
γ (deg)	97.11	90.42
V (Å^3)	611.8	1191.7
Z	1	2

Table 6.1: Muratas definition of unit cell parameters

common basis.

6.2.1 Unit cell basis transformation

The relationship between two unit cells axis vectors is drawn in the Fig 6.4. The c-axis in the HT and LT phases have near identical lengths (see Table 6.1), but opposite directions. Based on this, the following transformation was carried out

$$\begin{aligned}
\mathbf{a}^{\mathrm{HTnew}} &= \mathbf{a}^{\mathrm{HT}} + \mathbf{b}^{\mathrm{HT}} \\
\mathbf{b}^{\mathrm{HTnew}} &= \mathbf{b}^{\mathrm{HT}} \\
\mathbf{c}^{\mathrm{HTnew}} &= \mathbf{c}^{\mathrm{HT}} \\
\\
\mathbf{a}^{\mathrm{LTnew}} &= \mathbf{a}^{\mathrm{LT}} \\
\mathbf{b}^{\mathrm{LTnew}} &= \mathbf{a}^{\mathrm{LT}} - \mathbf{b}^{\mathrm{LT}} \\
\mathbf{c}^{\mathrm{LTnew}} &= -\mathbf{c}^{\mathrm{LT}}
\end{aligned} \tag{6.1}$$

In the above, $\mathbf{a}^{\mathrm{HTnew}}$ is obtained by projecting the $\mathbf{a}^{\mathrm{HT}}$ axis onto the $\mathbf{a}^{\mathrm{LT}}$ axis through a vector sum of $\mathbf{a}^{\mathrm{HT}}$ and $\mathbf{b}^{\mathrm{HT}}$. Similarly, $\mathbf{b}^{\mathrm{LTnew}}$ is a result of projection of the $\mathbf{b}^{\mathrm{LT}}$ onto the $\mathbf{b}^{\mathrm{HT}}$ cell axis. Axes $\mathbf{b}^{\mathrm{HTnew}}$, $\mathbf{c}^{\mathrm{HTnew}}$, $\mathbf{a}^{\mathrm{LTnew}}$ are unchanged, but $\mathbf{c}^{\mathrm{LT}}$ direction is reversed, so that all unit cell axes in the new basis have same

	HT (300 K)	LT (150 K)
a (Å)	9.35	9.55
b (Å)	7.35	14.48
c (Å)	12.02	11.95
α (deg)	93.61	92.35
β (deg)	81.91	80.37
γ (deg)	47.92	48.97
V (Å^3)	611.8	1191.7
Z	1	2

Table 6.2: Unit cell parameters after basis transformation.

directions. The new cell parameters after basis transformation are reported in Table 6.2. The procedure for the transformation is the same as that used by the authors in [164] to treat $(EDO{-}TTF)_2PF_6$ crystallographic data. The comparison between the two unit cells can be made more easily now and it follows that there is an elongation of the cell along the b-axis, which is the stacking direction of the donor molecules. The resulting 3D models after basis transformation for the two phases are shown in Fig 6.5.

The experiments described from the next section are aimed at understanding the photoinduced structural dynamics in this complex.

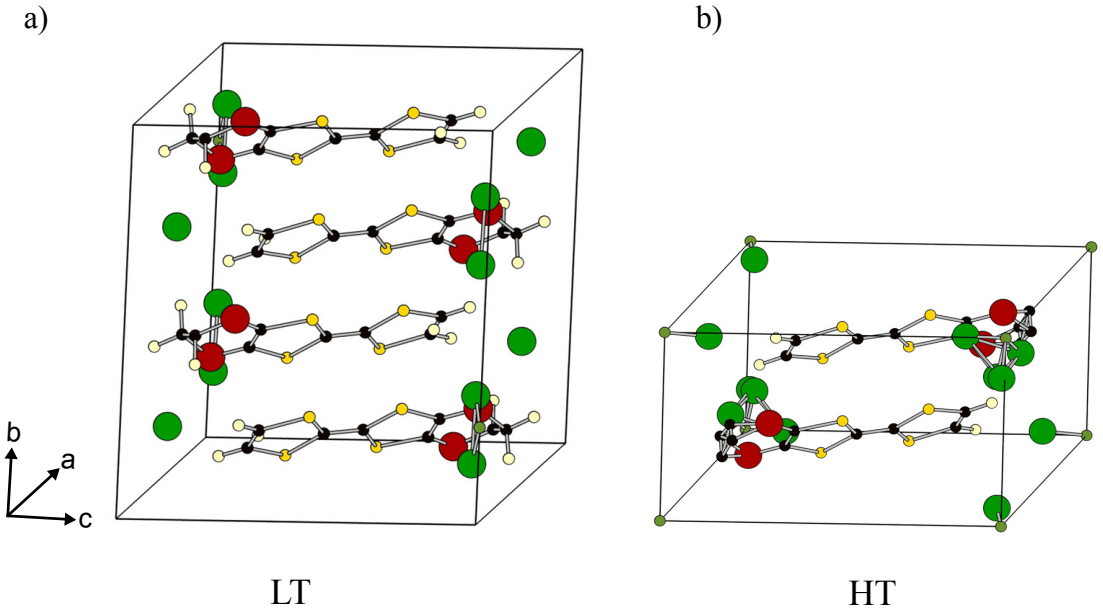

Figure 6.5: 3D models of the HT and LT crystal structure after unit cell transformations to a common basis. The lengthening of the b axis in LT is now clearly seen.

6.3 Experiments

The crystalline samples of EDO-MeEDO (x = 0.11) were supplied by our collaborators in Tokyo Institute of Technology. The crystals were shiny black needles with an approximate area of $2 \times 1\,\mathrm{mm}^2$ and less than 0.5 mm in thickness. These crystals were microtomed parallel to the longest axis (the stacking axis) in 100 nm sections. Diffraction patterns from most microtomed sections showed a strong rotational disorder, seen as pronounced extended tails of the Bragg peaks. The samples that showed the least distortion were selected for experiments.

6.3.1 Temperature dependence

At first, a temperature dependence measurement was carried out using the setup described in the previous chapter in order to look for the signature of the cell doubling transition. The temperature, beginning at 298 K, was lowered in 50 K increments down to 100 K. After each increment, the sample holder was allowed to

first stabilise thermally to compensate for any drifts and then a diffraction image was recorded. Fig 6.6 shows the normalised diffraction patterns resulting from subtraction of images taken at different temperatures. The difference patterns showed shifts in peak positions due to electron beam shift (which can occur due to temperature variation in the magnetic lens and/or laser pointing instability). An attempt was made to correct for the shift by selecting at least four peak pairs and locating their centres in x and y directions, by fitting with a Gaussian function. The distances between the peak centres for each peak pair were computed and the average bisector of the pairs was used as the new image centre. Unfortunately, this did not work very well as some images still showed significant peak shifts, presumably because the sample holder also shifted during acquisition (despite allowing it to come to a steady temperature), which is difficult to estimate and correct. Nevertheless, importantly no new reflections could be observed even when the temperature was at 100 K (well below T_c). Instead, some peak pairs showed sign changes with some going up and some going down in intensity, as would be expected for a structural change (see Fig 6.6).

Another way to see the effect changing the temperature has on the peak intensities is to plot relative intensity changes, normalised to the lowest recorded temperature (100 K). The relative changes in intensity were calculated using the expression below

$$\frac{\Delta I}{I_0} = \frac{I_{\mathrm{T>100K}} - I_{\mathrm{100K}}}{I_{\mathrm{100K}}} \tag{6.2}$$

where $I_{\mathrm{T>100K}}$ are the detector background-corrected intensities of selected peaks from images recorded at temperatures higher than 100 K and I_{100K} correspond to the intensities of the peaks from the image recorded at 100 K. The results for some selected peaks are shown in Fig 6.7. It can be seen from the relative intensity change plots that some peaks go up in intensity while other go in the opposite direction. This confirms the above observation that a structure change did indeed take place after changing the temperature.

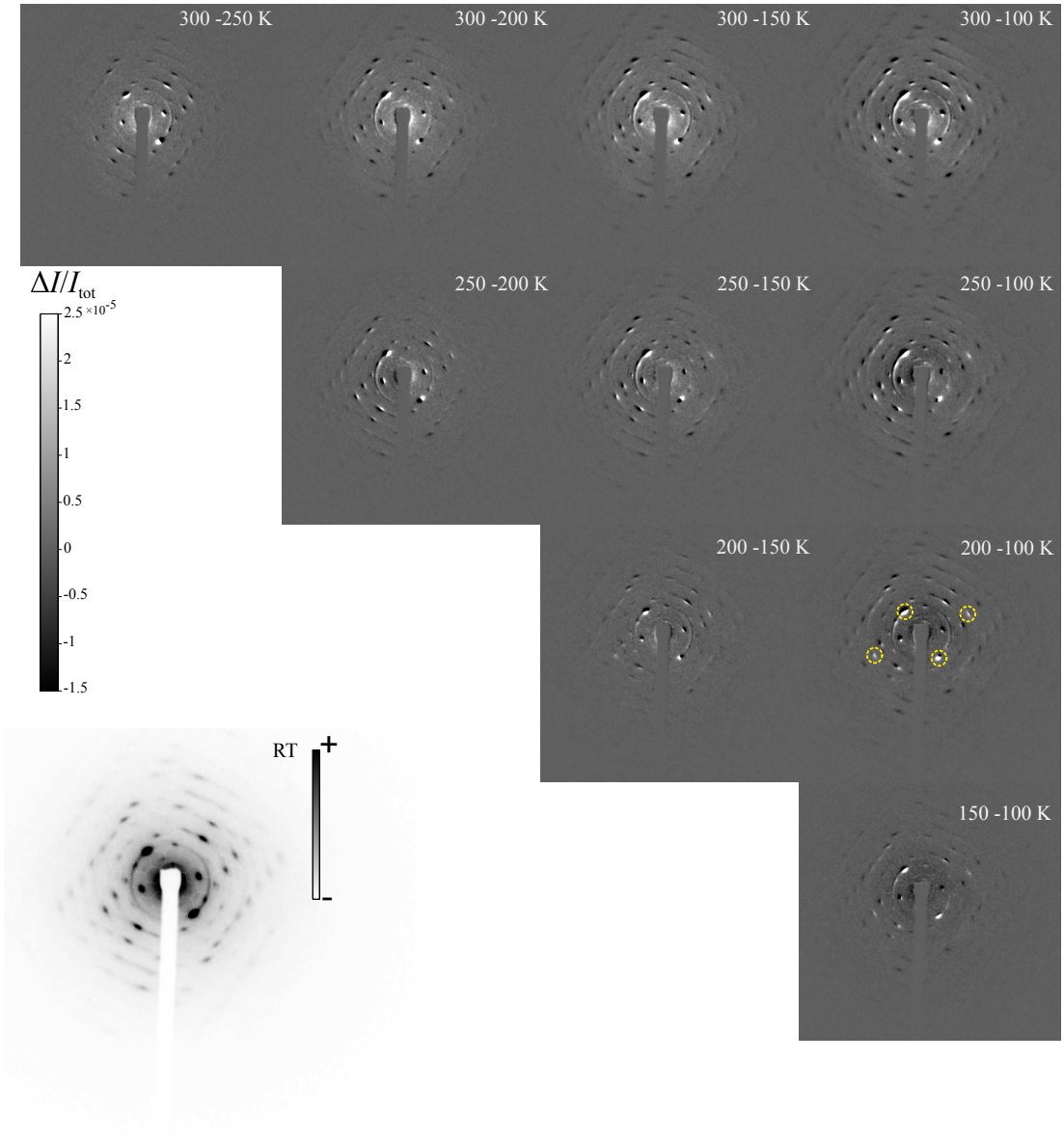

Figure 6.6: Difference images from temperature dependence measurements. Also shown is the room temperature diffraction pattern. Peaks circled show an increase in intensity, while other peaks go down. The shift due to electron beam can also be seen clearly in the most bright peaks.

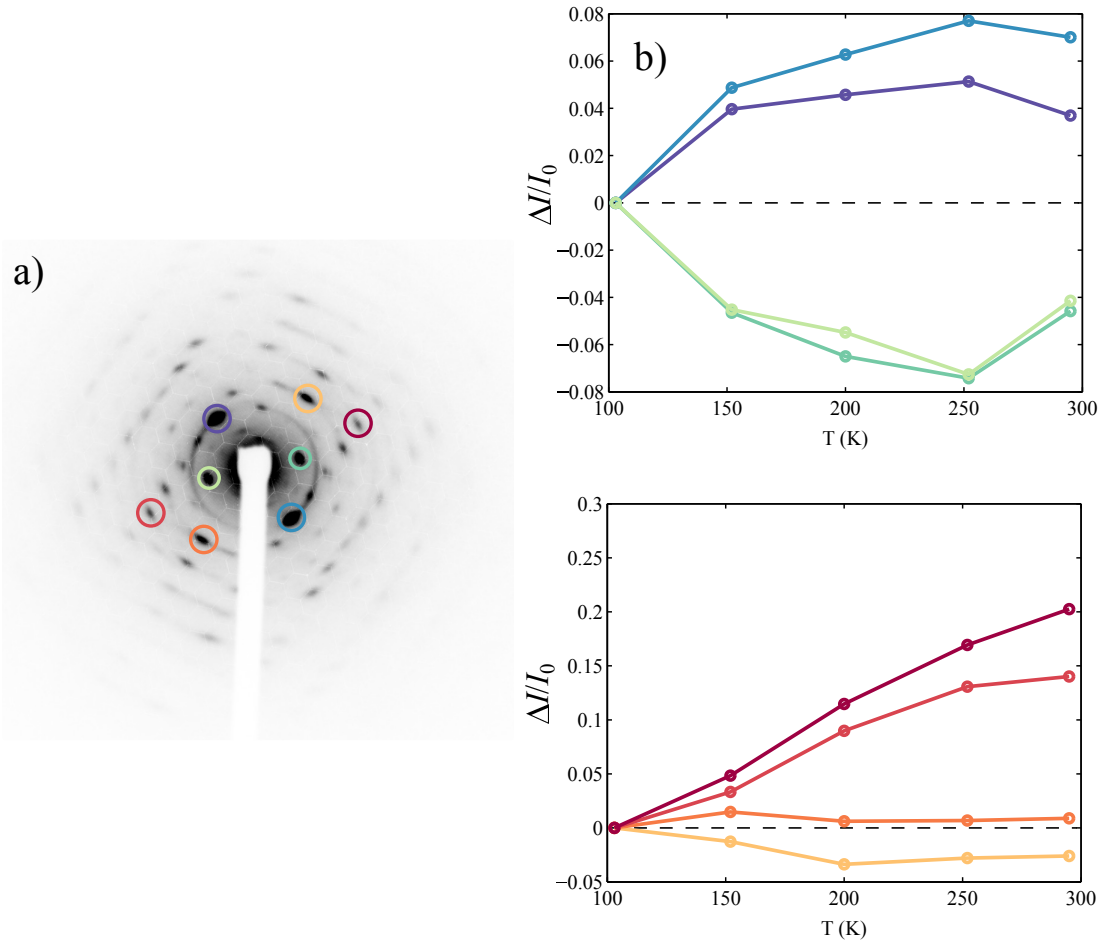

Figure 6.7: The relative intensity change for selected peaks as a function of the temperature. Panel a) shows the diffraction pattern measured at LT.

6.3.2 Time-resolved experiments

Time-resolved experiments were carried out to investigate the effect of photoexcitation on the system held at 100 K. The fundamental output of the Ti:Sa laser (800 nm, 100 Hz) was used to excite the sample, which corresponds to an absorption into a charge-transfer band of EDO-TTF. As the molecules stack along a particular crystal axis, polarisation is an important factor to consider as those molecules whose transition dipole moments are aligned parallel to the electric field vector of the laser will get preferentially excited. Initially, to avoid any polarisation issues, a quarter wave-plate ($\lambda/4$) was installed to change the linearly polarised 800 nm laser beam into circularly polarised light. A perfectly circularly polarised beam contains two linear components (s and p) that are equal in amplitude, but have a phase difference of $\pi/2$ and which rotate the field in a circle around the axis of propagation. The quality of the circularly polarised light can be examined by placing a polariser after the quarter-wave plate and measuring the transmission as the polariser is rotated. If the intensity of the transmitted light remains unchanged then the polarisation state of the beam is perfectly circular. The polarisation of the pump beam was found to be somewhat elliptical (≈ 25 %).

The results of the time-resolved experiments covering the first 100 ps of the dynamics are shown in Fig 6.8. A step-size of 5 ps was used in the measurement and the pump energy was tuned so that the fluence was 2.8 mJ cm^{-2}, giving a number for excitation fraction of about 10 % (OD at 800 nm = 0.3 for 300 nm thick crystal [2]).

The relative intensity changes were calculated using the equation below

$$\frac{\Delta I}{I_0} = \frac{I_{\mathrm{PumpON}} - I_{\mathrm{PumpOFF}}}{I_{\mathrm{PumpOFF}}} \tag{6.3}$$

where I_{PumpON} is the background-subtracted intensity measured in the pump and probe sequence and I_{PumpOFF} corresponds to the intensity measured when the pump was off. Normalisation was performed to account for any changes

[2] Absorption measurements were performed by our collaborators.

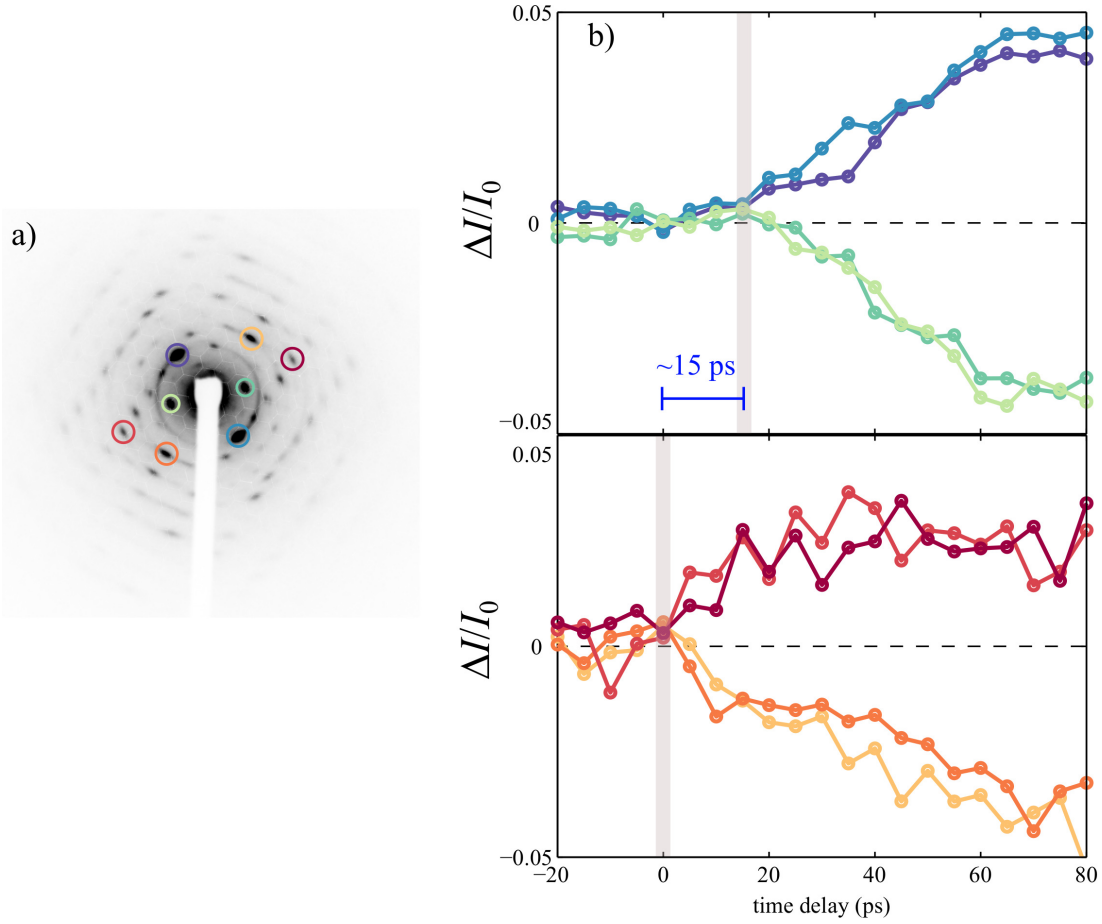

Figure 6.8: Result of a time-resolved scan. The delayed onset of the lower order peaks is clearly seen.

in electron number during the course of the time-resolved scan. Comparisons of the time-resolved plots with the results of temperature dependence measurements shown in Fig 6.7 reveal similar trends for the selected peaks. Indeed, the two measurements agree quite well, at least in terms of the signs of the relative changes. Also, interestingly, very close to the time-zero region, a decay and rise of the signal was witnessed for some higher order peaks (red and orange rings in Fig 6.8a), but not for the most intense Friedel pair, which appear to change after about 15 ps.

The rise in temperature due to laser absorption was also estimated. The

following relation was used [168]

$$\Delta \mathrm{T\,(K)} = \frac{F_{\mathrm{abs}}}{\mathrm{C_v} \times l} \tag{6.4}$$

where F_{abs} is the absorbed fluence given in the units of J cm^{-2}, $\mathrm{C_v}$ is the volumetric heat capacity with units J K^{-1}cm^{-3} and l is the crystal thickness in cm. For the present case, $\rho\,(100\,\mathrm{K}) = 1.88\,\mathrm{g\ cm^{-3}}$, $\mathrm{C_{molar}} = 575\,\mathrm{J\ K^{-1}mol^{-1}}$ and $\mathrm{M_r} = 673.35\,\mathrm{g\ mol^{-1}}$. This gave a value of about 87 K for the temperature rise.

Additionally, an experiment was performed in which the complete range afforded by the translational delay stage (approximately 1.5 ns) was covered. The results of the measurement are presented in Fig 6.9 for the same peaks as those plotted previously. Strong oscillations with a period of nearly 200 ps are clearly observed. The oscillations become increasingly damped as time progresses and after about 1 ns, they are completely washed out.

Finally, it was mentioned above that molecules stacked in a particular direction in the crystal should show a dependence for pump beam polarisation. Therefore, a measurement was conducted to confirm this. Different polarisation states of the laser were generated by replacing the quarter-wave plate with a half-wave plate, which rotates the plane of polarisation of the laser beam by twice the angle the beam makes with the fast axis of the plate. For each polarisation angle, a time-resolved scan was run covering the first 100 ps. The images corresponding to the last time-point of the scan, with different polarisation angles, are shown in Fig 6.10. The most intense peak was selected for examination and relative intensity changes were plotted as a function of the polarisation angle (θ_{pol}) as displayed in Fig 6.11. The error bars were calculated by taking the standard error of the mean as follows

$$s = \frac{\sigma}{\sqrt{n}} \tag{6.5}$$

where σ is the sample standard deviation and n is the sample size. The standard deviation, σ was calculated by using the following formula

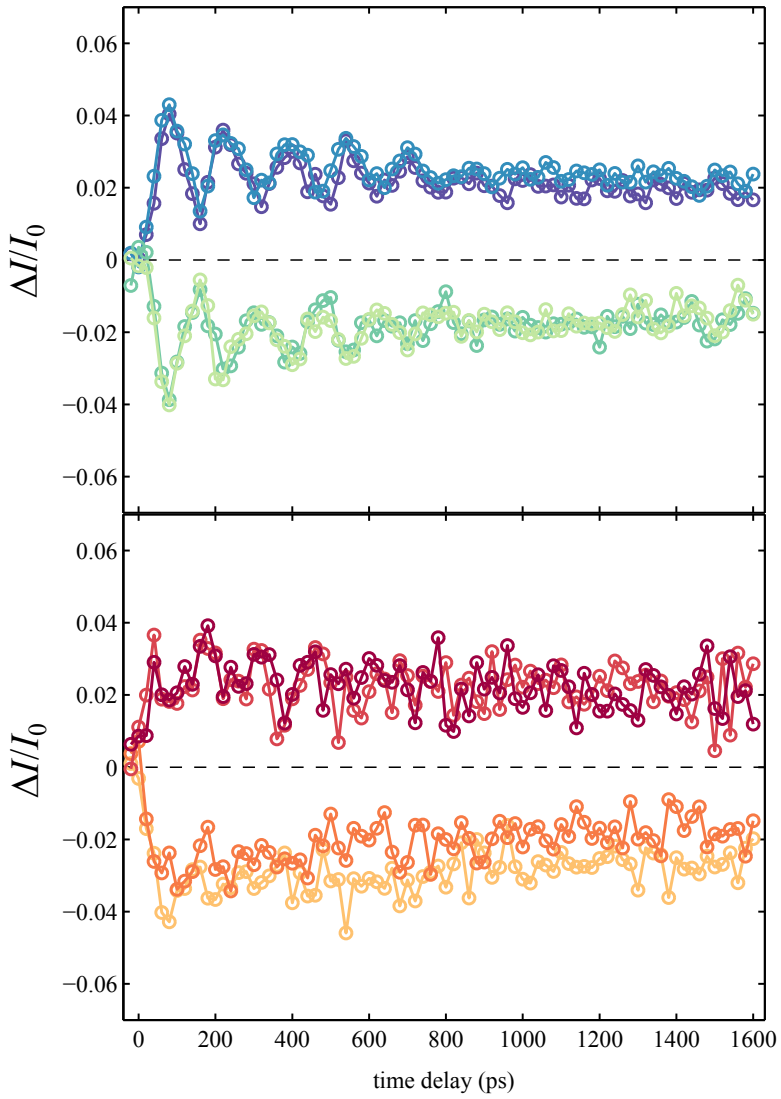

Figure 6.9: The relative intensity change of the first four Bragg peaks are shown. The signature of the acoustic phonon is clearly seen.

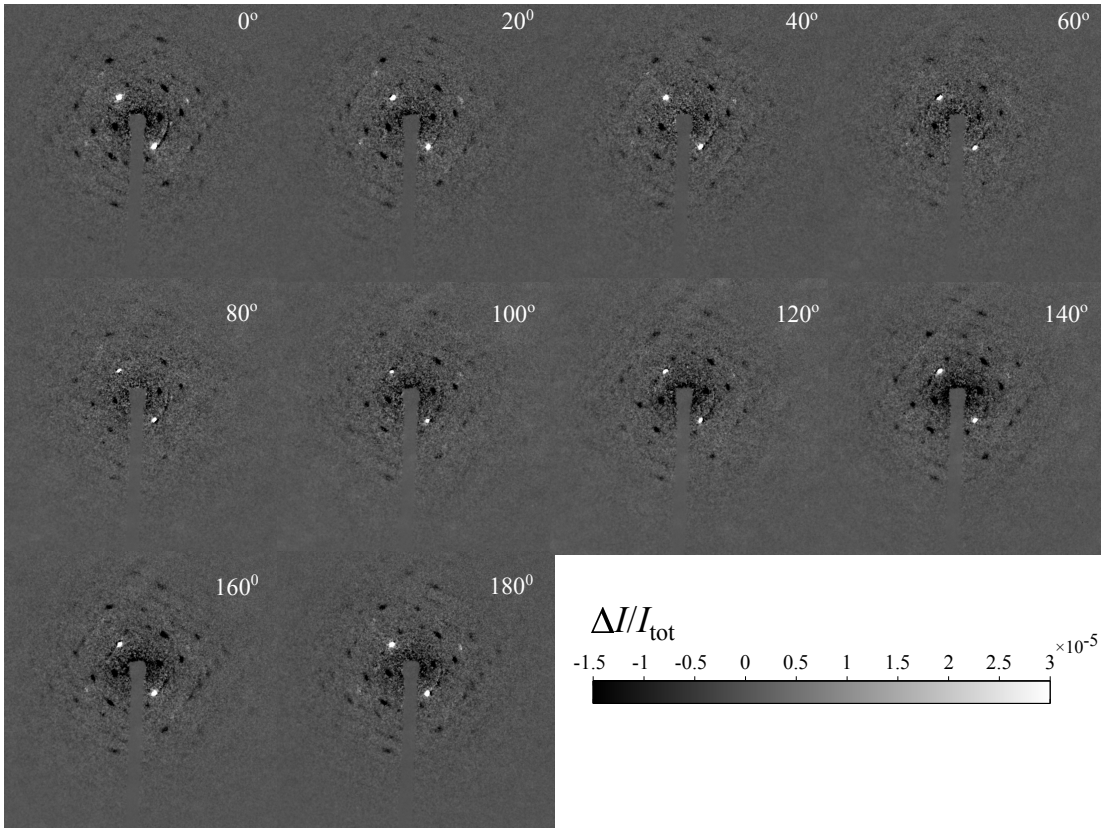

Figure 6.10: Difference images for different polarisation of the pump beam.

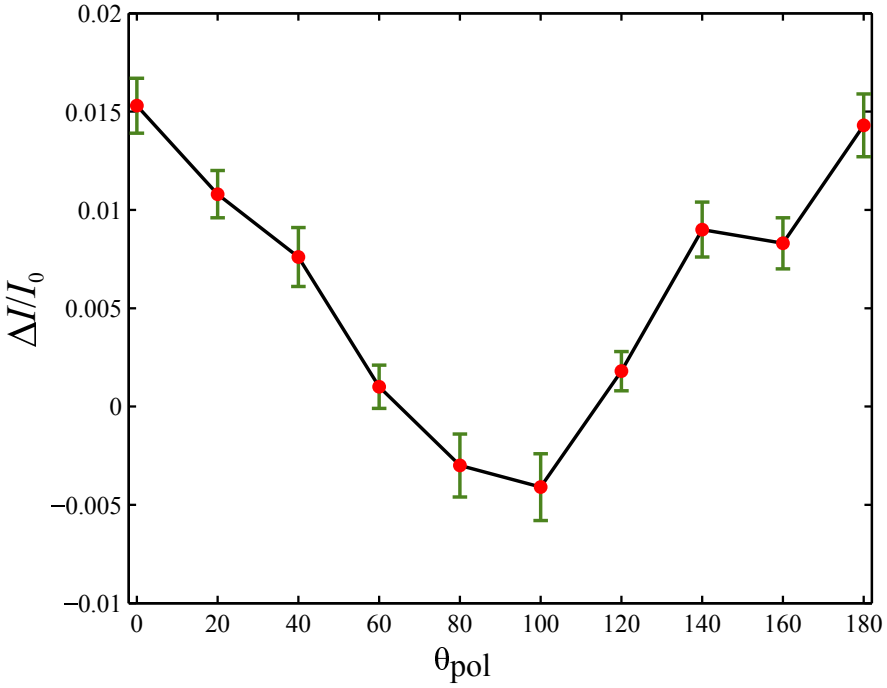

Figure 6.11: Plot showing the polarisation dependence

$$\sigma = \sqrt{\frac{1}{N-1}\sum_{i=1}^{N}|I_i - \mu|^2} \tag{6.6}$$

where I_i is the intensity of the ith measurement, N is the total number of repeated measurements and μ is the mean of the sample given by

$$\mu = \frac{1}{N}\sum_{i=1}^{N} I_i \tag{6.7}$$

There is a clear polarisation dependence on the magnitude of the changes.

6.3.2.1 Discussion

Thermal data show that structural changes take place when the temperature is lowered, but unfortunately offer no clear indication as to the doubling of the cell because of the marked absence of superlattice reflections in the diffraction pat-

terns. This might be explained by the imagining the following possible scenarios: the preparation of the samples which involves ultramicrotomy of the crystals to produce ultra-thin sections suitable for diffraction experiments, disrupts the crystal structure [3]. The thermal phase transition measurements are then of samples that are no longer in their 'pristine' state. This theory can be tested by using $(EDO{-}TTF)_2PF_6$ crystals and following the same steps as for EDO-MeEDO crystals. The other possibility could be that the superlattice peaks are actually present and that the doubling of the unit cell does take place [4], but the superlattice reflections are simply too weak to be detectable. The ratio of absolute intensities between the most intense peak and the weakest discernible peak in the pattern was found to be 53. This means that it will not be possible to identify reflections that are a factor of 53 weaker than the most intense Bragg peak.

The reason for the delayed intensity change seen for some of the peaks in the time-resolved measurement is not known at this stage and warrants further investigation. But, one could speculate that modification of charge distribution brought about by a HOMO $\rightarrow$ LUMO type excitation will lead to a local structural change and fast thermalisation of molecules along the stack —owing to relatively strong orbital overlap, which will cause some peaks to change in intensity, followed by a slower thermalisation of the neighbouring stack. It should also be mentioned that the sensitivity of the higher order peaks (those appearing at large diffraction angles) as compared to the low order ones to local structural changes is typically higher, which could also help to explain the above observation. Charging of the sample, due to ionisation, can be safely ruled out as the peak intensities (< 10 GW cm^{-2}) used in the experiments are not that which can cause ionisation of the sample.

When a few molecules simultaneously undergo structural changes, pressure can build up inside the crystal which can puts it in a stressed state. The stress is relieved by expansion of the lattice and propagation of a coherent wave travelling through it, close to the speed of sound. This can be seen as an oscillation with

[3] As result of strain from the diamond knife during the cutting process.

[4] as expected according to [166].

a period of hundreds of picoseconds depending on the crystal dimensions. The onset of such an oscillation is typically $\sim$ 90-100 ps after excitation. Therefore the oscillations seen in Fig 6.9 are assigned to acoustic phonons. The damping of the phonons is attributed to the crystal returning to its pre-stressed state. It is worthwhile mentioning here that in an organic material such as this one, the oscillations are one of the strongest observed to the knowledge of the author. The magnitude of the phonons can be an indicator of the strength of the intermolecular forces. As EDO-MeEDO is an organic crystal with Van der Waals forces dominating the inter-stack interactions, it is surprising to see such strong phonon signals. In $(EDO{-}TTF)_2PF_6$, which has very similar crystal structure to EDO-MeEDO, the acoustic phonons were less pronounced [164]. This points to the possibility of a cooperative mechanism, that may be responsible for the enhancement of the oscillations via elastic feedback of the lattice, which in turns leads to structural changes at acoustic timescales. This phenomenon in which structural feedback during solid deformation leads to amplification of photoinduced transformation has been previously reported by Bertoni *et al* in a spin cross-over crystal [169]. It is also not unreasonable to hypothesise that this could be a feature of materials which show second-order phase transition behaviours as they have been studied less commonly than the systems showing first-order phase transition with ultrafast diffraction techniques. Lastly, the results of temperature dependence measurements and time-resolved measurement are compared (see Fig 6.12) and from the similarities, it is predicted that the structural changes associated with lowering of the temperature were similar to changes observed when the sample was photoexcited.

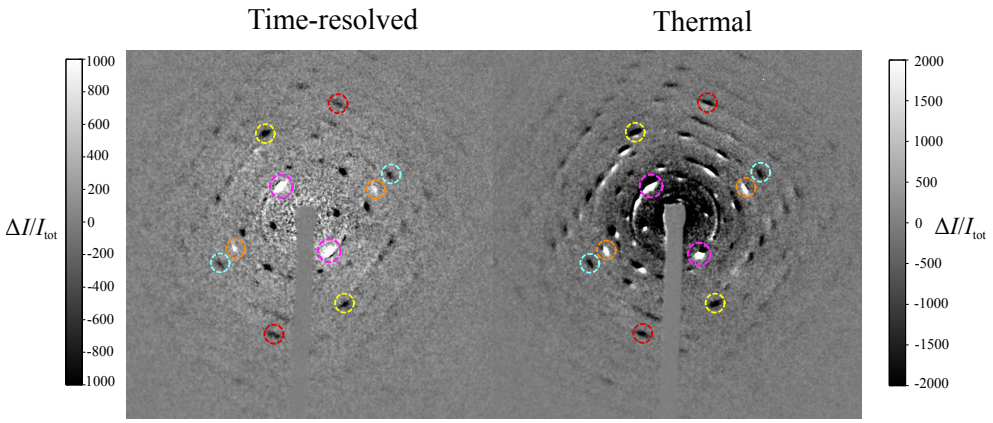

Figure 6.12: The comparison between the time-resolved images and the thermal change. The similarity between the time-resolved and thermal difference pattern in terms of signs of the peaks suggest that the photoinduced structural changes are similar to the thermally driven changes. Some peaks are selected for comparison.

6.4 Conclusion

In this chapter, some results from femtosecond electron diffraction experiments were presented. The aim of the experiments was to study the effect blending MeEDO-TTF with EDO-TTF in a crystal has on the systems overall property. In EDO-TTF crystals, the phase transition has been shown to involve near doubling of the unit cell by Gao *et al* [164], but from our investigation of the mixed complex using electron diffraction, there remains a degree of uncertainty if this occurs or not. Time-resolved experiments also revealed interesting dynamics, such as presence of large amplitude phonons and delayed onset of lower order Bragg peaks. Further experiments (fluence dependence, for instance) and inputs from spectroscopy/theoretical simulations are needed to gain a better understanding of this intriguing system.

Chapter 7

Concluding Remarks and Outlook

In this PhD work, photoinduced dynamics of two organic crystals were investigated using time-resolved absorption spectroscopy and/or femtosecond electron diffraction. One of the systems belonged to a photochromic family of compounds known as spirooxazines and the other was a strongly correlated organic salt, EDO-MeEDO.

The dynamics of chemical reaction in spirooxazines were studied in solution and crystalline state following UV excitation using a home-built transient absorption setup. In the solution phase, the spirooxazines underwent ring-opening and isomerisation resulting in the formation of merocynanine isomers within 1 ps post-excitation. The reaction reached completion with the formation of trans-merocyanine species, which were found to emerge in approximately 80 ps, in good agreement with previously reported studies on the system. For experiments on crystals of spirooxazines, a new methodology was needed due to reversibility issues associated with irrevocable accretion of products. To this end, an ultrafast tunable laser source was built and integrated with the transient absorption setup. The ultrafast and tunable nature of the source permitted fixing the wavelength to the absorption maximum of the generated photoproduct molecules in order to convert them back to the initial, 'pre-excited' state much faster than the mani-

festation of the crystal damage. The methodology (synchronised photoreversion), therefore made use of a non-collinear optical amplifier whose output pulses acted as the photoreversion pulses. Naturally, a new acquisition scheme was required to accommodate the additional beam. The implemented scheme —described in chapter 4, not only allowed precise control of the arrival times of pump, probe and photoreversion beams, but also enabled *in situ* monitoring of the product buildup and hence crystal damage. Experiments performed under this scheme established that spirooxazines molecules can not convert to the fully isomerised trans-products, instead a transient with strong absorption at 500 nm forms after excitation. Simulations on a spriooxazine supercell were performed in which the geometries of the spirooxazine molecules prior to and after cleaving the C-O bond were optimised using *ab inito* methods and these intimated that the transient was likely a ring-opened version of the spiroform with the oxazine and indoline rings bent inwards towards each other. This contrasts with results in solution in which the spiroform is able to fully convert to the merocynanine form. This was rationalised by noting the lack of free volume in crystals, which prohibits large structural changes. A very important result to come out his work was that, with synchronised photoreversion, the damage due to product accumulation can be greatly minimised. No degradation of the sample was observed for up to 10^4 laser shots at fluences that were conquerable to those that would be required for femtosecond electron diffraction studies of this system.

A slightly different direction in terms of photophysics investigation was taken with another molecular crystal, namely EDO-MeEDO. EDO-MeEDO (containing 89/11 % mixture of EDO-TTF/MeEDO-TTF molecules) undergoes a phase transition as opposed to a chemical reaction. The authors who first synthesised the system performed crystallography, Raman spectroscopy and electrical conductivity characterisation of this mixed crystal system. Their work ascertained that EDO-MeEDO undergoes a second-order phase transition in which the first derivative of the order parameter is continuous. A near doubling of one of unit cell axis (one that is parallel to the stacking direction) at the low temperature

($<$ 200 K) was observed by the authors for this crystal. In the measurements reported in chapter 6 to study the structural dynamics of phase transition of this system, doubling of the unit cell —which would manifest in appearance of new peaks, could not be unambiguously confirmed. Lowering the temperature below the critical temperature resulted in a structural change, but any new peaks indicating doubling of the cell were not observed. It was surmised that doubling of the unit cell could have taken place, but the sensitivity of the instrument to detect the new peaks (which would be much weaker in comparison to the original peaks) may not have been enough. Alternatively, the sectioning of the crystals with the ultramicrotome could have had an effect on the crystal as the strain from the knife could potentially be detrimental. Nevertheless, the system was photoexcited at low temperature (100 K) with 800 nm light resulting in time-resolved profile displaying a delayed response of the lower order peaks when compared to the higher order peaks. The offset was found to be approximately 15 ps. Two scenarios were theorised that could help explain this observation; rapid thermalisation of the stacking column after initial excitation causing some peaks to change in intensity and a short time later, thermalisation of the neighbouring stack resulting in other peaks undergoing intensity changes was imagined. The other noted that higher order peaks can be more sensitive to structural changes than lower order ones. Furthermore, very strong oscillation on 100 ps timescales were observed, which for a soft-material with relatively weak intermolecular bonds was deemed to be peculiar, especially since EDO-TTF which has been studied previously with femtosecond electron diffraction showed much less pronounced oscillations despite very similar crystal structure to EDO-MeEDO. It was postulated that this could be a feature of the second-order phase transition materials since prior to this diffraction study, most systems investigated by FED were the ones that showed first-order behaviours. Another theory was that cooperative effects are in effect at acoustic time scales, leading to a combination of structural changes and crystal expansion. At the present stage of investigation, these results cannot be considered complete or conclusive for these sorts of systems and more work

is certainly needed, but it has nevertheless provided useful food for thought for future experiments on these type of systems.

Outlook

The work presented in chapter 4 of this thesis has now opened up the prospect to conduct pump-probe experiments to investigate photochemical reactions in molecular crystals provided that they are suited for synchronised photoreversion. The quality and quantity of data was good and sufficient enough to perform analysis to extract the kinetics. A more thorough treatment of the data, i.e. global and/or target analysis will now be undertaken to model the dynamics and present a picture of the reaction mechanism. This will require more experiments with finer time steps ($<$ 50 fs) to get a more sampled view of the very early dynamics (between 0-100 fs) and also extension of the measured range to at least 100 ps. This will be attempted with repetition rates that are higher than those used in the present work to improve on data acquisition times and signal-to-noise ratios. In terms of the modelling of the transient absorption data, aside from the global analysis, molecular dynamics (MD) simulations are planned with Dr Kochman.

The stage is now set to perform femtosecond electron diffraction experiments with the aim to gain an atomistic perspective of the structural dynamics in spirooxazines. At first, the forward photoreaction would be investigated to probe the structural changes associated with the ring-opening process. As the electron diffraction experiments require that they be performed in vacuum, sample evaporation can pose a potential hurdle. In order to avoid this issue, the crystalline samples will be cooled using either a Peltier element mounted directly to the sample holder or with liquid nitrogen prior to evacuating the diffraction apparatus. Afterwards, the data accumulated from diffraction experiments will be analysed and modelled using the methodology developed by Dr Hayes and implemented in [146] to develop a mechanistic picture of the reaction and to ultimately

resolve the identity of the ring-opened product.

In addition, experiments on diarytethene crystals have also been planned. Diarlyethene are arguably more promising than spirooxazines for industrial applications, for example as photoswitches, as they are totally photochromic in the solid state and can undergo comparable number of photocycles. As was mentioned in chapters 3 and 4, this system has been studied previously using transient absorption and femtosecond electron diffraction by Jean-Ruel *et al*, but their studies focused on only the forward reaction [44, 97]. In order to improve the performance of diarytehene photoswitches, structural dynamics of the back reaction will be very helpful as it could offer insight into what changes can be made to the chemical structure, to make the system more robust and efficient. With synchronised photoreversion, the back reaction would be investigated using the two ultrafast techniques used in this thesis work.

Femtosecond electron diffraction on EDO-MeEDO will be repeated with new (and fresh) samples, this time also with different orientations to gain more information on the system. Moreover, quasi-one dimensional molecular crystals that undergo second-order phase transitions are also currently being sought for comparisons with EDO-MeEDO, especially at acoustic timescales. Charge density wave materials are a potential candidate for this purpose.

Appendices

Appendix A

Calculations of cross-sections and excitation fractions

This appendix outlines the steps needed to calculate the absorption cross-sections from steady-state absorption measurements and to estimate excitation fractions. Cases of solution phase and crystalline will be treated separately.

A.1 Solution phase

The relationship between absorbance (or OD), concentration, c and path length, l was met in chapter 3 and was given by the Beer-Lambert law

$$\mathrm{OD} = \varepsilon c l \tag{A.1}$$

For the case of Spironaphthooxazine ($C_{22}H_{20}N_2O$)

$M_r = 328.40\,\mathrm{g\ mol^{-1}}$

OD = 1 (for $\lambda = 266$ nm)

$l = 1$ mm

$c = 0.5\ \mathrm{mM} = 0.5 \times 10^{-3}\ \mathrm{mol\ dm^{-3}}$

Using the above, the molar extinction coefficient ε can be calculated

$$\begin{aligned}\varepsilon &= \frac{\text{OD}}{c\,(\text{mol cm}^{-3}) \times l\,(\text{cm})} \\ &= \frac{1}{0.5 \times 10^{-6}\,(\text{mol cm}^{-3}) \times 0.1\,(\text{cm})} \\ &= 2 \times 10^{7}\,\text{mol}^{-1}\,\text{cm}^{2}\end{aligned}$$

Dividing ε by the Avogadro's constant,N_A gives the cross-section in cm^2

$$\begin{aligned}\sigma &= \frac{\varepsilon\,(\text{mol}^{-1}\,\text{cm}^{2})}{N_A\,(\text{mol}^{-1})} \\ &= \frac{2 \times 10^{7}\,(\text{mol}^{-1}\,\text{cm}^{2})}{6.022 \times 10^{23}\,(\text{mol}^{-1})} \\ &= 3.32 \times 10^{-17}\text{cm}^{2}\end{aligned}$$

In order to calculate the fraction of excited molecules in a given experiment, the experimentally set parameters, such as the pulse energy and the spot size at the sample position need to be known. Solution phase experiments performed in chapter 4 used the following parameters:

Excitation wavelength (nm) = 266
Measured laser power (mW) = 0.165
repetition rate (Hz) = 500
spot size (cm) = 330×10^{-4}

$$\text{number of photons} = \frac{E\,(\text{J})\,\lambda\,(\text{m})}{h\,(\text{J s})\,\text{c}\,(\text{m s}^{-1})} \tag{A.2}$$

where E is the energy per pulse, which can be calculated by the measured power (units W or J s^{-1}) and repetition rate (unit Hz or s^{-1}).

$$E\,(\text{J}) = \frac{\text{power}\ (\text{J s}^{-1})}{\text{repetition rate}\ (\text{s}^{-1})} \tag{A.3}$$

The pulse energy is calculated as 330×10^{-9} J or 330 nJ and using this value in Eq A.2, the total number of photons turn out to be 4.4×10^{11}. As the cross-sectional area (assuming a square) is spot size squared, dividing the number of photons by the cross-sectional area gives the number of photons that pass through the probe region, i.e. photon flux, which is equal to $F = \frac{(4.4 \times 10^{-11}\,\text{photons})}{(1.09 \times 10^{-3}\text{cm}^2)} = 4.06 \times 10^{14}\,\text{photons cm}^{-2}$. Multiplying this number with the absorption cross-section times 100 gives the percentage excitation.

$$\begin{aligned} \%\ \text{excitation} &= \sigma(\text{cm}^2) F(\text{photons cm}^{-2}) \times 100 \\ &= (3.32 \times 10^{-17}\text{cm}^2)\,(4.06 \times 10^{14}\,\text{photons cm}^{-2}) \times 100 \\ &= 1.37\,\% \end{aligned}$$

Therefore, at a fluence of 0.48 mJ cm^2, the percentage excitation is found to be approximately 1.35 %.

A.2 Crystalline State

To calculate the percentage excitation expected from pumping crystalline samples, an additional detail is required, namely the crystal density. Below a calculation is presented for spirooxazine crystal. Information from the steady-state absorption measurement of the crystal can be used to calculate the absorption coefficient, α, which is often quoted in units of cm^{-1} as

$$\alpha = \frac{\text{OD}}{l\,(\text{cm})} \tag{A.4}$$

where l is the sample thickness.

The absorption coefficient is related to absorption cross-section by the following relationship

$$\sigma = \frac{\alpha}{n} \tag{A.5}$$

where n is the number density given by

$$n = \frac{\rho\,(\text{g cm}^{-3})N_A\,(\text{mol}^{-1})}{\text{M}_\text{r}\,(\text{g mol}^{-1})} \tag{A.6}$$

Here ρ is the density of the crystal in g cm^{-3}, which can be obtained by solving the crystal structure, N_A is Avogadro's constant in mol^{-1} and M_r is the molecular weight in g mol^{-1}. Therefore, the number density has the units of molecules cm^{-3} and when inserted in Eq A.5, gives the cross-section in units of cm^2. Once the absorption cross-section, σ has been calculated, the procedure outlined earlier can be used to determine the fraction excitation. Care must be taken with the units of different quantities in the formulae; consistency must be maintained in numerator and denominator. Below is a worked example.

OD = 0.87 (for $\lambda = 266$ nm)
$l = 100\,\text{nm} = 100 \times 10^{-7}$ cm $= 10^{-5}$ cm
$\rho_{\text{SNO}} = 1.22\,\text{g cm}^{-3}$ (taken from CIF data in [130])

The absorption coefficient, α in units of cm^{-1} is calculated to be 87000 cm^{-1} and the number density is found to be 2.24×10^{21}cm^{-3}. Using Eq A.5 gives the value of 3.88×10^{-17}cm^2 for the absorption cross-section. The following was conditions were used in the experiments.

Excitation wavelength (nm) = 266
Measured power (µW) = 8.25
repetition rate (Hz)= 31.25
spot size (cm) = 137×10^{-4}
Therefore, the fluence is 1.4 mJ cm^{-2} and the photon flux is 1.8×10^{15} photons cm^{-2}. This corresponds to approximately 7 % excitation of the probed region.

Another, often useful, calculation is that of the penetration depth, δ defined as the depth at which the intensity of the incoming radiation inside the material falls to $\frac{1}{e}$ (about 37 %) of its original value and, therefore, is a measure of how deep an electromagnetic radiation can penetrate into a material. It can straightforwardly be calculated by taking the reciprocal of the absorption coefficient.

$$\delta\,(\mathrm{m}) = \frac{1}{\alpha(\mathrm{m}^{-1})} \tag{A.7}$$

Therefore, a 266 nm laser penetrates about 114.94 nm in the SNO crystal.

Appendix B

Matlab codes

B.1 Matlab code: phase matching calculation

```
clear all;
close all;
clc;

% Sellmier constants (SC) taken from Opt.Commun.,
   184,485-491 (2000)

% Note: Only applicable for BBO

% SC BBO ordinary ray

a = 2.7359;
b = 0.01878;
c = 0.01822;
d = 0.01471;
e = 0.0006081;
f = 0.00006740;
```

```
% SC BBO extraordinary ray

g = 2.3753;
h = 0.01224;
i = 0.01667;
j = 0.01627;
k = 0.0005716;
l = 0.00006305;

% Start calculations

v = 3e+8;   % speed of light

pumpWave = 400;  % pump wavelength

n_op = 1.6934;  % pump ordinary refractive index

n_ep = 1.5687;  % pump extraordinary refractive index

sigWave = 450:1:800;  % signal wavelength

slambda = sigWave/1000;   % signal wavelength in microns

nWavelength = length(slambda);
```

```
for ii = 1 : nWavelength

    sFrequency(ii) = v./(sigWave(ii));

    pFrequency = v./pumpWave;

    idlerFrequnecy = pFrequency-sFrequency(ii);

    idlerWave(ii) = v./idlerFrequnecy;

    ilambda(ii) = idlerWave(ii)./1000;

   % Solve Sellmeier equations to compute refractive
      indices

     no_squared = a+(b/(slambda(ii).^2-c))-d*slambda(ii).^2
         + e*slambda(ii).^4-f*slambda(ii).^6;

     n_os(ii) = sqrt(no_squared);

     ne_squared = g+(h/(slambda(ii).^2-i))-j*slambda(ii).^2
         + k*slambda(ii).^4-l*slambda(ii).^6;

     n_es(ii) = sqrt(ne_squared);

     noi_squared = a+(b/(ilambda(ii).^2-c))-d*ilambda(ii)
        .^2 + e*ilambda(ii).^4-f*ilambda(ii).^6;
     n_oi(ii) = sqrt(noi_squared);
```

```
    nei_squared = g+(h/(ilambda(ii).^2-i))-j*ilambda(ii)
        .^2 + k*ilambda(ii).^4-l*ilambda(ii).^6;

    n_ei(ii) = sqrt(nei_squared);

end

a_int = 3.1:0.2:4;  % define internal angles to compute
na = length(a_int);

for kk = 1 : na;

kk
    for ll = 1 : nWavelength


        n_p = (pumpWave./sigWave(ll))*n_os(ll)*(cosd(a_int
            (kk))+sqrt( (sigWave(ll).^2./idlerWave(ll).^2)
            *(n_oi(ll).^2./n_os(ll).^2)-sind(a_int(kk))^2))
            ;


            theta_pm(kk,ll) = asind(sqrt((n_op^2/n_p^2)-1)
                *((n_op^2/n_ep^2)-1)^(-0.5));


    end

end
```

```
    % Plot results

   for nn = 1 : na

            alpha = a_int(nn);
          fthetaPM = sgolayfilt(theta_pm(nn,:),3,31);

       plot(sigWave,theta_pm(nn,:));
       xlabel('wavelength (nm)');
       ylabel('\theta_{p} (degree)');
       legendInfo{nn}=['\alpha = ', num2str(alpha) '\circ'];
       legend(legendInfo)
       hold all
       legend boxoff

   end

% External Angle (Snell's law)

nBBO_o = 1.6934;  % ordinary refractive index pump for BBO
nair = 1;  % refractive index of air
aint_f = 3.7; % internal angle
theta_ext = asind((nBBO_o*sind(aint_f)/nair)) % external
                                               % angle
```

B.2 Fit Function

```
function f = kinFitFun(para,t)

% Equation used to fit data.

comp1 = para(1).*exp(-(t-para(2))./para(3))...
  .*exp(para(4).^2./(2*para(3).^2))...
  .*(1+erf((t-para(2)-(para(4).^2./para(3)))/(sqrt(2*para
      (4)))));

comp2 = para(5).*exp(-(t-para(2))./para(6))...
  .*exp(para(4).^2./(2*para(6).^2))...
  .*(1+erf((t-para(2)-(para(4).^2./para(6)))/(sqrt(2*para
      (4)))));


sumComps = comp1 + comp2
F = (0.5.*sumComps);

end
```

B.2.1 Matlab code: curve fitting

```
clear all;
close all;
clc;

% Load data for fitting and save to variables

file = open('D:\PhD\Theses\Khalid_Thesis\Matlab\data
    fitting\sol_430nm_trace.fig');

t = get(gco,'xdata');
OD = get(gco,'ydata');

% Provide reasonable guesses

p1 = 4e-3;      % A
p2 = -0.1;      % t=0
p3 = 0.70;      % tau1
p4 = 0.22;      % irf
p5 = 0.5e-3;    % B
p6 = inf;       % tau2


para=lsqcurvefit(@kinFitFun,[p1,p2,p3,p4,p5,p6],t, OD);
```

```
% Save fit parameters

A = para(1);
t0 = para(2);
tau1 = para(3);
sigma_irf = para(4);
B = para(5);
tau2 = para(6);

yfit = kinFitFun(para,t);
residual = OD-yfit;

[beta,resnorm,resid,exitflag,output,lambda,J] =
    lsqcurvefit(@fitKin,[p1,p2,p3,p4,p5,p6],t, OD);

ci = nlparci(beta,resid,'jacobian',J)

% Plot results

 plot(t,OD,'o','color','k','linewidth',2);
 hold all;
 plot(t,yfit,'color','r','linewidth',2)
```

References

1. J. Simpson, J. Speake, Eds., *The Oxford Dictionary of Proverbs* (Oxford University Press, 2008).
2. E. Rutherford, *Philos. Mag. 6,* **21**, 669–688 (1911).
3. J. J. Thomson, *Philos. Mag. A. Series. 5,* **44**, 293–316 (1897).
4. A. L. Schawlow, C. H. Townes, *Phys. Rev.,* **112**, 1940–1949 (1958).
5. J. Hecht, *Opt. Eng.,* **49**, 091002 (2010).
6. G. Binnig, H. Rohrer, *Surf. Sci.,* **126**, 236–244 (1983).
7. W. T. Welford, *Advanced Light Microscopy. Vol. 1. Principles and Basic Properties* (Informa UK Limited, 1989).
8. D. B. Murphy, M. W. Davidson, *Fundamentals of Light Microscopy and Electronic Imaging* (Wiley-Blackwell, 2012).
9. Editorial, *Nat. Photon,* **3**, 361–361 (2009).
10. J. Bückers, D. Wildanger, G. Vicidomini, L. Kastrup, S. W. Hell, *Opt. Express,* **19**, 3130 (2011).
11. S. W. Hell, J. Wichmann, *Opt. Lett.,* **19**, 780 (1994).
12. R. V. Noorden, *Nature,* **514**, 286–286 (2014).
13. M. S. Pshenichnikov, A. Baltuška, D. A. Wiersma, 409–445 (2004).
14. D. E. Spence, P. N. Kean, W. Sibbett, *Opt. Lett.,* **16**, 42 (1991).
15. `https://17strevdav.wordpress.com/`.
16. I. Pomerantz *et al.*, *Phys. Rev. Lett.,* **113**, 184801 (2014).

17. J. R. Dwyer *et al.*, *J. Mod. Opt.,* **54**, 923–942 (2007).

18. R. Henderson, *Q. Rev. Biophys.,* **28**, 171 (1995).

19. R. Henderson, *Nature,* **415**, 833–833 (2002).

20. B. W. J. McNeil, N. R. Thompson, *Nat. Photon,* **4**, 814–821 (2010).

21. H. N. Chapman *et al.*, *Nat. Phys.,* **2**, 839–843 (2006).

22. *Deutsches Elektronen-Synchrotron*, `http://www.desy.de`.

23. *SLAC National Accelerator Laboratory*, `https://www6.slac.stanford.edu/`.

24. R. Bonifacio, C. Pellegrini, L. Narducci, *Opt. Commun.,* **50**, 373–378 (1984).

25. G. Geloni, V. Kocharyan, E. Saldin, *J. Mod. Opt.,* **58**, 1391–1403 (2011).

26. I. Grguraš *et al.*, *Nat. Photon,* **6**, 852–857 (2012).

27. M. Hada, K. Pichugin, G. Sciaini, *Eur. Phys. J. Spec. Top.,* **222**, 1093–1123 (2013).

28. A. Căsăndruc, R. Bücker, G. Kassier, R. J. D. Miller, *Appl. Phys. Lett.,* **109**, 091105 (2016).

29. D. A. Shapiro *et al.*, *Nat. Photon.,* **8**, 765–769 (2014).

30. B. J. Siwick, J. R. Dwyer, R. E. Jordan, R. J. D. Miller, *J. Appl. Phys.,* **92**, 1643 (2002).

31. M. Aidelsburger, F. O. Kirchner, F. Krausz, P. Baum, *Proc. Natl. Acad. Sci. U.S.A.,* **107**, 19714–19719 (2010).

32. G. Herink, D. R. Solli, M. Gulde, C. Ropers, *Nature,* **483**, 190–193 (2012).

33. G. Sciaini, R. J. D. Miller, *Rep. Prog. Phys.,* **74**, 096101 (2011).

34. P. Zhu *et al.*, *New J. Phys.,* **17**, 063004 (2015).

35. G. Mourou, *Appl. Phys. Lett.,* **41**, 44 (1982).

36. A. A. Ischenko *et al.*, *Appl. Phys. B.,* **32**, 161–163 (1983).

37. J. C. Williamson, M. Dantus, S. B. Kim, A. Zewail, *Chem. Phys. Lett.,* **196**, 529–534 (1992).

38. B. J. Siwick, *Science,* **302**, 1382–1385 (2003).

39. G. Sciaini *et al.*, *Nature,* **458**, 56–59 (2009).

40. S. Nie, X. Wang, J. Li, R. Clinite, J. Cao, *Microsc. Res. Tech.,* **72**, 131–143 (2009).

41. M. M. Lin, D. Shorokhov, A. H. Zewail, *J. Am. Chem. Soc.,* **133**, 17072–17086 (2011).

42. S. P. Weathersby *et al.*, *Rev. Sci. Instrum.,* **86**, 073702 (2015).

43. V. R. Morrison *et al.*, *Science,* **346**, 445–448 (2014).

44. J. R. Hubert *et al.*, *J. Phys. Chem. B,* **117**, 15894–15902 (2013).

45. R. Trebino, *Frequency-Resolved Optical Gating: The Measurement of Ultrashort Laser Pulses* (Springer Nature, 2000).

46. B. M. Oerle, G. J. Ernst, *Appl. Opt.,* **35**, 5177 (1996).

47. R. Trebino *et al.*, *Rev. Sci. Instrum.,* **68**, 3277 (1997).

48. C. Iaconis, I. A. Walmsley, *Opt. Lett.,* **23**, 792 (1998).

49. E. Miesak, R. Negres, *Appl. Opt.,* **37**, 8146 (1998).

50. R. L. Fork, O. E. Martinez, J. P. Gordon, *Opt. Lett.,* **9**, 150 (1984).

51. W. E. Lamb, *Phys. Rev.,* **134**, 1429–1450 (1964).

52. J. Herrmann, M. Müller, *Opt. Commun.,* **135**, 83–88 (1997).

53. S. Zeng *et al.*, *Rev. Sci. Instrum,* **78**, 015103 (2007).

54. B. K. Garside, *J. Appl. Phys.,* **44**, 2335 (1973).

55. T. Brabec, C. Spielmann, P. F. Curley, F. Krausz, *Opt. Lett.,* **17**, 1292 (1992).

56. G. P. Agrawal, *J. Opt. Soc. Am. B,* **28** (2011).

57. R. W. Boyd, *Nonlinear Optics (3rd Edition)* (Academic Press, 2008).

58. Y. B. Band, D. F. Heller, J. R. Ackerhalt, J. S. Krasinski, *Phys. Rev. A,* **42**, 1515–1521 (1990).

59. J. Butet, P. F. Brevet, O. J. F. Martin, *ACS Nano,* **9**, 10545–10562 (2015).

60. X. Chen, O. Nadiarynkh, S. Plotnikov, P. J. Campagnola, *Nat. Protoc.,* **7**, 654–669 (2012).

61. T. Manaka, M. Iwamoto, *Light Sci. Appl.,* **5**, e16040 (2015).

62. P. A. Franken, A. E. Hill, C. W. Peters, G. Weinreich, *Phys. Rev. Lett.,* **7**, 118–119 (1961).

63. M. Bass, P. A. Franken, A. E. Hill, C. W. Peters, G. Weinreich, *Phys. Rev. Lett.,* **8**, 18–18 (1962).

64. R. Baumgartner, R. Byer, *IEEE J. Quant. Electron.,* **15**, 432–444 (1979).

65. G. Cerullo, S. D. Silvestri, *Rev. Sci. Instrum.,* **74**, 1 (2003).

66. Y. R. Shen, *Prog. Quant. Electron.,* **4**, 1–34 (1975).

67. J. H. Marburger, *Prog. Quant. Electron.,* **4**, 35–110 (1975).

68. B. A. Cumberland, J. C. Travers, S. V. Popov, J. R. Taylor, *Opt. Lett.,* **33**, 2122 (2008).

69. A. M. Zheltikov, *Phys. Usp.,* **49**, 605 (2006).

70. M. Piché, F. Salin, *Opt. Lett.,* **18**, 1041 (1993).

71. G. Cerullo, S. D. Silvestri, V. Magni, *Opt. Lett.,* **19**, 1040 (1994).

72. F. Shimizu, *Phys. Rev. Lett.,* **19**, 1097–1100 (1967).

73. G. H. C. New, J. F. Ward, *Phys. Rev. Lett.,* **19**, 556–559 (1967).

74. *'SNLO nonlinear optics code available from A. V. Smith, AS-Photonics, Albuquerque, NM.*

75. T. J. Driscoll, G. M. Gale, F. Hache, *Opt. Commun.,* **110**, 638–644 (1994).

76. `http://refractiveindex.info/`.

77. T. M. Kardaś, B. Ratajska-Gadomska, W. Gadomski, A. Lapini, R. Righini, *Opt. Express,* **21**, 24201 (2013).

78. R. L. Carman, R. Y. Chiao, P. L. Kelley, *Phys. Rev. Lett.,* **17**, 1281–1283 (1966).

79. P. Tzankov, I. Buchvarov, T. Fiebig, *Opt. Commun.,* **203**, 107–113 (2002).

80. G. Ghosh, *Appl. Opt.,* **36**, 1540 (1997).

81. N. Matuschek, L. Gallmann, D. Sutter, G. Steinmeyer, U. Keller, *Appl. Phys. B.,* **71**, 509–522 (2000).

82. T. Wilhelm, J. Piel, E. Riedle, *Opt. Lett.,* **22**, 1494 (1997).

83. R. Bonifacio, L. A. Lugiato, *Phys. Rev. A,* **11**, 1507–1521 (1975).

84. R. Berera, R. v. Grondelle, J. T. M. Kennis, *Photosynth. Res.,* **101**, 105–118 (2009).

85. P. W. Atkins, *Molecular Quantum Mechanics (fifth edition)* (OUP Oxford, 2010).

86. W. Domcke, D. R. Yarkony, *Annu. Rev. Phys. Chem.,* **63**, 325–352 (2012).

87. D. L. Webster, *Phys. Rev.,* **27**, 637–644 (1926).

88. A. Jabłoński, *Nature,* **131**, 839–840 (1933).

89. J. R. Lakowicz, Ed., *Principles of Fluorescence Spectroscopy* (Springer Nature, 2006).

90. S. E. Braslavsky, *Pure and Applied Chemistry* **79** (2007).

91. J. M. Hollas, *Modern Spectroscopy (4th Ed.)* (John Wiley, 2004).

92. I. H. M. v. Stokkum, D. S. Larsen, R. v. Grondelle, *Biochim. Biophys. Acta.,* **1657**, 82–104 (2004).

93. C. Ruckebusch, M. Sliwa, P. Pernot, A. de Juan, R. Tauler, *J. Photochem. Photobiol. C: Photochem. Rev,* **13**, 1–27 (2012).

94. J. Ayache, L. Beaunier, J. Boumendil, G. Ehret, D. Laub, *Sample Preparation Handbook for Transmission Electron Microscopy* (Springer Science, 2010).

95. F. O. Kirchner, S. Lahme, E. Riedle, P. Baum, *AIP Adv.,* **4**, 077134 (2014).

96. P. R. Poulin, K. A. Nelson, *Science,* **313**, 1756–1760 (2006).

97. H. Jean-Ruel *et al.*, *J. Phys. Chem. A,* **115**, 13158–13168 (2011).

98. M. Lorenc *et al.*, *Appl. Phys. B,* **74**, 19–27 (2002).

99. U. Megerle, I. Pugliesi, C. Schriever, C. F. Sailer, E. Riedle, *Appl. Phys. B,* **96**, 215–231 (2009).

100. M. Irie, *Chem. Rev.,* **100**, 1683–1684 (2000).

101. V. I. Minkin, *Chem. Rev.,* **104**, 2751–2776 (2004).

102. E. Deniz, S. Impellizzeri, S. Sortino, F. M. Raymo, *Can. J. Chem.,* **89**, 110–116 (2011).

103. S. Kobatake, S. Takami, H. Muto, T. Ishikawa, M. Irie, *Nature,* **446**, 778–781 (2007).

104. H. M. D. Bandara, S. C. Burdette, *Chem. Soc. Rev.,* **41**, 1809–1825 (2012).

105. M. A. Wolak, C. J. Thomas, N. B. Gillespie, R. R. Birge, W. J. Lees, *J. Org. Chem.,* **68**, 319–326 (2003).

106. R. Klajn, *Chem. Soc. Rev.,* **43**, 148–184 (2014).

107. D. A. Parthenopoulos, P. M. Rentzepis, *Science,* **245**, 843–845 (1989).

108. G. Jiang, Y. Song, X. Guo, D. Zhang, D. Zhu, *Adv. Mater.,* **20**, 2888–2898 (2008).

109. G. Berkovic, V. Krongauz, V. Weiss, *Chem. Rev.,* **100**, 1741–1754 (2000).

110. N. Tamai, H. Miyasaka, *Chem. Rev.,* **100**, 1875–1890 (2000).

111. X. Li, J. Li, Y. Wang, T. Matsuura, J. Meng, *J. Photochem. Photobiol. A,* **161**, 201–213 (2004).

112. P. J. Castro, I. Gómez, M. Cossi, M. Reguero, *J. Phys. Chem. A,* **116**, 8148–8158 (2012).

113. N. W. Tyer, R. S. Becker, *J. Am. Chem. Soc.,* **92**, 1289–1294 (1970).

114. I. Gómez, M. Reguero, M. A. Robb, *J. Phys. Chem. A,* **110**, 3986–3991 (2006).

115. F. Liu, K. Morokuma, *J. Am. Chem. Soc.,* **135**, 10693–10702 (2013).

116. C. Walter *et al.*, *J. Chem. Phys.,* **140** (2014).

117. R. S. S. Kumar, L. Lüer, D. Polli, M. Garbugli, G. Lanzani, *Opt. Mater. Express.,* **1**, 293 (2011).

118. M. R. Nunzio, E. O. Danilov, M. A. J. Rodgers, G. Favaro, *Photochem. Photobiol. Sci.,* **9**, 1391–1399 (2010).

119. R. A. Evans *et al.*, *Nat. Mater.,* **4**, 249–253 (2005).

120. L. Poisson, K. D. Raffael, B. Soep, J. M. Mestdagh, G. Buntinx, *J. Am. Chem. Soc.,* **128**, 3169–3178 (2006).

121. M. Suzuki, T. Asahi, H. Masuhara, *J. Photochem. Photobio. A,* **178**, 170–176 (2006).

122. C. Lenoble, R. S. Becker, *J. Photochem.,* **34**, 83–88 (1986).

123. N. Tamai, H. Masuhara, *Chem. Phys. Lett.,* **191**, 189–194 (1992).

124. S. A. Antipin *et al.*, *Chem. Phys. Lett.,* **331**, 378–386 (2000).

125. G. Buntinx *et al.*, *Dyes. Pigm.,* **89**, 305–312 (2011).

126. F. Maurel *et al.*, *J. Phys. Chem. A,* **110**, 4759–4771 (2006).

127. M. Suzuki, T. Asahi, H. Masuhara, *Phys. Chem. Chem. Phys.,* **4**, 185–192 (2002).

128. T. Asahi, Y. Matsuo, H. Masuhara, *Chem. Phys. Lett.,* **256**, 525–530 (1996).

129. M. Suzuki, T. Asahi, H. Masuhara, *Chem. Phys. Chem,* **6**, 2396–2403 (2005).

130. J. Harada, Y. Kawazoe, K. Ogawa, *Chem. Commun.,* **46**, 2593 (2010).

131. K. M. Siddiqui *et al.*, *CrystEngComm,* **18**, 7212–7216 (2016).

132. M. Bradler *et al.*, *Opt. Express,* **21**, 20145 (2013).

133. A. E. Fitzpatrick, C. N. Lincoln, L. J. G. W. v. Wilderen, J. J. v. Thor, *J. Phys. Chem. B,* **116**, 1077–1088 (2012).

134. O. Matsuda, M. C. Larciprete, R. L. Voti, O. B. Wright, *Ultrasonics* **56**, 3–20 (2015).

135. F. Jensen, *Introduction to Computational Chemistry: Second Edition* (Wiley, 2011).

136. *Turbomole V6.3.1 (2010).*

137. A. B. Trofimov, J. Schirmer, *J. Phys. B,* **28**, 2299–2324 (1995).

138. T. Young, *Phil. Trans. R. Soc.,* **92**, 12–48 (1802).

139. L. Broglie, *Philos. Mag. 6,* **47**, 446–458 (1924).

140. C. J. Davisson, L. H. Germer, *Proc. Natl. Acad. Sci. U.S.A.,* **14**, 317–322 (1928).

141. D. Shechtman, I. Blech, D. Gratias, J. W. Cahn, *Phys. Rev. Lett.,* **53**, 1951–1953 (1984).

142. N. Robotti, *Rend. Lincei,* **24**, 7–18 (2012).

143. W. H. Bragg, *Math. Proc. Cambridge.,* **19**, 43–57 (1913).

144. G. Taylor, *Acta Crystallogr. Sect. D,* **59**, 1881–1890 (2003).

145. H. Schenk, *J. Chem. Educ.,* **56**, 383 (1979).

146. T. Ishikawa *et al.*, *Science,* **350**, 1501–1505 (2015).

147. D. H. Dowell, J. F. Schmerge, *Phys. Rev. ST Accel. Beams,* **12** (2009).

148. P. A. Anderson, *Phys. Rev.,* **115**, 553–554 (1959).

149. A. M. Michalik, E. Y. Sherman, J. E. Sipe, *J. Appl. Phys.,* **104**, 054905 (2008).

150. S. Manz *et al.*, *Farad. Discuss.,* **177**, 467–491 (2015).

151. A. Jabłoński, *J. Phys. Chem. Ref. Data.,* **33**, 409 (2004).

152. I. Suh, H. Ohta, Y. Waseda, *J Mater. Sci.,* **23**, 757–760 (1988).

153. D. C. Palmer, S. E. Palmer, *CrystalDiffract Software v.6.6.2*, (2016).

154. A. Facchetti, *Nat. Mater.,* **12**, 598–600 (2013).

155. R. O. Loutfy, Y. Shing, D. K. Murti, *Sol cells,* **5**, 331–341 (1982).

156. D. Jérome, H. J. Schulz, *Adv. Phys.,* **51**, 293–479 (2002).

157. S. E. Brown, *Physica. C. Supercond.,* **514**, 279–289 (2015).

158. S. Koshihara, Y. Takahashi, H. Sakai, Y. Tokura, T. Luty, *J. Phys. Chem. B.,* **103**, 2592–2600 (1999).

159. E. Dagotto, *Science,* **309**, 257–262 (2005).

160. M. Chollet, *Science,* **307**, 86–89 (2005).

161. K. Onda *et al.*, *Phys. Rev. Lett.,* **101** (2008).

162. H. Yamochi, S. Koshihara, *Sci. Technol. Adv. Mater.,* **10**, 024305 (2009).

163. N. Fukazawa *et al.*, *J. Phys. Chem. C,* **116**, 5892–5899 (2012).

164. M. Gao *et al.*, *Nature,* **496**, 343–346 (2013).

165. A. Ota, H. Yamochi, G. Saito, *J. Mater. Chem.,* **12**, 2600–2602 (2002).

166. T. Murata *et al.*, *Chem. Mater.,* **22**, 3121–3132 (2010).

167. D. C. Palmer, S. E. Palmer, *CrystalMaker Software v.9.1*, (2016).

168. M. Hada *et al.*, *Sci. Rep.,* **5**, 13530 (2015).

169. R. Bertoni *et al.*, *Nat. Mater.,* **15**, 606–610 (2016).